The following text is a preprint of the book:

Nicolas Fries; Capillary transport processes in porous materials – experiment and model; Cuvillier Verlag Göttingen; 2010; ISBN 978-3-86955-507-2

The book is available directly at www.cuvillier.de or online shops such as www.amazon.de

# Capillary transport processes in porous materials - experiment and model

Vom Fachbereich Produktionstechnik

der

UNIVERSITÄT BREMEN

zur Erlangung des Grades

Doktor-Ingenieur

genehmigte

Dissertation

von

Dipl.-Ing. Nicolas Fries

Gutachter: PD Dr. M.E. Dreyer

Prof. Dr. D. Quéré

Tag der mündlichen Prüfung: 01.09.2010

# Zusammenfassung

Das Ziel der hier vorgestellten Arbeit ist die Untersuchung von kapillardominierten Transportprozessen in porösen Materialien und kleinen, zylindrischen Rohren. Von Relevanz ist dies insbesondere für die raumfahrtbezogene Anwendung von porösen Metallgeweben (häufig Dutch Twilled Weaves) in sogenannten Propellant Management Devices (PMDs) für Treibstofftanks. So gilt es, bei der Konstruktion von Raketentanks für flüssige Treibstoffe sicherzustellen, dass in einer Mikrogravitationsumgebung kein Gas in die Treibstoffleitungen gelangt. Diese Aufgabe übernehmen die PMDs häufig dadurch, dass sie den Blasendurchbruchsdruck (bubble point) von porösen Strukturen nutzen.

Der erste Teil der Arbeit beschäftigt sich mit einer grundlegenden Diskussion der theoretischen Modellierung kapillarer Strömungen. Zunächst wird eine Einführung in relevante Grundgleichungen, wie beispielsweise die integrale Bilanz des Impulses, gegeben. Die im nächsten Schritt vereinfachte Impulsbilanz stellt dann die Basis für die weiteren mathematischen Betrachtungen dar, die im Folgenden um sogenannte Pore Structure Parameters ergänzt werden, um die kapillaren Strömungen in porösen Materialien umfassend beschreiben zu können. Durch die Verwendung der Parameter statischer Radius (Beschreibung des Kapillardrucks), Permeabilität (Beschreibung des viskosen Druckverlustes in der porösen Struktur) sowie Porosität (Beschreibung des Verhältnisses von Porenvolumen zu Gesamtvolumen) lässt sich eine Impulsbilanz für poröse Materialien aufstellen. Es zeigt sich, dass die Gleichungen für poröse Materialien bzw. für zylindrische Rohre ähnlich sind und somit eine Analogie zwischen kapillaren Transportprozessen in zylindrischen Rohren und porösen Strukturen existiert. Folglich lassen sich analytische Lösungen, die ursprünglich nur für Strömungen in Rohren entwickelt wurden, auch für die Beschreibung von Transportprozessen in porösen Strukturen verwenden.

Unter Anwendung des Buckingham Pi Theorems werden in einer detaillierten Dimensionsanalyse die verschiedenen Skalierungsansätze vorgestellt und diskutiert. Anhand eines mathematischen Vergleiches der verschiedenen analytischen Lösungen für einen trägheits- bzw. viskos dominierten Transport kann eruiert werden, welche Kräfte zu welchem Zeitpunkt des Trans-

portprozesses relevant sind. Die Erkenntnis, welche Terme berücksichtigt werden müssen, ist eine wichtige Voraussetzung für eine präzise Beschreibung des Transportprozesses. Ein Vergleich des Modells mit experimentellen Daten aus der fachspezifischen Literatur konnte hierbei eine gute Übereinstimmung nachweisen.

Bei Transportprozessen, die unter Einfluss von Gravitation stattfinden, ist es darüber hinaus jedoch notwendig, eben diesen Parameter in die Modellierung mit einzubeziehen. Häufig wurde dies aufgrund fehlender analytischer Lösungen vernachlässigt und stattdessen auf bestehende, vereinfachte Lösungen, wie beispielsweise die Lucas-Washburn Gleichung, zurückgegriffen. Durch die mathematische Umformung einer impliziten t(h) Lösung von Washburn in eine explizite h(t) Lösung soll für diesen Bereich nun eine neue, präzisere Lösung vorgestellt werden. Ein Vergleich beider Gleichungen konnte hier zeigen, für welche Fälle die klassische Lucas-Washburn Lösung zulässig ist und wo sie an ihre Grenzen stößt: So wird deutlich, dass bei der Anwendung der herkömmlichen Gleichung bei einer Steighöhe von unter 10 % der Gleichgewichtshöhe (der maximalen Steighöhe) ein Fehler von höchstens 3.5 % auftreten kann. Wird diese Höhe jedoch überschritten, nimmt der Fehler erheblich zu und es empfiehlt sich, auf die neue h(t) Lösung zurückzugreifen.

Die mit einem kommerziellen CFD tool erstellten makroskopischen Simulationen zeigen im Vergleich eine sehr gute Übereinstimmung mit analytischen Lösungen. Somit kann die Anwendbarkeit dieser Modelle auf die untersuchten Prozesse bestätigt werden. Anschließend wird auf zwei Sonderfälle von kapillaren Strömungen eingegangen; die Gegenüberstellung von mathematischem Modell und Experimentdaten steht hierbei im Mittelpunkt der Analyse. Untersucht wurde zunächst der Einfluss von Verdampfung auf den kapillaren Anstieg in porösen Strukturen. Anhand von Experimenten konnte gezeigt werden, dass Verdampfung insbesondere bei sehr dünnen porösen Materialien, wie beispielsweise Metallgeweben, eine starke Verlangsamung des Prozesses sowie eine Reduktion der maximal erreichbaren Höhe bewirkt. Dieses kann zusätzlich durch ein mathematisches Modell gestützt werden, welches mit den Experimentdaten eine ausreichende Übereinstimmung aufweist (20 % Abweichung). Der zweite Sonderfall bezieht sich auf den radialen Flüssigkeitstransport, wie er beispielsweise bei der Ausbreitung eines Tropfens in einem Gewebe auftritt - im Hinblick auf die Untersuchung soll hier jedoch von der Speisung durch ein unendlich großes Flüssigkeitsreservoir ausgegangen werden. Die mathematische Beschreibung erlaubt es, analytische Lösungen für die aufgestellte Differentialgleichung zu entwickeln, die für den Fall des radialen Transports von Flüssigkeit nach außen eine gute Übereinstimmung mit den erzielten Experimentdaten zeigen.

Die Arbeit schließt mit einem Ausblick auf anwendungsbezogene Problemstellungen, die eine weitergehende Beschäftigung mit dieser Thematik erlauben. In vielen Raketenoberstufen wird Wasserstoff und Sauerstoff in tiefkalter (kryogener), flüssiger Form als Treibstoff eingesetzt. Bei der Entwicklung von PMDs für eben diese Anwendungen müssen auch kapillare Transportprozesse in porösen Materialien berücksichtigt werden. Während im Rahmen der hier vorgestellten Untersuchung nur auf isotherme Strömungen eingegangen werden konnte und thermale Aspekte vernachlässigt wurden, besteht ein deutlicher Bedarf an weiteren mathematischen oder numerischen Modellen sowie experimentellen Daten für nicht-isotherme Strömungen. In Bezug auf die Raumfahrttechnik und die Konstruktion von Tanks und PMDs gilt dies insbesondere für den kryogenen Bereich. Ein weiterer Schritt in diese Richtung wird derzeit am ZARM Institut (Universität Bremen) in Anbindung an das Graduiertenkolleg PoreNet unternommen.

# Preface

This work evolved from my employment as a research associate in the Multiphase Flow Group at the Center of Applied Space Technology and Microgravity (ZARM) at the University of Bremen. First of all I would like to gratefully acknowledge PD Dr.-Ing. Michael Dreyer, who not only provided very helpful guidance, supervision and scientific direction, but also allocated the necessary funds for many experiments. Without his appreciated and valued support this work could not exist.

Especially I would like to thank Prof. Dr. D. Quéré for agreeing to supervise my work and for his participation in the examination process. His thoughtful comments and advice during the review of my work was very helpful. I also like to acknowledge Prof. Dr. G. Grathwohl, Prof. Dr. S. Will, Dr. A. Grah and M. Meistering for taking their valuable time to be part of my examination committee. Many thanks also to Prof. Dr. H. J. Rath, director and founder of the ZARM institute, and especially to Prof. Dr. F. Peters, who introduced me to the field of fluid mechanics during my studies at the Ruhr-Universität Bochum. This work was funded by the German Research Foundation (DFG) through the Research Training Group 1375 "PoreNet", and I would like to express my gratitude towards all members of PoreNet for the numerous useful discussions and the advice given. In particular I would like to thank Prof. Dr. G. Grathwohl, spokesman of PoreNet, and Dr. M. Wilhelm for organizing the regular meetings, lectures and events.

Special thanks are due to my colleagues who helped to design and build the experimental hardware. Without the valued support of Frank Ciecior, Holger Faust, Ronald Mairose and Peter Prengel the experiments could have never been conducted. I owe gratitude to Stephanie Dackow, who did a great job organizing literature and helping with the completion of administrative duties. Many thanks also to my colleagues Dr. Karine Odic, Dr. Michael Conrath, Jörg Klatte, Tim Arndt, Dr. Aleksander Grah and Diana Gaulke who worked on projects with me, went to conferences and business trips with me, and spent some of their scarce time reviewing my papers. They also helped me in numerous discussions with their comments and

advice. I would also like to especially acknowledge the support of my (former) students Aykut Kaya, Blazenko Coskovic, Ming Zhang, Malte Meistering and René Sionkiewicz who helped with building the hardware and who performed many of the experiments and data analyses.
I also thank the companies Spoerl KG, ROBU Glasfilter Geräte GmbH and Krüss GmbH for the interesting discussions on porous media and surface tension effects.
Last but not least it is my pleasure to especially mention my wife Lucie-Patrizia Arndt and her understanding and patience with me. Without her great moral support it would have been a much harder time. I also owe gratitude to my family, in particular to my parents Dr. Ursula Fries and Dr. Helmut Fries who funded my undergraduate studies. Many thanks also to my friend Petar Valov with whom I always had many helpful and uplifting discussions.
For my dear grandfather Kurt Niggemann (1923-2010).

Bremen, July 2010

# Contents

# List of Symbols

## Latin symbols

| | | |
|---|---|---|
| $a$ | [$s^2/m^2$] | parameter Eq. (3.4) |
| $A_b$ | [$m^2$] | cross sectional area of a specimen ($w\,T$) |
| $b$ | [$s/m^2$] | parameter Eq. (3.5) |
| $b_{,h}$ | [$s/m^2$] | $b$ found in horizontal strip experiment |
| $b_{,v}$ | [$s/m^2$] | $b$ found in vertical strip experiment |
| $\overline{b}$ | [$s/m^2$] | mean value of $b$ |
| $\Delta b$ | [$s/m^2$] | error of $b$ |
| $c$ | [1/m] | parameter Eq. (3.6) |
| $c_v$ | [J/(kg K)] | specific heat (constant volume) |
| $c_p$ | [J/(kg K)] | specific heat (constant pressure) |
| $C$ | [-] | mathematical integration constant |
| $d$ | [-] | differential symbol |
| $d$ | [m] | distance between parallel plates |
| $D$ | [m] | inner tube diameter |
| $e$ | [-] | Euler's constant (2.71828...) |
| $E$ | [J] | energy |
| $F$ | [N] | force |
| $F_{fr}$ | [N] | viscous friction force |
| $F_{gr}$ | [N] | gravity force |
| $F_{pl}$ | [N] | force at the lower boundary |
| $F_{pu}$ | [N] | force at the upper boundary |
| $g$ | [$m/s^2$] | gravity |
| $h$ | [m] | wicking height |
| $\Delta h$ | [m] | height difference between screen and reservoir see Fig. 8.1 |

| | | |
|---|---|---|
| $h_0$ | [m] | height due to wetting see Fig. 7.4 |
| $h_1$ | [m] | separation height see chapter 4.3 |
| $h_{2,S}$ | [m] | separation height see chapter 4.3 |
| $h_{2,Q}$ | [m] | separation height see chapter 4.3 |
| $h_3$ | [m] | separation height see chapter 4.3 |
| $h_c$ | [m] | meniscus height see Fig. 2.3 |
| $h_{eq}$ | [m] | equilibrium meniscus height |
| $h_l$ | [m] | immersion height see Fig. 7.4 |
| $h_m$ | [m] | meniscus height see Fig. 2.3 |
| $h_t$ | [m] | meniscus height see Fig. 2.3 |
| $h_w$ | [m] | maximum height of validity of the Lucas-Washburn equation |
| $h_{wi}$ | [m] | height due to wicking see Fig. 7.4 |
| $H$ | [m] | height of the screen |
| $K$ | [$m^2$] | permeability of a porous structure |
| $K_s$ | [-] | coefficient by Sparrow et al. see Eq. (2.41) |
| $L$ | [m] | characteristic length |
| $L_e$ | [m] | entrance length see Eq. (2.39) |
| $m$ | [kg] | mass |
| $\vec{n}$ | [m] | normal vector |
| $p$ | [Pa] | pressure |
| $p_0$ | [Pa] | pressure at inlet |
| $p_a$ | [Pa] | ambient pressure |
| $p_f$ | [Pa] | pressure at front |
| $p_{wick}$ | [Pa] | pressure loss in the wick |
| $P_b$ | [m] | perimeter of a specimen $[2\,(w+T)]$ |
| $Q$ | [J] | heat |
| $r$ | [m] | radial coordinate |
| $r_0$ | [m] | initial radius of the wetted spot (wick radius) |
| $r_f$ | [m] | front radius of the wetted spot |
| $R$ | [m] | inner tube radius |
| $R_1$ | [m] | first principal radius of curvature |
| $R_2$ | [m] | second principal radius of curvature |
| $R_s$ | [m] | mean static porous medium pore radius |

| | | |
|---|---|---|
| $s$ | [m] | distance between screen and camera |
| $s(t)$ | [s] | factor by Siegert et al. see Eq. (2.32) |
| $S_a$ | [m$^2$] | control surface a |
| $t$ | [s] | time |
| $t_1$ | [t] | separation time see chapter 4.3 |
| $t_{2,S}$ | [t] | separation time see chapter 4.3 |
| $t_{2,Q}$ | [t] | separation time see chapter 4.3 |
| $t_3$ | [t] | separation time see chapter 4.3 |
| $t_r$ | [s] | reorientation time see Eq. (2.33) |
| $t_s$ | [s] | time to reach static state |
| $t_w$ | [m] | maximum time of validity of the Lucas-Washburn equation |
| $T$ | [m] | thickness of a specimen |
| $v$ | [m/s] | velocity (of the front line) |
| $v_0$ | [m/s] | velocity at inlet (radial wicking) |
| $v_f$ | [m/s] | velocity at front (radial wicking) |
| $v_i$ | [m/s] | interstitial velocity |
| $v_r$ | [m/s] | velocity in radial direction |
| $v_{rel}$ | [m/s] | relative velocity |
| $v_s$ | [m/s] | superficial velocity |
| $v_Q$ | [m/s] | constant rise velocity see Eq. (2.37) |
| $v_z$ | [m/s] | velocity in height direction |
| $v_\varphi$ | [m/s] | velocity in angular direction |
| $V$ | [m$^3$] | volume |
| $V_a$ | [m$^3$] | control volume a |
| $V_b$ | [m$^3$] | control volume b |
| $\dot{V}$ | [m$^3$/s] | liquid flow rate |
| $w$ | [m] | specimen width see Fig. 8.9 |
| $W$ | [J] | work |
| $W(x)$ | [-] | Lambert W function Eq. (5.17) |
| $x$ | [m] | position |
| $x_0$ | [m] | initial meniscus position in the strip experiments |
| $x_f$ | [m] | position of the front |
| $z$ | [m] | height coordinate |

# Greek symbols

| | | |
|---|---|---|
| $\beta_F$ | [1/m] | Forchheimer coefficient Eq. (2.4) |
| $\gamma$ | [1/s] | parameter Eq. (7.22) |
| $\delta$ | [-] | parameter for initial height Eq. (5.54) |
| $\epsilon$ | [-] | parameter for allowed deviation Eq. (5.28) |
| $\phi$ | [-] | porosity of the structure |
| $\varphi$ | [°] | angle coordinate |
| $\Phi$ | [-] | dimensionless related maximum height Eq. (7.33) |
| $\mu$ | [kg/(ms)] | dynamic viscosity |
| $\nu$ | [$m^2$/s] | kinematic viscosity |
| $\pi$ | [-] | circle constant (3.14159...) |
| $\pi_1$ | [-] | first dimensionless $\pi$ parameter by Buckingham method |
| $\pi_2$ | [-] | second dimensionless $\pi$ parameter by Buckingham method |
| $\pi_3$ | [-] | third dimensionless $\pi$ parameter by Buckingham method |
| $\rho$ | [kg/$m^3$] | density |
| $\rho_h$ | [-] | regression coefficient (horizontal strip exp.) |
| $\rho_v$ | [-] | regression coefficient (vertical strip exp.) |
| $\sigma$ | [N/m] | surface tension |
| $\theta$ | [°] | contact angle |
| $\theta_d$ | [°] | dynamic contact angle |
| $\theta_s$ | [°] | static contact angle |
| $\Omega$ | [-] | dimensionless basic parameter, see Eq. (3.10) |

# Dimensionless numbers

| | | |
|---|---|---|
| Bo | [-] | Bond number, see Table 3.3 |
| Ca | [-] | Capillary number, see Table 3.3 |
| Fr | [-] | Froude number, see Table 3.3 |
| Ga | [-] | Galileo number, see Table 3.3 |
| Oh | [-] | Ohnesorge number, see Table 3.3 |

| | | |
|---|---|---|
| Re | [-] | Reynolds number, see Table 3.3 |
| $\mathrm{Re}_d$ | [-] | Reynolds number based on tube diameter |

## Indices to indicate dimensionless scaling

| | |
|---|---|
| † | Index for dimensionless variable: viscous effects and gravity as scaling forces, see Eq. (3.8) |
| ‡ | Index for dimensionless variable: inertia and gravity as scaling forces, see Eq. (3.15) |
| $*$ | Index for dimensionless variable: inertia and viscous effects as scaling forces, see Eq. (3.21) |
| $\star$ | Index for dimensionless variable for radial wicking, see Eqs. (8.4 and 8.5) |

# Chapter 1

# Introduction

Liquid flows driven by capillary forces represent an important field of research as many applications in science, industry and daily life rely on this process. For example in technical applications such as heat pipes or spacecraft Propellant Management Devices (PMDs) capillarity is of high importance. This also applies for average consumer products like marker pens, candle wicks as well as sponges. In nature capillary transport can be found in plants, where together with the osmotic pressure it facilitates the transport of water from the roots to the tips, or in the field of hydrology where the movement of groundwater is influenced by capillary transport as well. Typically, this transport occurs in complex shaped structures. However, many flow or layout calculations adopt models for cylindrical tubes or simplified porous materials to match the flow in arbitrary shaped capillaries. Despite their reduction in complexity, macroscopic approaches to capillary transport have been very successful in describing many of the presented problems.

A large amount of literature is devoted to capillary transport but there is still a need for fundamental research to fully understand the processes. Due to the described relevance for technical applications experimental data, models, and numerical simulations are of importance to engineers designing heat pipe systems or PMDs for instance. Besides these applications, capillary transport processes are also a very interesting subject for fundamental research in a sense of pure science. By analytical means theoretical modeling or dimensionless scaling can be conducted - e.g. based on the momentum balance of a fluid inside a porous structure - and then compared to experimental data for validation purposes. These processes also provide good test cases for validation of CFD tools to enable a deeper insight into the fluid mechanics behind capillary dominated problems.

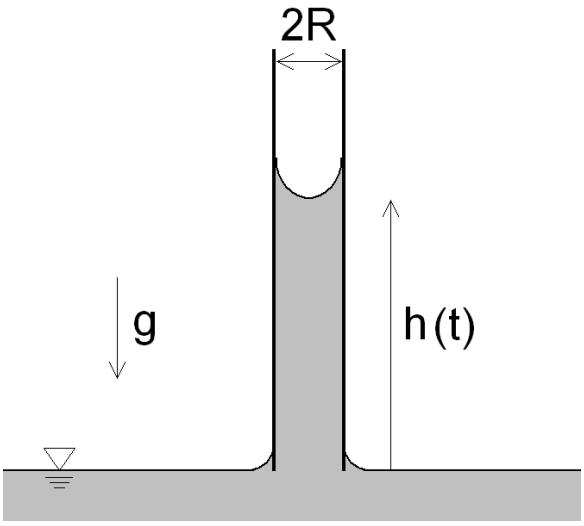


Figure 1.1: Liquid rise in a capillary tube of inner radius $R$. Gravity vector $g$ is parallel to the tube. The height of the liquid column is a function of time and denoted $h(t)$.

## 1.1 Applications of capillary transport

As previously mentioned, there are numerous applications of capillary transport phenomena in engineering, daily life and science. Two technical applications shall be introduced briefly in the following section. The first one "Propellant Management Devices" describes the main motivation of this work, while the second one "Heat Pipes" concerns a system of major importance to thermal management of spacecraft .

### 1.1.1 Propellant Management Devices

In many spacecrafts and rockets liquid propellants are used as they typically provide a much higher specific impulse $I_{sp}$ than solid propellants. The specific impulse can be regarded as change in momentum per mass of the propellant that is used. Consequently, a propulsion system with a higher $I_{sp}$ is more efficient and will need less propellant to obtain the same $\Delta v$ (change in velocity). For many cases the increased complexity and costs of liquid propulsion systems are more than balanced by their higher specific impulse.
However, the main problem in liquid spacecraft propellant tanks in orbit is the lack of gravity to define "up" and "down". When operating within microgravity, it can become difficult to separate the liquid propellant from the pressurant gas in the tanks. Despite this, a constant and gas free delivery of propellant to the engines has to be ensured during all acceleration conditions of the mission. To handle this problem, Propellant Management Devices (PMDs)

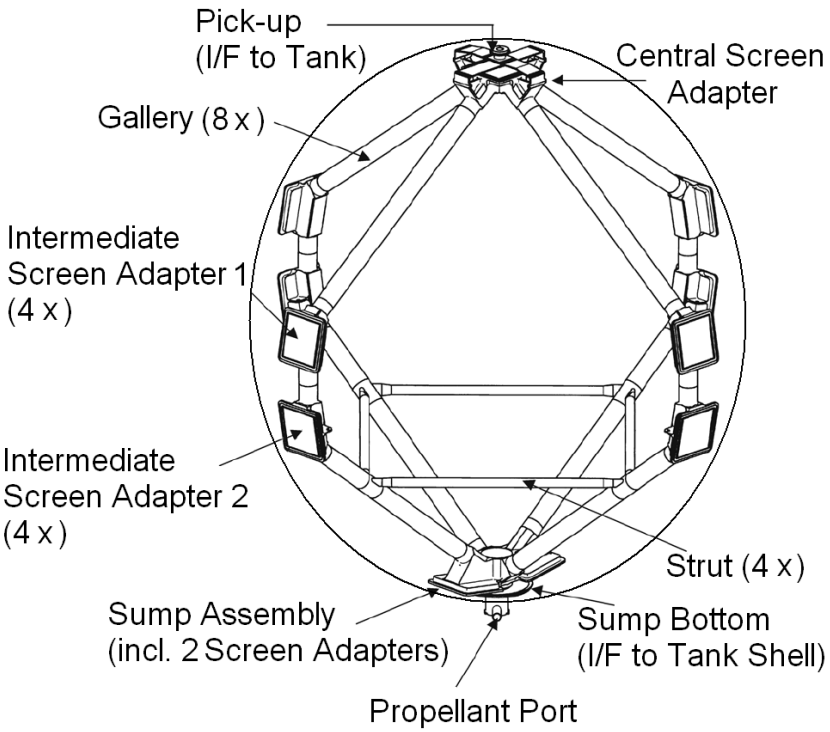


Figure 1.2: Total communication type Propellant Management Device (PMD) of the Automated Transfer Vehicle [8] including galleries with screen windows (slightly modified).

are utilized. These often feature a fine porous structure - like a metallic weave - which allows liquid to permeate but blocks out gas below a critical differential pressure. This phenomenon is known as the bubble point effect. Propellant Management Devices are designed to i) ensure a constant connection between propellant and tank outlet (communication type) or ii) confine the propellant at a designated location (control type) [1, 27, 82]. Fig. 1.2 shows a total communication type PMD including galleries with porous screen windows. These screens are made of metal weave and form passive surface tension devices. As mentioned they allow propellant to penetrate but prevent gas from entering below a critical bubble point pressure. This mechanism requires the weave to be always saturated with propellant. If a screen is partially dry, wicking can be regarded as a self healing mechanism to restore saturation. Here, the wicking performance strongly depends on the degree of evaporation from the porous screen. Especially for cases where the propellants are cryogenic liquids such as hydrogen and oxygen (as displayed in Fig. 1.3), the PMD may fall dry during coast phases, and require appropriate refilling and rewetting of the structure during subsequent chill down. This is the motivation for chapter 7 “Linear capillary rise and the effect of evaporation”.

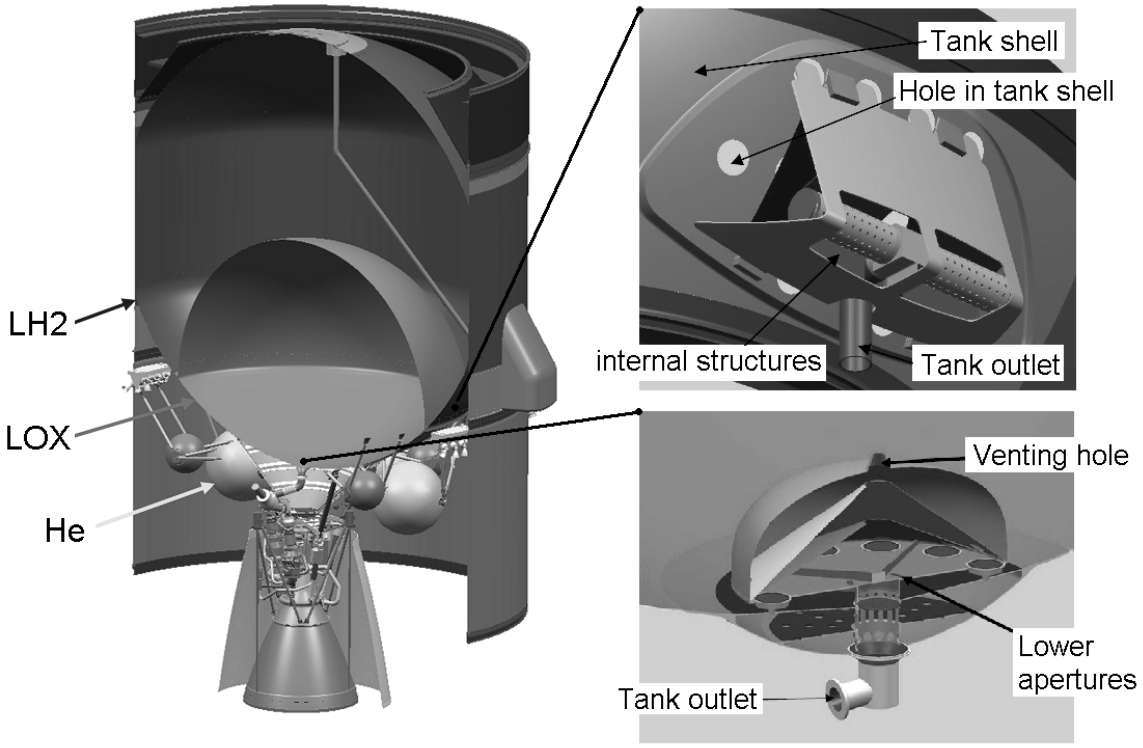


Figure 1.3: Draft of the proposed Propellant Management Device for the new, restartable upper stage ESC-B for the European launcher Ariane 5 [7] (slightly modified).

Transport processes in porous materials are also of great interest to determine material properties which affect relevant parameters including cross flow pressure and bubble point pressure. A better understanding of the occurring processes will enable engineers to identify better structures for usage in PMDs. These structures should provide several characteristics, e.g. have a high bubble point, however feature a minimal resistance against fluid flow (= a high permeability).

### 1.1.2 Heat Pipes

Heat pipes are passive devices designed to effectively facilitate the transport of heat from a hot heat source to a colder heat sink [103]. To transport comparably large amounts of heat they only require a fairly low temperature difference between the hot and cold interfaces. As shown in Fig. 1.4, a heat pipe evaporates liquid at its hot end. The resulting vapor is transported through the center cavity and condensates at the cold end, which provides heat transport due to the latent heat of phase change. The liquid however must return back to the hot end to

close the loop. For this process, porous materials or structured surfaces are used which - due to capillary forces - transport the liquid back to the hot end to restore saturation (see Fig. 1.5). The advantages of heat pipes in comparison to conventional heat transport systems are not only the passivity and robustness. Due to their low thermal resistance they provide very high heat fluxes [$W/m^2$] based on their cross section. For a typical device length this results in a smaller system diameter and mass when compared to a block of copper for example. Working temperatures of heat pipes range from a few (5) Kelvin up to several thousand (2200) Kelvin. The choice of the working fluid strongly depends on the operating temperature range [103]. The following list provides a brief, incomplete overview:

- Cryogenic temperatures down to a few K: liquified gases like e.g. Helium (He), Hydrogen ($H_2$), Nitrogen ($N_2$).
- Cool temperatures below 250 K: Methane ($CH_4$), Ethane ($C_2H_6$).
- Moderate temperatures up to 500 K: Freon, Ammonia ($NH_3$), Water ($H_2O$).
- High temperatures: molten metals like Mercury (Hg), Potassium (K), Sodium (Na), Lithium (Li), Silver (Ag).

Due to their application in low temperature engineering, spacecraft thermal control, and electronic device cooling systems (see Fig. 1.5) - just to mention a few - heat pipes can probably be considered to be the most important devices featuring porous structures with capillary transport.

## 1.2 Embedment of this work in the frame of PoreNet

PoreNet is a Research Training Group (Graduiertenkolleg) funded by the German Research Foundation DFG. Several institutes from different disciplines participate in a collaborative and interdisciplinary effort to enhance the understanding of *Nonmetallic Porous Structures for Physical-Chemical Functions*. The aim of the work conducted in the Multiphase Flow Group at the ZARM is to investigate capillary dominated flows in porous materials to improve the comprehension and knowledge of the occurring processes and effects. This is conducted with a special focus on topics of relevance for the application of capillary flows in Propellant Management Devices as introduced earlier in this chapter. The underlying rationale is that an enhanced understanding of these topics will allow to design enhanced materials for these applications -

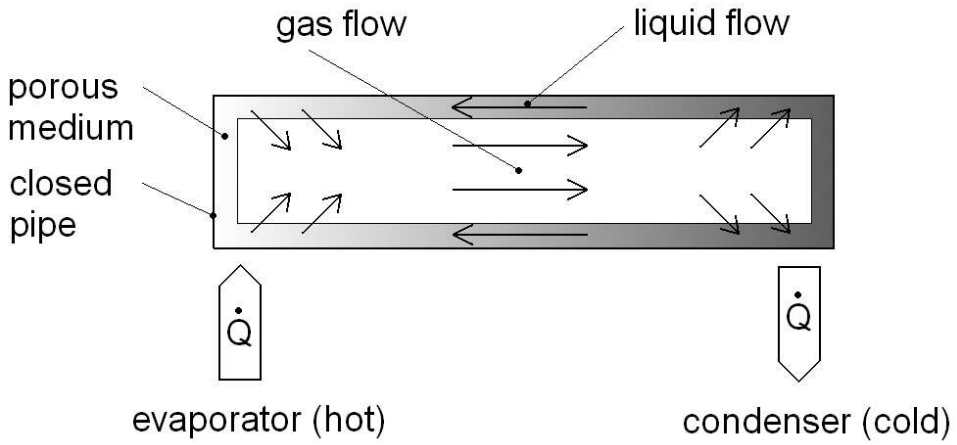


Figure 1.4: Schematic drawing of a heat pipe. Liquid is evaporated at its hot end (left) and condensed at the cold end (right). Capillary transport of liquid from cold to hot end.

which can be realized only in a design, production and testing loop in close cooperation with the other participating institutes. This present work is part of the first generation of doctorates in PoreNet and seeks to build the theoretical and experimental foundation concerning capillary flows in porous media for the works to follow. Relevant pore structure parameters and analogies to classic cylindrical capillaries are discussed in terms of analytical approaches and experiments as will be explicated in the next section.

## 1.3 Questions and aims of this work

The first part of this study is dedicated to a fundamental discussion of capillary flows. The aim is to enhance the understanding as well as the classification of capillary flows and the dominant forces by an analytical approach based on the governing equations. In chapter two of this work, the current "state of the art" of capillary driven flow is discussed and the main theoretical models, pore structure parameters, analogies and governing equations are introduced. The third chapter deals with a dimensionless scaling of the equation of motion. By this investigation the fundamental physics can be examined. Furthermore, the process of capillary dominated flow can be understood with a deeper insight than the dimensional consideration would allow. It also allows the classification of the rise process into different time stages under the impact of different corresponding forces. Chapter four investigates the transition from inertia dominated flow stage to the viscous stage during capillary rise. This helps to identify a priori the dominant forces that govern the flow. In the fifth chapter, analytical solutions including the gravity term,

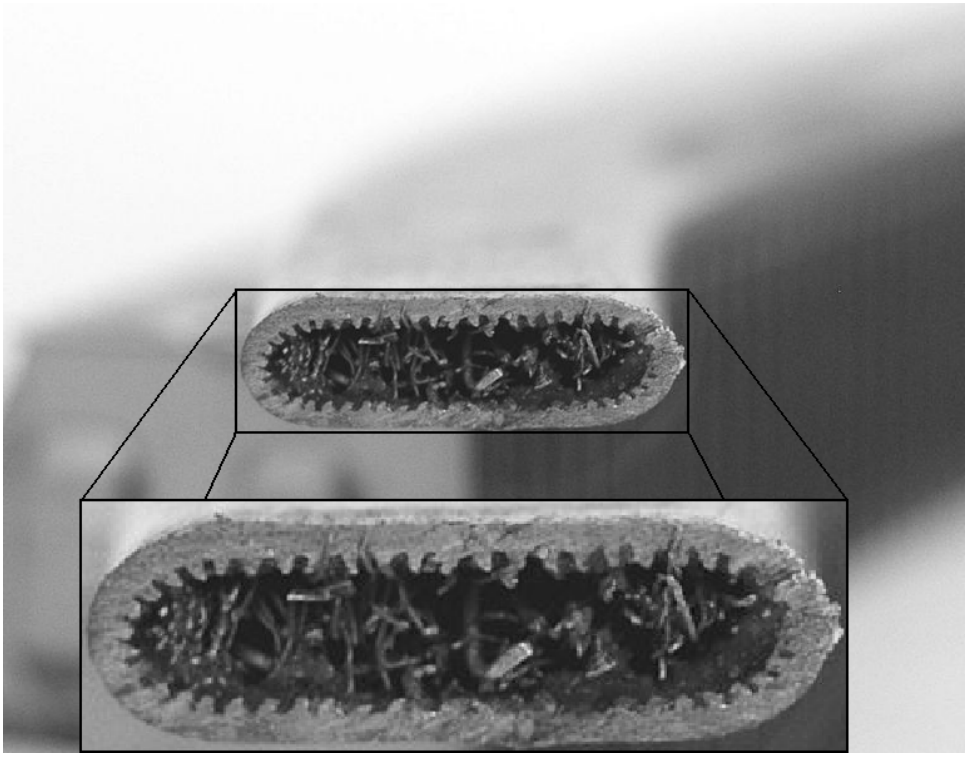

Figure 1.5: Cross section of a heat pipe used for cooling computer processors. Capillary transport is obtained by application of a grooved surface and copper gauze [108].

based on the implicit Washburn equation, are introduced. The discussion of the results allows to understand and predict capillary flows for an extended range of time. Some numerical simulations (CFD) and a macroscopic model of capillary rise is presented in the sixth chapter. The second part of this work investigates special cases of relevance to applications in spaceflight. The aim is to conduct fundamental research and to develop verified mathematical models that enable engineers to design enhanced PMDs. In chapter seven the linear capillary rise in thin, porous, metallic structures and glass filter frits is investigated. Also the effect of evaporation on capillary rise is determined. The interest arises particularly due to the actual development of a cryogenic, restartable upper stage (ESC-B) for the European launcher Ariane 5 (see Fig. 1.3). The eighth chapter discusses radial capillary transport in porous structures. This is in contrast to the previous chapters which all investigate linear transport. However, similar to the previous chapters a mathematical model is derived to describe the flow. An experimental setup for outward wicking is used to validate the analytical model. Thus, one is able to determine the validity of the derived solution and to discuss the assumptions made during the derivation of the model.

# Part I

# Fundamental discussion of capillary flow

# Chapter 2

# Theory of capillary dominated flows - State of the art

## 2.1 Literature review

### 2.1.1 Capillary rise

Due to the numerous applications of capillary transport - as described in the previous chapter - there exist many publications dealing with this problem, the mathematical description as well as the physical explanation. Since several hundred years, researchers (e.g. in 1712 Taylor [100], 1712 Hauksbee [42], 1717 Jurin [49], 1805 Young [111], 1806 Laplace [25] or 1908 Ostwald [76]) investigate capillary rise and try to develop equations for the maximum reachable height and relations between height and elapsed time. In 1918 Lucas [61] and 1921 Washburn [104] provide the first analytical explanation for the observed capillary rise velocity. They consider a flow regime where the influences of inertia and gravity can be neglected. By omitting some terms of the momentum balance, they derive an analytical solution providing the meniscus height as a function of time. Comparison of the predicted values with experimental results shows good agreement, however it also points out the limitations of the model. Thus, in following publications, many researchers tried to add missing or neglected terms to the momentum balance to extend the validity of the derived solutions, or otherwise to determine the impact of the neglected terms (e.g. in 1922 Rideal [81], in 1923 Bosanquet [11], and in recent years Siebold et al. [89], Hamraoui and Nylander [41], and Lavi et al. [55]). Ichikawa and Satoda [47] describe the interface dynamics of capillary flow and derive dimensionless variables.

#### 2.1.1.1 New experimental techniques and numerical approaches

Due to the advances in the power of computers in the 1960s it has become possible to numerically solve differential equations (e.g. by a Runge-Kutta algorithm, 1971 Szekely et al. [99]) or to conduct simulations (CFD) of capillary dominated processes. The improving measurement technology available for the experiments has triggered several new approaches to investigate the capillary rise in the very first moments after the contact using high speed cameras (Quéré [78]). The behavior in microgravity environments is examined by Dreyer et al. [31] and Stange et al. [96]. Details of the flow field at the meniscus are experimentally investigated using Micro Particle Image Velocimetry ($\mu$PIV) by Nasarek et al. [73]. Influence of a phase change (condensation, evaporation) at the meniscus in a capillary tube is examined by Ramon and Oron [80].

#### 2.1.1.2 Flow regimes

Based on the momentum equation, Stange [95, 96] claims that the capillary rise process can be divided into four successive stages with i) an initial $h \sim t^2$ domain corresponding to the local acceleration of the liquid, ii) a $h \sim t$ domain related to the convective losses, iii) a $h \sim \sqrt{t}$ domain related to viscous dissipation and finally iv) a $h \sim 1 - e^{-(1+t)}$ domain due to the gravity deceleration. These domains show transitions at specific, characteristic times which are also addressed by Fries and Dreyer [36]. The inertia dominated flow regime in capillary tubes is examined previously in depth by Quéré [78] and Quéré et al. [79]. They notice that oscillations occur if the fluid viscosity is low enough. In contrast, for some cases - mostly very small capillaries and setups with porous media - the inertial forces can be neglected. In the non-inertial capillary flow regime many authors, for example Dodge [27], Symons [98] and Washburn [104], apply a simple model in which the capillary pressure is balanced only by viscous friction and hydrostatic pressure. Zhmud et al. [112] give a good overview to solutions for different time regimes and derive short and long time asymptotic solutions. Siebold et al. [89] carry out capillary rise experiments in glass capillaries and packed powder to investigate the effect of the dynamic contact angle. Hamraoui and Nylander [41] provide an analytical approach for setups with a highly dynamic contact angle. Chan et al. [18] provide factors affecting the significance of gravity on infiltration of a liquid into a porous medium. Xue et al. [110] report on dynamic capillary rise with hydrostatic effects. In a recent paper Chebbi [19] investigates the dynamics of liquid penetration and compares numerical results with asymptotic solutions.

### 2.1.2 Porous media

When a fluid enters a porous medium due to capillary effects, a complex flow field develops within its pores. This wicking depends on geometrical and physical properties of the structure (see Fig. 2.1) and the physical properties of the liquid. Many authors have considered this capillary penetration of liquids into porous media: Van Oss et al. [102], for example, determine contact angles and pore sizes of porous media by column and thin layer wicking. They demonstrate that low-surface-energy liquids pre-wet the surface over which they subsequently spread. Siebold et al. [89] focus on total wetting liquids in powders featuring a zero degree contact angle at equilibrium. They show that during the rising process the contact angle is higher than expected and propose a new method to re-calculate the constant terms in the Lucas-Washburn equation. A review article written by Bachmann et al. [3] describes the available methods to determine the wetting properties of porous media. Chibowski et al. [20] review existing literature on formulation and determination of free surface energy. Furthermore, they depict contact angle problems that also involve spreading liquids. Delker et al. [26] and Lago and Araujo [54] write about the rise of liquids in columns of glass beads and observe Lucas-Washburn behavior for small time scales, however deviations for later times. Lockington and Parlange [59] find an equation for the capillary rise in porous media. Marmur and Cohen [65], [67] characterize porous media by analyzing the kinetics of capillary penetration. The extraction of pore structure parameters from capillary rise observations is also described by Fries et al. [39]. When reviewing actual literature, many recent publications on the topic of porous media can be found. This depicts the importance of the still unresolved questions. For instance, Lavi et al. [55] aim to characterize porous media, Masoodi et al. [70] focus on liquid absorption in polymer wicks, while Siddique et al. [88] investigate capillary rise in deformable porous media.

#### 2.1.2.1 Bundle of capillary tubes approach

Many models describing porous media are based on the assumption that the pore spaces correspond to a “bundle of capillary tubes”. In particular, this includes the previously mentioned works of Lucas [61] and Washburn [104] who study dynamic invasion of fluid into a cylindrical capillary or a porous medium. Levine et al. [57, 58] examine the momentum balance and investigate the departure from Poiseuille flow in the vicinity of an advancing meniscus in a vertical cylindrical capillary. They investigate capillary rise in tubes as well as in parallel plate channels. Marmur [65] examines the thermodynamic and kinetic effects on capillary penetration in systems of limited size. The capillary tube analogy is also the background for an approach that

aims to improve the consistency with real porous media. Here, the capillary tube is assumed to be non-uniform - for example sinusoidally constricted (varying in diameter) - which is proposed by Hemmat and Borhan [44], Staples and Shaffer [97] and Patro et al. [77].

#### 2.1.2.2 Darcy law approach

An alternative to using the capillary tube analogy is to apply the Darcy law to determine the viscous friction losses. This approach is, for example, used by Symons [98] and Marmur [66]. Further details on the Darcy law are provided in sections 2.2 and 2.5. Symons [98] conducts a study to determine the magnitude of wicking rates in various metallic screens, including the one also investigated in chapter 7 of this work: Dutch Twilled Weave (DTW) $200 \times 1400$. Symons develops an analytical model for the wicking process which expresses the wicking velocity as a function of liquid properties and geometrical parameters. His experimental results confirm the validity of this model. However, due to the complexity of the pore geometry within the screen, it is necessary to merge several screen geometry parameters into a single constant. Furthermore, he investigates the effect of evaporation and local heat sources as well.

#### 2.1.2.3 Green and Ampt approach and saturation issues

As recently pointed out by Barry et al. [4], the Green and Ampt [40] model represents a further alternative to the above models. The Green and Ampt model, which is often used by soil science researchers, describes the capillary rise or infiltration of water into soils. To describe the viscous losses they consider - analogous to the Darcy law - the permeability, while the capillary pressure is described using an empirical, integral constant determined by experiments. Barry et al. [4] also point out that the models (capillary tube analogy, Darcy approach and Green and Ampt model) all feature a sharp front between the dry and the wetted porous structure. Therefore, "the weave's saturation has only two states, completely saturated (all the pore space is filled with liquid) or completely unsaturated (all the pore space contains no liquid)" [4]. In all the models introduced before, the porosity $\phi$ (volume of pore space divided by total volume) is set to equal the saturation, which is only the case if the pore space is completely filled with liquid. The actual saturation depends on the local pressure and can be described using the "capillary pressure function", which often features a hysteresis for drainage and imbibition respectively. This topic is extensively discussed by Dullien [32] page 132 ff. Thus, the actual saturation must depend on the position within the porous structure (top or bottom when gravity forces apply) and can be lower than the maximum possible saturation, which is determined by the

porosity. Barry et al. [4] state: "The non-constant $\phi$ (author's note: in this context the liquid content) in the profile is largely due to the capillary diffusion of liquid in the weave. The capillary diffusion coefficient in a porous medium can be approximated by a power law, $\sim \phi^n$, with $4 \leq n \leq 8$ [15] (a.n. by Brooks and Corey) (if $n \to \infty$, $\phi^n$ approaches a delta function in which case $\phi$ becomes uniform and, for imbibition, the two-state saturation model ... ensues). The parameter $n$ is an empirical, medium-dependent constant. ... the liquid content $\phi$ is a function of position x given by Eq. (6) in [16] as $x/x_f = 1 - (\phi/\phi_0)^n$, where $x_f$ is the position of the wetting front and $\phi_0$ is the value of $\phi$ at saturation. Then the average liquid content is given by $(x_f\,\phi_0)^{-1} \int_0^{\phi_0} x\,d\phi = n/(n+1)$."

Though the physical considerations discussed above are correct their actual effect on capillary transport will vary from case to case. For some setups no influence will be measurable as demonstrated in the experimental chapters of this work. It can be assumed that at least two parameters, the uniformity of the pore sizes and the difference in local pressures, will affect how different the local degrees of saturation will be. For the theoretical models developed in this work a sharp jump in saturation is assumed at the interface position, while for further investigations microscopic simulations of the liquid within the pores may reveal further details on this issue.

## 2.2 Pore structure parameters and analogies

### 2.2.1 Porosity

The porosity $\phi$, relating the volume of pores to the total volume of the medium, is defined by

$$\phi = \frac{V_{Pores}}{V_{PorousMedia}}. \tag{2.1}$$

For most cases this definition is sufficient but for porous media with closed pores, e.g. like some foams, one has to distinguish between open porosity and closed porosity [83]. Open porosity refers to the pore volume which is accessible by a test liquid, while closed porosity will not influence wicking processes. However, it can be measured using the density of the porous structure. The porous media investigated in this work, as schematically displayed in Fig. 2.1, are all considered to have an open porosity only.

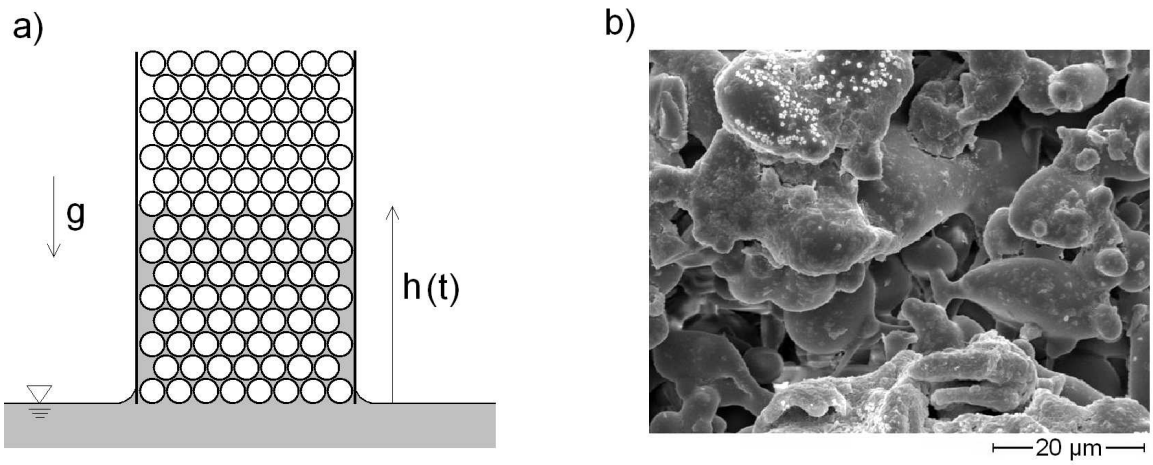


Figure 2.1: a) Vertical capillary rise setup using a generic porous medium. The liquid is wicking into the pore space formed between solid spheres. b) Scanning electron microscope image of the actual structure of a filter frit P5 (pore diameter 1 - 1.6 $\mu$m; courtesy F. Krause).

### 2.2.2 The Darcy law and extensions

The Darcy law was developed by H. Darcy in 1856 [24]. By investigating the flow of water through sand, it was found that the viscous pressure loss can be described by

$$\nabla p = -\frac{\mu}{K}\vec{v_s}, \tag{2.2}$$

where $v_s$ is the volume averaged velocity (superficial velocity). The factor $K$ is a factor depending on the pore geometry and pore size of the structure and is denoted permeability. The higher the permeability is, the easier the liquid can pass the porous obstacle and the lower the pressure drop will be. A comparison between the Hagen-Poiseuille law for the viscous loss in a cylindrical tube (as introduced later in Eq. (2.45)) and the Darcy law Eq. (2.2) shows that both equations are interchangeable with each other so that

$$R^2 = \frac{8K}{\phi}. \tag{2.3}$$

The porosity $\phi$ is included as the laws are defined for the interstitial (Hagen-Poiseuille) and the superficial velocity (Darcy) respectively. This analogy will be of interest again in the next section.

The Darcy law, predicting a linear relation between pressure drop and flow velocity, is only valid for small Reynolds numbers where convective terms can be neglected and viscous terms dominate. Due to the different pore geometries no specific critical pore Reynolds number can be provided for the validity of the Darcy law, as they vary between 0.1 and 75 ([32] page 245).

To account for the convective terms the Forchheimer equation can be applied

$$\frac{\Delta p}{L} = \frac{\mu}{K} v_s + \beta_F \rho \, v_s^2. \tag{2.4}$$

Here $\beta_F$, which has to be experimentally determined, is denoted "inertia parameter" [32] or Forchheimer coefficient. There also exist various empirically or theoretically derived equations like the Ergun equation, the Carman-Kozeny equation or the Brinkman equation [32] which give $K$ or $\beta_F$ as a function of $\phi$ and the average particle size if packed spheres are considered. Due to their limitation to certain porous materials they will not be explicated here.

### 2.2.3 Static radius

In anticipation of later results the capillary pressure of a cylindrical tube is given by Eq. (2.27)

$$\Delta p = \frac{-2\sigma cos(\theta)}{R}. \tag{2.5}$$

Considering porous materials the capillary pressure will be depending on the local pore size and saturation as described in section 2.1.2.3. Despite this physical background the average, macroscopic capillary pressure can be calculated using Eq. (2.5) with a slight modification

$$\Delta p = \frac{-2\sigma cos(\theta)}{R_s}. \tag{2.6}$$

Here, $R$ is replaced by the "static radius" $R_s$ to emphasize that the porous structure does not consist of capillary tubes with a specific radius $R$. One also assumes that the porous medium features a uniform pore size, which actually applies for few cases only. Despite these simplifications $R_s$ still is a useful parameter to determine the capillary pressure as will be shown in the experimental chapters of this work. The static radius $R_s$ can be calculated from the maximum obtainable "static" height $h_{eq}$, see Eq. (5.27)

$$h_{eq} = \frac{2\sigma \cos(\theta)}{R_s \rho g}, \tag{2.7}$$

which can be measured experimentally. Further alternatives which are not applied in this work are the radii measured by mercury intrusion porosimetry (as proposed by Washburn [105]), radii determined by optical and tomography methods, or radii obtained from bubble point considerations. It is important to notice that some of these methods will not provide a single defined radius, but a pore size distribution that features a maximum and a minimum pore size. This is of relevance if one seeks to microscopically simulate and understand the occurring processes.

With $R_s$ the last pore structure parameter of great relevance for this work is introduced. The three parameters $K$, $R_s$ and $\phi$ will be applied in all mathematical models which are derived and can be considered a central theme spanning the different chapters (e.g. see section 7.2 ff. for a discussion of the experimental approaches to determine the parameters).

As previously mentioned an analogy exists between linear capillary transport in a cylindrical tube and linear capillary transport in a porous structure. The advantage of the capillary tube is that - in contrast to porous media - all of its "pore structure parameters" are known with the tube radius $R$ and $\phi = 1$. Thus, as the physical processes occurring in both setups are the same, capillary tubes can be considered to be a good model medium for theoretical and experimental investigations of the flow in other porous structures. A further analogy can be found to capillary rise between parallel plates as presented in Eq. (8.29). There also exists an analogy between radial capillary transport in porous structures as studied in chapter 8 and the radial capillary between two plates as investigated by Marmur [64], see Fig. 8.18.

## 2.3 Radial capillary transport

Radial capillary transport, as discussed in chapter 8, is a basic mechanism that works under variable gravity conditions including weightlessness. Therefore, it is also of interest for space applications like Propellant Management Devices that ensure an undisturbed fuel supply. Within these devices, the capillary force is bound to porous, mostly woven structures like stainless steel weaves. If the liquid fuel comes in point contact with the porous structure for the first time, it imbibes it radially outward. If due to evaporation a part of the porous structure has fallen dry, it will be re-wetted by radially inward imbibition.

As previously discussed, linear capillary transport in a porous medium can be modeled by the capillary bundle theory. Consequently, when it comes to radial capillary transport in a porous medium, one might assume a radial capillary as done by Marmur [64]. He analytically studies the radially outward movement of a meniscus between two parallel plates with a liquid supply hole in the middle. This theory is experimentally supported by Danino and Marmur [23] who use filter paper for their experiments. The similarity between Marmur's hydrodynamic model and the porous model presented here will be explained later on in the discussion. Numerical calculations with Marmur's model are presented by Hsu and Ashgriz [46]. Smiles [91] investigates the connection between capillary suction time and filter properties of some papers. Capillary spot spreading in textile assemblies is examined by Kissa [53] and Kawase et al. [51].

In contrast to such flat radial geometries Bernet et al. [9] and Neacsu et al. [74, 75] describe the problem of yarn impregnation. Here the yarn that consist of many single fibers is imbibed from the outside inwards and can be modeled as an assembly of cylinders. A problem of such a non-flat geometry is that the advancing meniscus traps the fluid in the core of the cylinder assembly. This circumstance is also tackled by Standnes [94] and Mason et al. [68] who consider imbibition of water into oil-wetted cylinders with different aspect ratios.

## 2.4 Linear flow in a tube: Governing equations

In this section the governing equations describing the dynamics of a liquid with a meniscus in a capillary tube or a porous medium are derived. At first, the focus is on capillary rise in cylindrical tubes. The control volume approach as proposed by Levine et al. [58], which was later extended by Stange [95] and Dreyer [30] is applied. This integral method allows to balance properties like mass, energy and momentum inside the control volume. Using these balances - especially the momentum balance - the governing equation of motion can be derived. However, attention must be given to the appropriate selection of boundary conditions, which are introduced in the following section. Fig. 2.2 displays a schematic drawing of a capillary tube in contact with a liquid including the applied control volumes. Here, the fill level is assumed to be constant during the rise process as the size of the reservoir is much larger than the tube. In the later part of this section, the applicability of the derived equation to porous media, and the conversion to a viscous pressure loss described by the Darcy law is given.

### 2.4.1 Meniscus details

In this section some details of the geometric properties of the liquid meniscus are discussed. As shown in Fig. 2.2, the liquid height $h$ is defined as the volume effective height, not the absolute maximum or minimum height of the liquid within a capillary tube. It relates the total volume of liquid in the tube to a liquid column with radius $R$, height $h$ and a flat surface. In setups under the impact of gravity, the surface contour of the meniscus is not a spherical cap, but deformed due to the hydrostatic pressure difference between upper and lower part of the meniscus. For this section however, a spherical cap meniscus (valid for small Bond numbers; see Table 3.3 for definition) is assumed, which also implies that both principal radii of curvature ($R_1$ and $R_2$ which lie perpendicular to each other) are identical for the entire surface. Despite these assumptions, the approach allows to briefly examine the characteristic geometry and lengths of

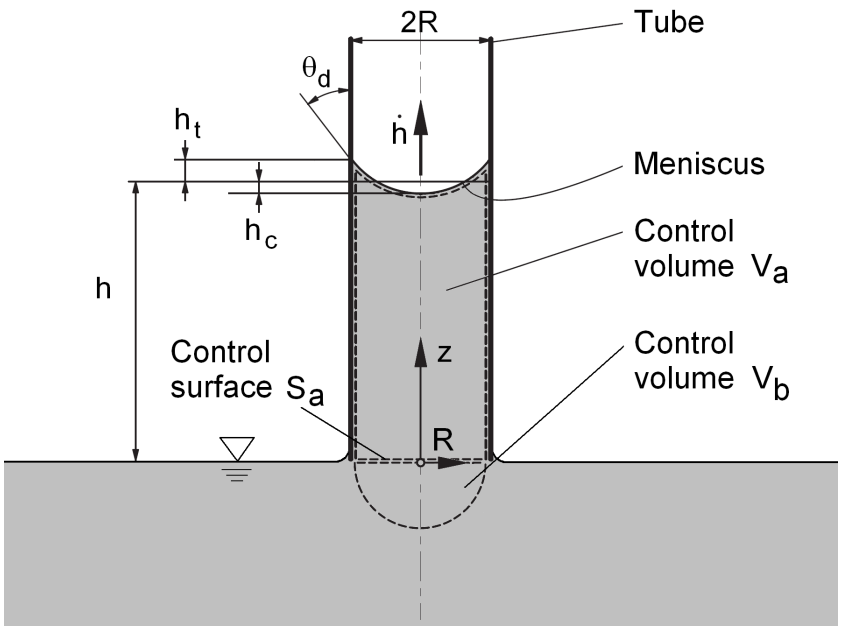


Figure 2.2: Schematic drawing of the geometry. The control volumes and the control surfaces are shown.

a meniscus. Fig. 2.3 displays a sketch of a meniscus and the definitions used in this study. As described by Stange [95] and Dreyer [30] the radius of curvature can be calculated using the tube radius as well as the contact angle $\theta$

$$R_1 \cos(\theta) = R. \tag{2.8}$$

In the following the equation given by Bronstein and Semendjajew [13] for a spherical cap is applied

$$R^2 = h_m(2R_1 - h_m). \tag{2.9}$$

and

$$V_1 = \frac{1}{6}\pi h_m(3R^2 + h_m^2) \tag{2.10}$$

for the spherical cap volume. With Eqs. (2.8) and (2.9) and by canceling out an unphysical solution, the meniscus height can be calculated to be

$$h_m = R\left(\frac{1}{\cos(\theta)} - \tan(\theta)\right). \tag{2.11}$$

To obtain the position of the volume effective height $h$ (by using $h_t$ and $h_c$), one can correlate the volume of the spherical cap with the corresponding cylinder

$$\pi R^2 h_t = \frac{1}{6}\pi h_m(3R^2 + h_m^2). \tag{2.12}$$

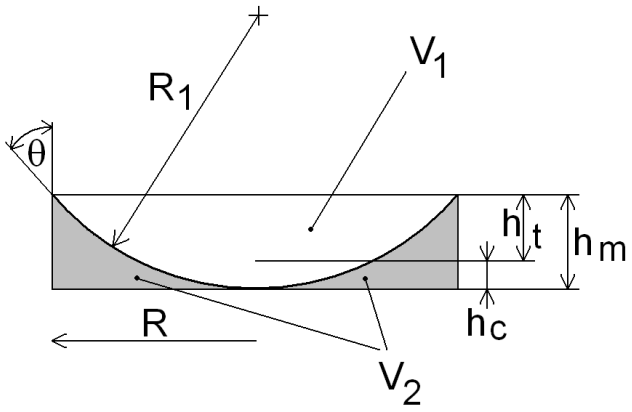


Figure 2.3: Schematic drawing of a liquid meniscus and the relevant lengths. The meniscus equals a spherical cap for small Bond numbers.

Finally the equations read

$$h_t = \frac{1}{6} h_m \left(3 + \frac{h_m^2}{R^2}\right), \tag{2.13}$$

and (see Fig. 2.3)

$$h_c = h_m - h_t. \tag{2.14}$$

### 2.4.2 Mass balance

To investigate the flow velocities one can apply an integral approach (White [106]) for the mass within the control volume $V_a$ (see Fig. 2.2)

$$\left(\frac{dm}{dt}\right)_{syst} = 0 = \frac{d}{dt}\left[\iiint_{V_a} \rho \, dV_a\right] + \iint_{S_a} \rho \, (\vec{v}_{rel} \cdot \vec{n}) dS_a. \tag{2.15}$$

This equation can be rewritten more specified to Fig. 2.2 yielding

$$0 = \frac{d}{dt}\left[\int_0^h \int_0^{2\pi} \int_0^R \rho \, r \, dr \, d\varphi \, dz\right] + \int_0^{2\pi} \int_0^R \rho \, (\vec{v}_{rel} \cdot \vec{n}) r \, dr \, d\varphi. \tag{2.16}$$

Here, $\vec{v}_{rel}$ denotes the relative velocity with respect to the control volume boundary. If the upper boundary is defined to move upwards with the meniscus velocity $\dot{h}$, the relative velocity at the upper boundary is zero. Thus, the balance can be simplified to read

$$0 = \pi \rho R^2 \dot{h} + \pi \rho R^2 (\vec{v}_{rel} \cdot \vec{n}). \tag{2.17}$$

The last term of Eq. (2.17) refers to the inflow at the tube inlet. Therefore, the inflow velocity at the tube bottom has to be equal to $\dot{h}$ to satisfy the mass balance (note that $\vec{v}_{rel} \cdot \vec{n}$ has a negative algebraic sign due to the orientation of the surface).

### 2.4.3 Energy balance

For the energy the integral conservation equation is given by

$$\frac{dE}{dt} = \frac{dQ}{dt} - \frac{dW}{dt} = \frac{d}{dt}\left[\iiint\limits_{V_a}\left(\frac{v^2}{2} + u + \frac{p}{\rho} + gz\right)\rho\, dV_a\right] + \iint\limits_{S_a}\left(\frac{v^2}{2} + u + \frac{p}{\rho} + gz\right)\rho(\vec{v}_{rel}\cdot\vec{n})dS_a, \tag{2.18}$$

which is a rearranged form of the equation given in [106]. $Q$ denotes heat added to the system while $W$ denotes work done by the system. $u$ refers to the inner energy of the fluid, which can be often described by $c_v T$. Analogous to the mass balance, the specific form of Eq. (2.18) for the investigated control volume reads

$$\frac{dE}{dt} = \frac{d}{dt}\left[\int_0^h\int_0^{2\pi}\int_0^R\left(\frac{v^2}{2} + u + \frac{p}{\rho} + gz\right)\rho\, r\, dr\, d\varphi\, dz\right] + \int_0^{2\pi}\int_0^R\left(\frac{v^2}{2} + u + \frac{p}{\rho} + gz\right)\rho(\vec{v}_{rel}\cdot\vec{n})r\, dr\, d\varphi. \tag{2.19}$$

### 2.4.4 Linear momentum balance in z direction

Finally, the integral approach is applied to the momentum as well [106]. This balance is probably the most fundamental and important one since it is the basis for many theoretical approaches to capillary rise

$$\frac{d}{dt}(mv_z)_{syst} = \sum F = \frac{d}{dt}\left[\iiint\limits_{V_a}\rho v_z dV_a\right] + \iint\limits_{S_a}\rho v_z(\vec{v}_{rel}\cdot\vec{n})dS_a = F_{pu} + F_{pl} + F_{fr} + F_{gr}. \tag{2.20}$$

Here, the boundary conditions (see Fig. 2.4) are given by the following forces where

- $F_{pu}$ is the pressure force at the upper boundary
- $F_{pl}$ is the pressure force at the lower boundary (the inlet)
- $F_{fr}$ is the viscous friction losses at the tube wall
- $F_{gr}$ is the volume force due to gravity.

These forces are discussed in more detail in the following sections. Again, one can provide Eq.

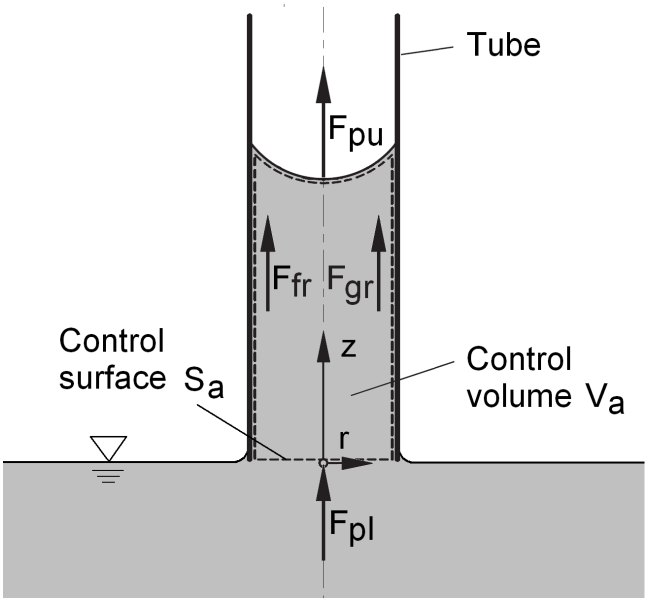


Figure 2.4: Schematic drawing of the forces and boundary conditions acting on the liquid column during the capillary rise process.

(2.20) in a more specific form

$$\frac{d}{dt}\left[\int_0^h\int_0^{2\pi}\int_0^R \rho\,\dot{h}\,r\,dr\,d\varphi\,dz\right] + \int_0^{2\pi}\int_0^R \rho\dot{h}(-\dot{h})r\,dr\,d\varphi = F_{pu} + F_{pl} + F_{fr} + F_{gr}. \tag{2.21}$$

By solving the integrals, one obtains

$$\left[\pi R^2\rho h\ddot{h} + \pi R^2\rho\dot{h}^2\right] - \pi R^2\rho\dot{h}^2 = F_{pu} + F_{pl} + F_{fr} + F_{gr}, \tag{2.22}$$

and

$$\pi R^2\rho h\ddot{h} = F_{pu} + F_{pl} + F_{fr} + F_{gr}. \tag{2.23}$$

#### 2.4.4.1 Pressure force at upper boundary

The force at the upper boundary can be calculated using the pressure integral over the upper control surface

$$F_{pu} = -\int_0^{2\pi}\int_0^R prdrd\varphi = -\int_0^{2\pi}\int_0^R (p_a + \Delta p)rdrd\varphi. \tag{2.24}$$

Here, in addition to the ambient pressure $p_a$, a pressure drop $\Delta p$ across the upper liquid surface has to be considered. It occurs due to the bending of the liquid surface due to capillary action, and it can be calculated using the Young-Laplace equation

$$\Delta p = -\sigma\left(\frac{1}{R_1} + \frac{1}{R_2}\right). \tag{2.25}$$

Here, $R_1$ and $R_2$ (which lies perpendicular to $R_1$) denote the principal radii of the meniscus, see Fig. 2.3. In case of a capillary tube where gravity is not distorting the spherical cap shape of the meniscus (for small Bond numbers) the principal radii can be calculated using the tube radius and the contact angle $\theta_d$

$$R_1 = R_2 = \frac{R}{cos(\theta_d)}. \tag{2.26}$$

Thus, the capillary pressure reads

$$\Delta p = \frac{-2\sigma \cos(\theta_d)}{R}. \tag{2.27}$$

For dynamic systems, one has to keep in mind that the contact angle may not have a static value. Instead it can be shown to depend on the meniscus velocity (the Capillary number Ca). Empirical equations are available for the dynamic contact angle $\theta_d$; e.g. Jiang et al. [48] (based on data by Hoffman [45]) give

$$\frac{\cos(\theta_d) - \cos(\theta_s)}{\cos(\theta_s) + 1} = -\tanh(4.94\,\mathrm{Ca}^{0.702}), \tag{2.28}$$

while Bracke et al. [12] find

$$\frac{\cos(\theta_d) - \cos(\theta_s)}{\cos(\theta_s) + 1} = -2\,\mathrm{Ca}^{0.5}. \tag{2.29}$$

Here, the capillary number is defined as

$$\mathrm{Ca} = \frac{\mu \dot{\mathrm{h}}}{\sigma}. \tag{2.30}$$

In anticipation of later results the maximum theoretical value of $\dot{h}$ can be obtained by differentiation of Eq. (4.3), and herein considering $\theta_s$ as conservative assumption. Thus

$$\mathrm{Ca} = \frac{\mu \dot{\mathrm{h}}}{\sigma} = \mu \sqrt{\frac{2\cos(\theta_\mathrm{s})}{\sigma \rho\, \mathrm{R}}}, \tag{2.31}$$

can be used as a rough estimate to calculate the maximum dynamic contact angle using Eq. (2.28) or Eq. (2.29). However, one should keep in mind that this angle will only develop within the initial moments with high rise velocity. The velocity slows down fairly fast and assuming a constant contact angle becomes feasible for later time stages.

To take into account the time the meniscus takes to develop out of a flat liquid surface the approach given by Stange et al. [96] is applied. Here, a factor $s(t)$ defined by the exponential function

$$s(t) = 1 - e^{-4.6t/t_r} \tag{2.32}$$

is used to retard the capillary pressure. $t_r$ denotes the reorientation time of a flat liquid surface in a cylindric tube suddenly exposed to microgravity as described by Siegert et al. [90]. It is developed from drop tower tests, and defined by

$$t_r = 0.413\sqrt{\frac{\rho R^3}{\sigma}}. \tag{2.33}$$

Finally, the boundary condition for the upper control surface reads

$$F_{pu} = -\pi R^2 \left( p_a - s(t)\frac{2\sigma\cos(\theta_d)}{R} \right). \tag{2.34}$$

#### 2.4.4.2 Pressure force at the lower boundary

Analogous to the upper boundary one can determine the force at the lower boundary by a pressure integral

$$F_{pl} = \int_0^{2\pi}\int_0^{R} p\, r\, dr\, d\varphi = \int_0^{2\pi}\int_0^{R} (p_a - p_{V_b}) r\, dr\, d\varphi. \tag{2.35}$$

Again, $p_a$ denotes the ambient pressure, which - in the momentum balance - later cancels out the ambient pressure at the upper boundary. $p_{V_b}$ refers to the pressure losses in the control volume $V_b$. This pressure loss is calculated by Levine et al. [58] while a refined calculation is provided by Stange [95]. Here, the equation by Stange is used, however, without the terms that are introduced to account for the special experiment design optimized for microgravity. As his liquid reservoir featured a pinned free surface, a decrease in the reservoir pressure had to be taken into account with decreasing fill level. Finally the boundary condition at the tube inlet is given by

$$F_{pl} = \pi R^2 \left( p_a - \left[ \underbrace{\frac{11}{12}\rho R\ddot{h}}_{1} + \underbrace{2\frac{\mu}{R}\dot{h}}_{2} + \underbrace{\frac{23}{24}\rho\dot{h}^2}_{3} \right] \right). \tag{2.36}$$

Here the individual terms denoted 1 to 3, can be understood as follows:

1. Local acceleration of liquid below the tube
2. Viscous loss below the tube
3. Convective acceleration losses

Stange [95] notes, that the precision of the coefficients (e.g. 11/12) used in Eq. (2.36) should not be overestimated. This uncertainty originates from the assumptions used for the determination of $p_{V_b}$, which also explain the slight deviations to the coefficients used by Levine et al. [58] who use 37/36 for term 1 and 7/6 for term 3.

It is important to mention that Eq. (2.36) is only valid for a rising column. For a falling column - as it occurs in oscillating cases - the different flow characteristics at the tube inlet have to be considered. While for the rising column it acts as a sink, a jet or vortex may be emitted for the falling column. Here, for the descending case, the $\dot{h}^2$ term (term 3) is omitted as discussed and experimentally validated by Lorenceau et al. [60]. In this work however, most of the analysis is restricted to cases with a rising column while a falling one is only explicated in chapter 3 where inertia dominated, oscillating cases are discussed.

#### 2.4.4.3 Viscous friction losses at the tube wall

To estimate whether the flow is in the laminar or turbulent regime, the following approach can be applied: The maximum flow velocity is estimated using the analytical solution by Quéré [78], taking into account capillary and inertial forces. It gives a rise with constant velocity (see Eqs. (4.2) and (4.3) for further detail)

$$v_Q = \sqrt{\frac{2\sigma\cos(\theta)}{\rho R}}. \tag{2.37}$$

In this example the fluid properties of silicone fluid SF 0.65 (see Table 2.1) are used, as it features a low viscosity and thus is most critical to reach turbulent flow. The Reynolds number is calculated based on the tube diameter

$$\mathrm{Re_D} = \frac{\mathrm{D\dot{h}}\rho}{\mu} = \frac{2\mathrm{Rv_Q}\rho}{\mu}. \tag{2.38}$$

Applying the conservative assumption of a contact angle of 0° (perfect wetting), one can plot the Reynolds number as a function of tube radius as displayed in Fig. 2.5. It can be observed, that the Reynolds number for the range of radii relevant for this work ($R \leq 1$ mm) is smaller than 2300, so that the flow is in the laminar regime.

Table 2.1: Fluid properties of silicone fluid SF 0.65 (kinematic viscosity of 0.65 cSt) at 25 °C. Source: product data sheet of Dow Corning.

| $\sigma$ [mN/m] | $\rho$ [kg/m$^3$] | $\mu$ [mPas] |
|---|---|---|
| 15.9 | 758 | 0.49 |

For laminar flow the viscous pressure losses in a cylindrical tube with a fully developed flow field can be described by the Hagen-Poiseuille law (see Eq. (2.45)). However, as the liquid enters the tube at the lower boundary, this flow field has not yet developed. The length at

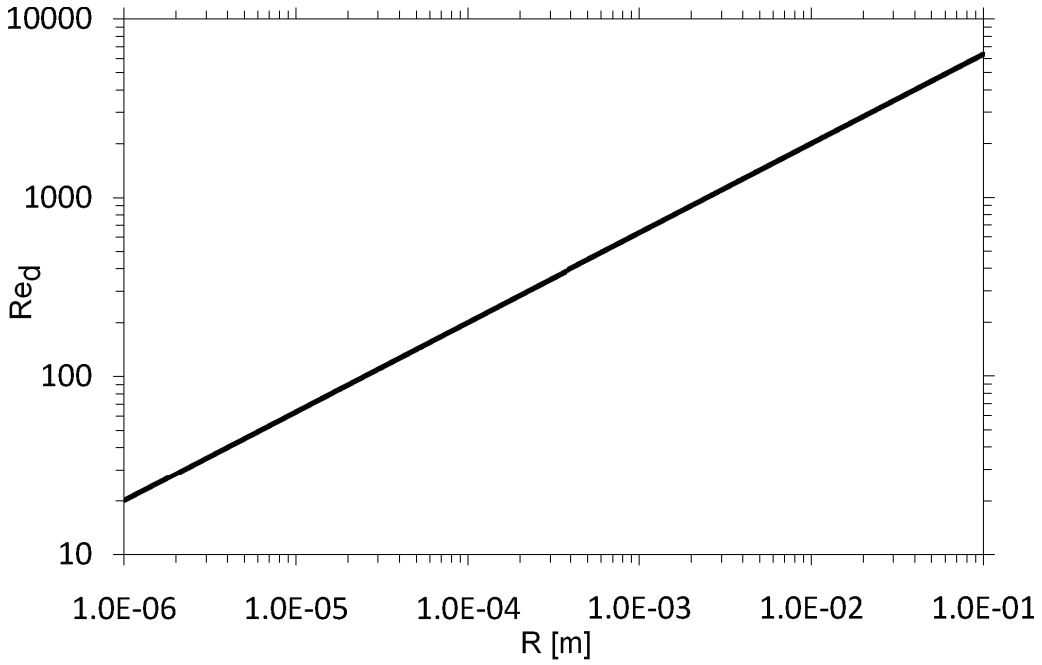


Figure 2.5: Maximum Reynolds number for silicone fluid SF 0.65 as a function of capillary tube radius.

which a fully developed flow can be observed, the entrance length $L_e$, is given by White [106] to be

$$L_e \approx 0.06\, D\, \mathrm{Re_D} = 0.06 \frac{\mathrm{D^2 \dot{h} \rho}}{\mu}. \tag{2.39}$$

During the development of the laminar flow profile an excess pressure drop can be observed. Stange et al. [96] used the model of Sparrow et al. [92] to calculate this excess pressure drop. Including this model, the total viscous pressure losses are given by

$$F_{fr} = -\pi R^2 \left( 8 \frac{\mu}{R^2} h\dot{h} + \frac{1}{2} \rho K_s \dot{h}^2 \right). \tag{2.40}$$

Here, $K_s$ denotes a coefficient for the excess pressure drop given by Sparrow et al. [92] to be

$$K_s(\hat{h}) = \frac{4}{3} + \sum_{i=1}^{25} \frac{8}{\alpha_i^2} \left( e^{-4\alpha_i^2 \hat{h}} - 3 \right) e^{-4\alpha_i^2 \hat{h}}, \tag{2.41}$$

with $\hat{h} = h/(D\, \mathrm{Re}_D)$ and $\alpha_i$ as given by [92].

### 2.4.5 Gravity force and inclination

The volume force developing due to gravity can be accounted for using

$$F_{gr} = -\iiint_{V_a} \rho g \, dV_a = -\int_0^h \int_0^{2\pi} \int_0^R \rho g r \, dr \, d\varphi \, dz = -\pi R^2 \rho g h, \tag{2.42}$$

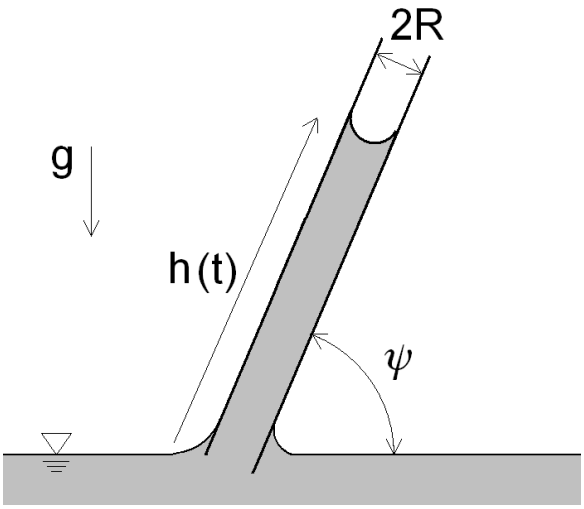


Figure 2.6: Setup with a tube inclined by an angle $\psi$. Note that $h$ denotes the distance covered within the tube.

where $g$ denotes the gravitational acceleration. In setups with gravity, $\psi$ (see Fig. 2.6) is defined to be the angle formed between the inclined tube and the horizontal free liquid surface. It shall be mentioned that for an inclined setup the equations derived in this work keep their validity except for two changes. First of all, the height $h$ is not the absolute height in respect to the horizontal liquid reservoir level but the distance covered within the tube (see Fig. 2.6). The second change concerns the effective gravitational acceleration. Here the inclination has to be considered and $g$ in the equations will have to be replaced by an effective $g_e$ defined by

$$g_e = g \sin \psi. \tag{2.43}$$

#### 2.4.5.1 The full linear momentum balance

By substituting Eqs. (2.34, 2.36, 2.40, 2.42) in Eq. (2.23), one obtains after dividing by $(-\pi R^2)$

$$\underbrace{-\rho h \ddot{h}}_{1} = \underbrace{-\frac{2\sigma \cos(\theta_d)\, s(t)}{R}}_{2} + \underbrace{\frac{11}{12}\rho R \ddot{h}}_{3} + \underbrace{2\frac{\mu}{R}\dot{h}}_{4} + \underbrace{\frac{23}{24}\rho \dot{h}^2}_{5} + \underbrace{8\frac{\mu}{R^2}h\dot{h}}_{6} + \underbrace{\frac{1}{2}\rho K_s \dot{h}^2}_{7} + \underbrace{\rho g h}_{8} \tag{2.44}$$

Here, the individual terms can be understood as follows:

1. Local acceleration of the liquid inside the tube
2. Capillary pressure
3. Local acceleration of the liquid below the tube

4. Viscous losses below the tube
5. Convective flow losses at the entrance of the tube
6. Viscous losses in the tube (Hagen-Poiseuille)
7. Sparrow et al. entrance function
8. Hydrostatic pressure

One can compare Eq. (2.44) to the momentum balance used by Stange et al. [95, 96]. It is found that both solutions are fairly similar, however, deviations can be traced back to the different boundary conditions. Stange et al. include a deviation in height between the liquid surface and the lower tube end (called $h_0$) and have to account for retarding capillary pressure in the liquid reservoir. These terms are not relevant for the cases investigated in this study. Contrary to Stange et al., who used a reservoir featuring a pinned surface optimized for micro-gravity environments, a mathematically infinite reservoir is applied [96].

### 2.4.6 Simplified linear momentum balance and corresponding assumptions

The full momentum balance Eq. (2.44) contains all known terms to describe the movement of the meniscus. However, due to its complexity it can only be solved numerically. Thus, a common approach (as for example applied in [112]) is to simplify Eq. (2.44) by neglecting certain terms. In this context, the solution is restricted to the cases where the neglected terms are actually small compared to the other ones. In the following, some commonly made assumptions are stated and a simplified momentum balance is presented.

- No entry effects: One can see that the entrance length $L_e$ decreases quadratically with decreasing tube diameter $d$ as introduced in Eq. (2.39). In conclusion, the entrance length can be neglected when compared to the meniscus height $h$ for small tube radii. Thus, the Hagen-Poiseuille term in Eq. (2.40) dominates the excess pressure term. As the focus of this work is the description of capillary rise in porous materials or capillary tubes with pore / tube radii of less than one millimeter, the excess pressure term will be - contrary to Stange et al. [96], who investigated tubes of up to 54 mm radius - neglected in the following calculations. Thus the total viscous pressure loss is given by the Hagen-Poiseuille law

$$\frac{\Delta p}{\Delta z} = -\frac{8\mu}{R^2} v_z, \tag{2.45}$$

so that the viscous friction force reads

$$F_{fr} = -\pi R^2 \frac{8\mu}{R^2} h\dot{h}. \tag{2.46}$$

- Constant capillary pressure: For many analytical models the capillary pressure is assumed to be constant. Hence, a static contact angle $\theta$ is used (for a discussion see section 2.4.4.1, Siebold et al. [89] or Fries and Dreyer [36]). Also, the coefficient $s(t)$, describing the development of the meniscus in the first initial moments - and thus the capillary pressure - is dropped.

- Viscous and local acceleration ($\ddot{h}$) terms in the liquid reservoir are neglected as they are typically (for small capillaries) small compared to the losses in the tube itself. Also the factor 23/24 of the convective acceleration term is dropped as its accuracy should not be overestimated (see section 2.4.4.2).

With these assumptions the equation of motion is given by (e.g. Bosanquet [11] or Zhmud et al. [112])

$$-\rho h\ddot{h} - \rho\dot{h}^2 = -\rho\frac{d(h\dot{h})}{dt} = -\frac{2\sigma\cos(\theta)}{R} + \frac{8\mu h}{R^2}\dot{h} + \rho g h. \tag{2.47}$$

In this equation, the momentum change (local and convective, left hand side) is balanced by the capillary pressure, the viscous forces and the hydrostatic pressure (left to right). An alternative is to rearrange the terms of Eq. (2.47) to highlight their physical meaning

$$\frac{2\sigma\cos(\theta)}{R} = \rho\frac{d(h\dot{h})}{dt} + \frac{8\mu h}{R^2}\dot{h} + \rho g h. \tag{2.48}$$

In Eq. (2.48) one can see that the capillary pressure (left hand side) is balanced by the sum of inertial, viscous and hydrostatic forces. All terms on the right hand side are depending on $h$ or $\dot{h}$, whereas the left hand side remains constant during the entire rise process.

## 2.5 Equation for porous media using the Darcy law

To derive an equation for the capillary rise of liquid in a porous medium the pore structure parameters and the analogy between capillary dominated flow in a cylindrical tube and in a porous medium as introduced in section 2.2 are considered. With the pore structure parameters $K$, $R_s$ and $\phi$ the momentum balance Eq. (2.47) can be rewritten

$$-\rho\frac{d(h\dot{h})}{dt} = -\frac{2\,\sigma\cos(\theta)}{R_s} + \frac{\phi}{K}\mu h\dot{h} + \rho g h. \tag{2.49}$$

Here, valid for small pore Reynolds numbers, the viscous losses are expressed by the Darcy law neglecting the convective terms of the Forchheimer equation as done by Symons [98] and Marmur [66] in this context. The radius $R$, used to calculate the capillary pressure in tubes, has been replaced by the static radius $R_s$ which can be calculated from the maximum obtainable "static" height. One also assumes that the porous medium features a uniform pore size, which actually applies for few cases only. Nevertheless, this simplified model can be successfully applied to describe capillary rise in porous media (see chapter 7).

## 2.6 Radial flow in porous media: Governing equations

In the following the relations for a radial capillary setup are investigated. This section is not considered being state of the art, yet it is placed within that chapter as it is a logical extension to the previous work. The approach is fairly analogous to the method introduced in the section for linear transport, however, there are some differences due to the radial motion which is addressed in the following. Figure 2.7 displays a drawing of the basic geometry and the boundary conditions.

### 2.6.1 Mass balance

Analogous to linear transport, the integral mass balance (White [106]) reads

$$\left(\frac{dm}{dt}\right)_{syst} = 0 = \frac{d}{dt}\left[\iiint_{V_a} \rho \, dV_a\right] + \iint_{S_a} \rho(\vec{v}_{rel} \cdot \vec{n}) dS_a. \tag{2.50}$$

For the control volume $V_a$ as introduced in Fig. 2.7 ($H$ denotes thickness of porous structure) one can write

$$0 = \frac{d}{dt}\left[\int_0^H \int_0^{2\pi} \int_{r_0}^{r_f} \rho \, r \, dr \, d\varphi \, dz\right] + \int_0^H \int_0^{2\pi} \rho(\vec{v}_{rel} \cdot \vec{n}) r \, d\varphi \, dz. \tag{2.51}$$

Again, $\vec{v_{rel}}$ denotes the relative velocity with respect to the boundary. If the outer boundary of the control system is defined to move with the wicking front velocity $\dot{r}_f$ the relative velocity at the outer boundary is zero, and the balance can be simplified to read

$$0 = 2\pi H \rho \, r_f \dot{r}_f + 2\pi H \rho \, r_0 (\vec{v}_{rel} \cdot \vec{n}). \tag{2.52}$$

From this, the following velocity distribution within the radial structure can be calculated

$$r_0 v_0 = r v_r(r) = r_f \dot{r}_f. \tag{2.53}$$

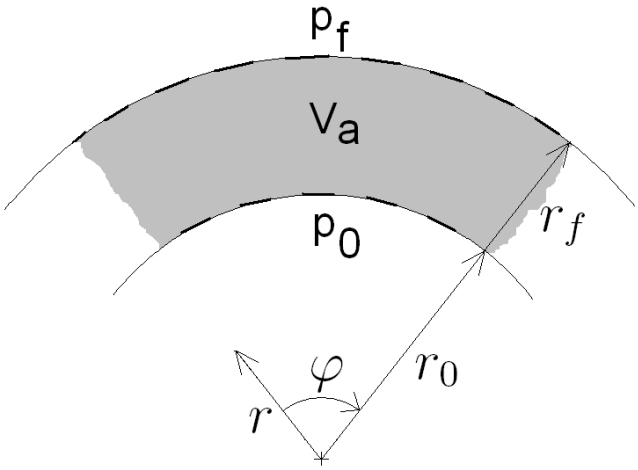


Figure 2.7: Schematic drawing of the boundary conditions for radial flow.

### 2.6.2 Linear momentum balance in radial direction

To analyze the motion of the liquid front, the Navier-Stokes equation for cylindrical coordinates in radial ($r$) direction can be used. It reads as follows [93]

$$\rho\left[\frac{\partial v_r}{\partial t}+v_r\frac{\partial v_r}{\partial r}+v_z\frac{\partial v_z}{\partial z}+\frac{1}{r}\left(v_\varphi\frac{\partial v_r}{\partial \varphi}-v_\varphi^2\right)\right]=\rho g_r-\frac{\partial p}{\partial r}-\mu\frac{\phi}{K}v_r, \tag{2.54}$$

where the last term is the Darcy law replacing the viscous momentum transport. Several terms of Eq. (2.54) can be canceled out, as the problem described is one dimensional, and all derivations and velocities in $\varphi$ and $z$ direction are zero. Also, for a horizontal setup, the gravity force can be set to zero. One obtains

$$\rho\left[\frac{dv_r}{dt}+v_r\frac{dv_r}{dr}\right]+\mu\frac{\phi}{K}v_r=-\frac{dp}{dr}. \tag{2.55}$$

By multiplying with $dr$ and integrating, the equation can be rearranged to

$$\frac{d}{dt}\int_{r_0}^{r_f}\rho\, v_r\, dr+\int_{v_0}^{v_f}\rho\, v_r\, dv_r+\int_{r_0}^{r_f}\mu\frac{\phi}{K}v_r\, dr=-\int_{p_0}^{p_f}dp=-p_f+p_0. \tag{2.56}$$

#### 2.6.2.1 Pressure at the wicking front

The pressure at the wicking front can be calculated using the Young-Laplace equation

$$p_f=p_a-s(t)\frac{2\sigma\cos(\theta_d)}{R_s}. \tag{2.57}$$

Here, $R_s$ denotes the static pore radius (or "capillary pressure effective radius") of the medium, and $p_a$ refers to the ambient pressure.

#### 2.6.2.2 Pressure at the inner boundary

Analogous to the outer boundary one can determine the pressure at the inner boundary by

$$p_0 = p_a - p_{wick}. \tag{2.58}$$

Here, $p_{wick}$ refers to viscous losses that may occur before the liquid enters the radial screen, e.g. in a feeding wick (see Fig 8.1).

#### 2.6.2.3 The final equation

By substituting Eqs. (2.57, 2.58) in Eq. (2.56), one obtains

$$\frac{d}{dt}\left[\int_{r_0}^{r_f} \rho\, v_r\, dr\right] + \int_{v_0}^{v_f} \rho\, v_r\, dv_r + \mu\frac{\phi}{K}\int_{r_0}^{r_f} v_r\, dr = s(t)\frac{2\sigma\cos(\theta_d)}{R_s} - p_{wick}. \tag{2.59}$$

In the following the parameter $s(t)$ describing the time for the meniscus to develop and the dynamic behavior of the contact angle $\theta$ shall be neglected. By also neglecting the viscous losses in the feeding wick - for this case its permeability has to be much higher than the permeability of the porous screen - Eq. (2.59) can be rearranged to

$$\underbrace{\frac{2\sigma\cos(\theta)}{R_s}}_{\text{capillary pressure}} = \underbrace{\mu\frac{\phi}{K}\int_{r_0}^{r_f} v_r(r)\, dr}_{\text{viscous term}} + \underbrace{\frac{d}{dt}\left[\int_{r_0}^{r_f} \rho\, v_r(r)\, dr\right]}_{\text{local acceleration}} + \underbrace{\int_{v_0}^{v_f} \rho\, v_r\, dv_r}_{\text{convective acceleration}}. \tag{2.60}$$

Due to the mass balance given in Eq. (2.53)

$$v_r(r) = \frac{1}{r} r_f \dot{r}_f, \tag{2.61}$$

so one can substitute $v_r(r)$ and rearrange to obtain

$$\frac{2\sigma\cos(\theta)}{R_s} - \mu\frac{\phi}{K} r_f \frac{dr_f}{dt}\ln\left(\frac{r_f}{r_0}\right) - \rho\left(\frac{d}{dt}\left[r_f\frac{dr_f}{dt}\ln\left(\frac{r_f}{r_0}\right)\right] + \left(\frac{dr_f}{dt}\right)^2\left[\frac{1}{2} - \frac{r_f^2}{2r_0^2}\right]\right) = 0. \tag{2.62}$$

# Chapter 3

# Dimensionless scaling methods for capillary rise

## 3.1 Introduction

The following chapter is based on the publication "Dimensionless scaling methods for capillary rise" by N. Fries and M. Dreyer [37]. To obtain a better understanding of a problem, its dimensionless consideration is always of interest. Here, the Buckingham $\pi$ theorem [17] can be used to obtain appropriate dimensionless scalings. In literature there are several papers applying dimensionless numbers to the problem of capillary rise. Ichikawa and Satoda [47] focus on experiments with horizontal capillaries, Dreyer et al. [31] and Stange et al. [95, 96] on capillaries in a microgravity environment. There also exist studies involving gravity, thus, leading to different scaling approaches e.g. by Quéré et al. [78, 79], Marmur and Cohen [67], Zhmud et al. [112], Lee and Lee [56] or Fries and Dreyer [35, 36]. McKinley [71] investigates dimensionless groups for free surface flows with a focus on complex fluids. In this chapter a systematic approach to dimensionless scaling of capillary rise is followed, and the different derived options are compared.

The basis for the dimensionless scalings is the differential equation of motion of liquid inside a capillary tube. It can be derived by solving an integral balance of the linear momentum in an appropriate control volume as shown in chapter 2 "Theory of capillary driven flow". The simplified equation (see chapter 2.4.6) for a capillary tube reads as follows (see Eq. (2.47))

$$-\rho\frac{d(h\dot{h})}{dt} = -\frac{2\sigma\cos(\theta)}{R} + \frac{8\mu h}{R^2}\dot{h} + \rho g h \quad (\text{for } \dot{h} > 0). \tag{3.1}$$

It is important to note that Eq. (3.1) is only valid for a rising column. For a falling column - as it occurs in oscillating cases - the different flow characteristics at the tube inlet have to be considered. While for the rising column it acts as a sink, a jet or vortex may be emitted for the falling column. Here, for the descending case, the $\dot{h}^2$ term included in the left hand side of Eq. (3.1) is omitted to obtain

$$-\rho h\ddot{h} = -\frac{2\sigma\cos(\theta)}{R} + \frac{8\mu h}{R^2}\dot{h} + \rho g h \quad (\text{for } \dot{h} < 0) \tag{3.2}$$

as shown by Lorenceau et al. [60].

For porous media the Darcy law can be used to describe the viscous pressure loss (see Eq. (2.49))

$$-\rho\frac{d(h\dot{h})}{dt} = -\frac{2\sigma\cos(\theta)}{R} + \frac{\phi\mu h}{K}\dot{h} + \rho g h \quad (\text{for } \dot{h} > 0). \tag{3.3}$$

## 3.2 Dimensionless scaling

In this section the different dimensionless scaling options will be discussed. The Buckingham $\pi$ theorem and the approach described by White [106] is used. The relevant definitions shall be introduced briefly:

- Dimensional variables are the basic output of the experiment, and normally the ones to be shown in a diagram. They vary during a given run. In the current case $h$ and $t$.
- Dimensional parameters affect the variables and may vary from case to case, however, remain constant during a given run. In the current case $a$, $b$ and $c$, see Eqs. (3.4), (3.5) and (3.6) below.
- Fundamental units are the units of the variables and parameters e.g. meter, kilogram, second.
- Scaling parameters are chosen to convert the variables to a dimensionless form. In the current case: two can be chosen.
- Basic parameter is the - in the current case one - remaining parameter.
- Dimensionless variables are the variables made dimensionless by the scaling parameters.
- Dimensionless basic parameter is the basic parameter made dimensionless using the scaling parameters.

In a graphic representation of the dimensionless solution the axes are the dimensionless variables, while the dimensionless basic parameter is varied to plot a set of curves [106] (e.g. see Fig. 3.1). With varying dimensionless basic parameter the influence of the basic parameter (and the corresponding force) can be observed. Regarding Eqs. (3.1) and (3.3) one may define the following dimensional parameters

$$a = \frac{\rho R}{2\sigma\cos(\theta)} \mathrel{\widehat{=}} \frac{\rho R_s}{2\sigma\cos(\theta)}, \tag{3.4}$$

$$b = \frac{4\mu}{R\sigma\cos(\theta)} \mathrel{\widehat{=}} \frac{\mu}{2\sigma\cos(\theta)}\frac{\phi R_s}{K}, \tag{3.5}$$

$$c = \frac{\rho g R}{2\sigma\cos(\theta)} \mathrel{\widehat{=}} \frac{\rho g R_s}{2\sigma\cos(\theta)}. \tag{3.6}$$

Due to the analogy, both the cylindrical capillary tube and the version using the pore structure parameters $K$, $R_s$ and $\phi$ is given. However, in favor of readability, the latter will not be explicated in the further text. Please note that the parameters $a$, $b$ and $c$ are not identical to those applied in [35, 36]. Using the introduced dimensional parameters one can rearrange Eqs. (3.1) and (3.3) to obtain

$$\underbrace{a\frac{d\left(h\dot{h}\right)}{dt}}_{inertial} + \underbrace{bh\dot{h}}_{viscous} + \underbrace{ch}_{hydrostatic} = 1. \tag{3.7}$$

It can now be observed that the momentum balance is much more clearly arranged and that each dimensional parameter corresponds to a single term: $a$ - inertia, $b$ - viscous effects and $c$ - hydrostatic effects. Table 3.1 summarizes the three different scaling options that will be examined one by one in the next sections.

Table 3.1: The different dimensionless scaling options.

| Option | Basic parameter | Scaling parameters |
|---|---|---|
| 1 | a (inertia) | b (viscosity) and c (gravity) |
| 2 | b (viscosity) | a (inertia) and c (gravity) |
| 3 | c (gravity) | a (inertia) and b (viscosity) |

### 3.2.1 Viscous effects and gravity as scaling forces (index †)

Here, $b$ (viscous effects) and $c$ (gravity) are used as scaling parameters, the remaining parameter $a$ (inertia) is used as basic parameter. The resulting dimensionless variables and the

dimensionless basic parameter are derived by applying the Buckingham $\pi$ theorem as shown in section 3.5

$$\pi_1^\dagger = h^\dagger = ch = \frac{\rho g R}{2\sigma\cos(\theta)}h, \tag{3.8}$$

and

$$\pi_2^\dagger = t^\dagger = \frac{c^2 t}{b} = \frac{\rho^2 g^2 R^3}{16\mu\sigma\cos(\theta)}t. \tag{3.9}$$

These two dimensionless variables have been used by Zhmud et al. [112] and Fries and Dreyer [35]. The dimensionless basic parameter reads as follows

$$\pi_3^\dagger = \Omega = \sqrt{\frac{b^2}{ac^2}} = \sqrt{\frac{128\sigma\cos(\theta)\mu^2}{\rho^3 g^2 R^5}}. \tag{3.10}$$

According to Quéré et al. [79], the basic dimensionless parameter $\pi_3^\dagger$ is denoted as $\Omega$. Here, $\Omega$ can be used to measure the influence of inertia. Fig. 3.1 shows that for decreasing $\Omega$ (increasing inertia, see arrow) the oscillations and the overshoot increase. This is consistent with Quéré et al. who find oscillations to occur for $\Omega \leq 2$. It is interesting to note that for all three scaling options presented in this article $\Omega$ ($=\pi_3$) is mathematically equal, however, its meaning changes from scaling to scaling [106]. Thus $\Omega$ always reflects the influence of the chosen basic parameter. For example, as will be shown later in further detail, $\Omega$ can become infinite in two limits which are physically very different: For a non inertial case (the Washburn limit) with $a = 0$, and for the no gravity case (the Bosanquet limit) with $c = 0$.

The numerical solutions of the momentum balance as shown in Figs. 3.1, 3.2 and 3.3 have been obtained by using an implicit Runge-Kutta algorithm with the initial conditions $h(t = 0) = 0$ and $\dot{h}(t = 0) = 0$. The case differentiation for $\dot{h} > 0$ and $\dot{h} < 0$ was programmed by including an $if()$ command into the code.

Applying the scalings presented above the resulting dimensionless momentum balances read

$$\frac{1}{\Omega^2}\frac{d\left(h^\dagger \frac{dh^\dagger}{dt^\dagger}\right)}{dt^\dagger} + h^\dagger\frac{dh^\dagger}{dt^\dagger} + h^\dagger = 1 \quad (\text{for } \dot{h^\dagger} > 0) \tag{3.11}$$

and

$$\frac{1}{\Omega^2}\frac{d^2h^\dagger}{dt^{\dagger\,2}} + h^\dagger\frac{dh^\dagger}{dt^\dagger} + h^\dagger = 1 \quad (\text{for } \dot{h^\dagger} < 0). \tag{3.12}$$

For $\Omega \to \infty$ (no inertia), Eq. (3.11) can be solved analytically with the solution given in implicit form by Washburn [104]

$$t^\dagger = -h^\dagger - \ln(1 - h^\dagger), \tag{3.13}$$

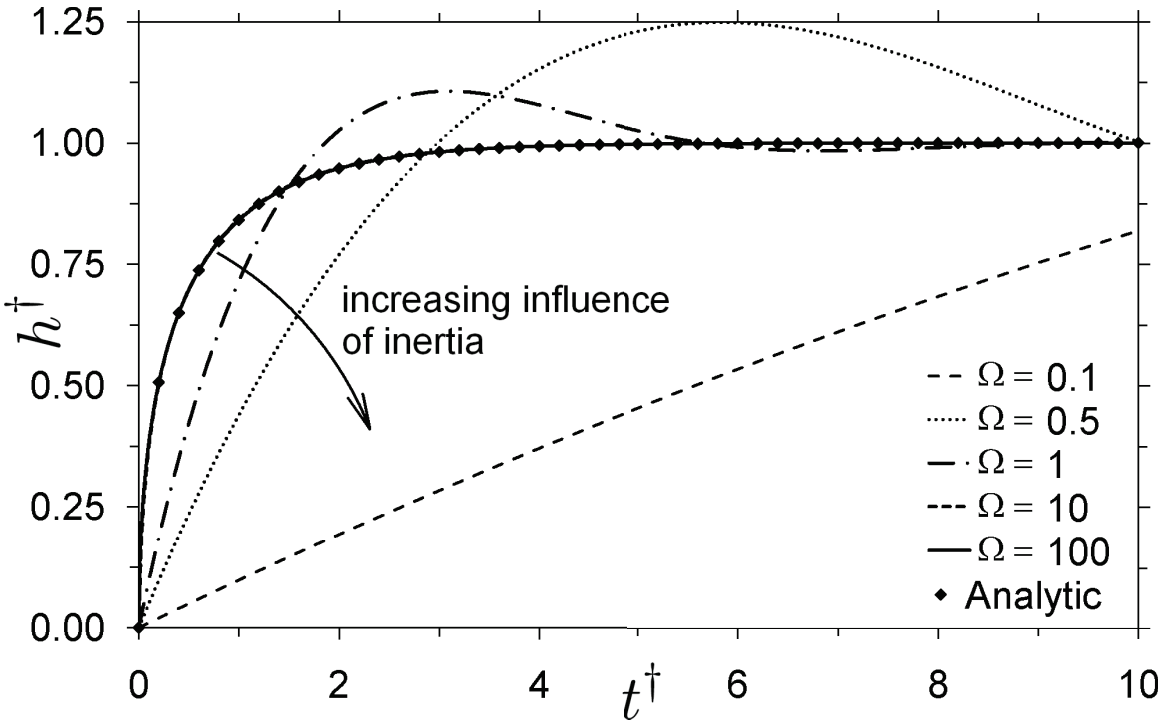


Figure 3.1: Plot showing the dimensionless numerical solution of Eqs. (3.11) and (3.12). Viscosity and gravity are the scaling forces, inertia is the basic parameter for the set of curves. The points refer to the analytic solution Eq. (3.14) for $\Omega \to \infty$ by Washburn. Note that the curve for $\Omega = 10$ lies above the curve for $\Omega = 100$ and is not visible.

and in explicit form by Barry et al. [5] and Fries and Dreyer [35]

$$h^\dagger = 1 + W(-e^{-1-t^\dagger}). \tag{3.14}$$

Here, $W(x)$ denotes the Lambert W function (see section 5.3.1). By numerical means the deviation between the analytic and the numerical solution is found to be smaller than 5 % for $\Omega \geq 7.9$ and $t^\dagger \geq 0.1$.

### 3.2.2 Inertia and gravity as scaling forces (index ‡)

For this case one obtains - analogous to the procedure as shown in section 3.5 - the following dimensionless variables

$$\pi_1^\ddagger = h^\ddagger = ch = \frac{\rho g R}{2\sigma\cos(\theta)}h, \tag{3.15}$$

and

$$\pi_2^\ddagger = t^\ddagger = \sqrt{\frac{c^2}{a}}\,t = \sqrt{\frac{\rho g^2 R}{2\sigma\cos(\theta)}}\,t. \tag{3.16}$$

These dimensionless variables have been used by Quéré et al. [79]. The dimensionless basic parameter reads

$$\pi_3^\ddagger = \Omega = \sqrt{\frac{b^2}{ac^2}} = \sqrt{\frac{128\sigma\cos(\theta)\mu^2}{\rho^3 g^2 R^5}}. \tag{3.17}$$

Here, $\Omega$ can be used to determine the influence of viscous effects. Thus, it can be observed that the oscillations decrease with increasing $\Omega$ (increasing viscosity, see arrow in Fig. 3.2). The dimensionless momentum balances read

$$\frac{d\left(h^\ddagger \frac{dh^\ddagger}{dt^\ddagger}\right)}{dt^\ddagger} + \Omega h^\ddagger \frac{dh^\ddagger}{dt^\ddagger} + h^\ddagger = 1 \quad (\text{for } \dot{h^\ddagger} > 0) \tag{3.18}$$

and

$$\frac{d^2 h^\ddagger}{dt^{\ddagger\,2}} + \Omega h^\ddagger \frac{dh^\ddagger}{dt^\ddagger} + h^\ddagger = 1 \quad (\text{for } \dot{h^\ddagger} < 0). \tag{3.19}$$

For $\Omega \to 0$ (no viscous effects), Eq. (3.18) can be solved analytically with the solution given by Quéré [78] to be

$$h^\ddagger = t^\ddagger \left(1 - \frac{t^\ddagger}{6}\right), \tag{3.20}$$

valid for $0 \leq t^\ddagger \leq 3$. By numerical means, the deviation between the analytic and the numerical solution is found to be smaller than 5 % for $\Omega \leq 0.11$ and $0 \leq t^\ddagger \leq 3$.

### 3.2.3 Inertia and viscous effects as scaling forces (index $*$)

With this choice one obtains - analogous to the procedure as shown in section 3.5 - the dimensionless variables as described in following: The first one reads

$$\pi_1^* = \sqrt{\frac{b^2}{a}}\, h = \sqrt{\frac{32\mu^2}{\rho R^3 \sigma\cos(\theta)}}\, h. \tag{3.21}$$

To be consistent with the scaling by Ichikawa and Satoda [47], and to obtain a more convenient form of analytic solution (see Eq. (3.27)) one can divide $\pi_1^*$ by $\sqrt{2}$ to obtain

$$h^* = \frac{b}{\sqrt{2}a}\, h = \sqrt{\frac{16\mu^2}{\rho R^3 \sigma\cos(\theta)}}\; h. \tag{3.22}$$

The second dimensionless variable reads

$$\pi_2^* = t^* = \frac{b}{a} t = \frac{8\mu}{\rho R^2} t, \tag{3.23}$$

and the dimensionless basic parameter

$$\pi_3^* = \Omega = \sqrt{\frac{b^2}{ac^2}} = \sqrt{\frac{128\sigma\cos(\theta)\mu^2}{\rho^3 g^2 R^5}}. \tag{3.24}$$

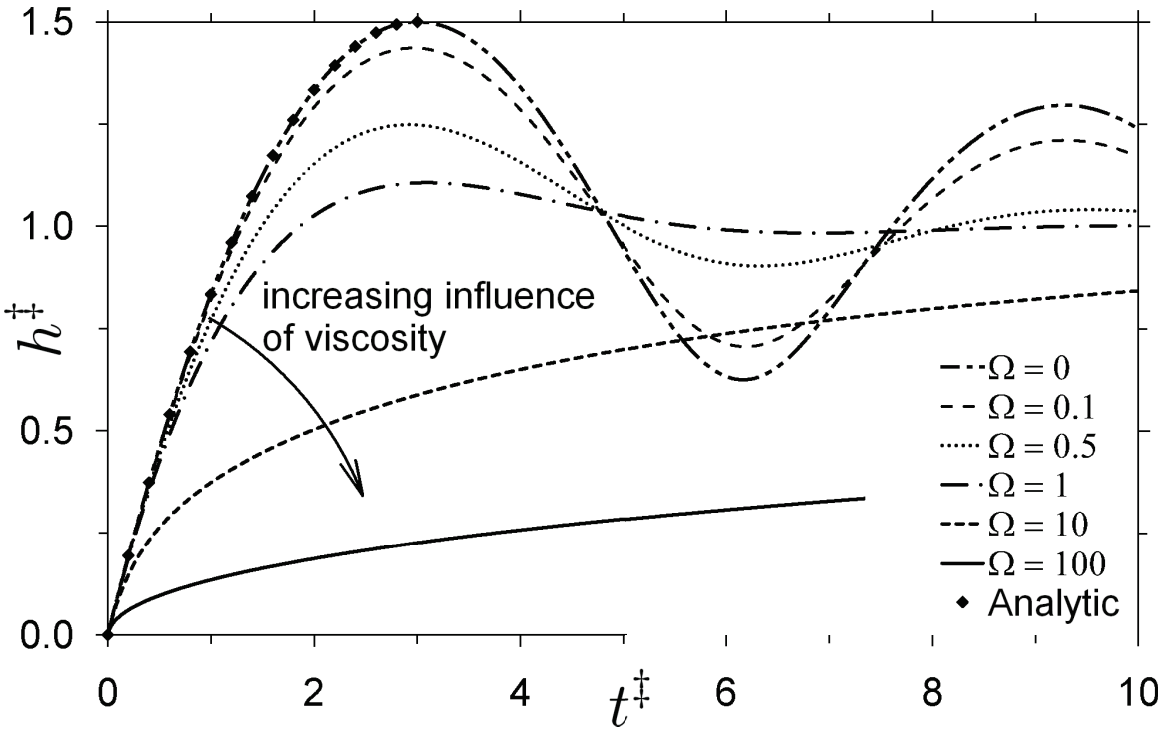


Figure 3.2: Plot showing the dimensionless numerical solution of Eqs. (3.18) and (3.19). Inertia and gravity are the scaling forces, viscosity is the basic parameter for the set of curves. The points refer to the analytic solution Eq. (3.20) for $\Omega \to 0$ by Quéré.

Here, $\Omega$ can be used to measure the influence of hydrostatic effects. Thus, it can be observed that the oscillations increase and the maximum height decreases with decreasing $\Omega$ (increasing hydrostatic effect, see arrow in Fig. 3.3). Using the presented scaling the dimensionless momentum balances can be given as

$$2\frac{d\left(h^*\frac{dh^*}{dt^*}\right)}{dt^*} + 2h^*\frac{dh^*}{dt^*} + \frac{\sqrt{2}}{\Omega}h^* = 1 \quad (\text{for } \dot{h^*} > 0) \tag{3.25}$$

and

$$2\frac{d^2h^*}{dt^{*\,2}} + 2h^*\frac{dh^*}{dt^*} + \frac{\sqrt{2}}{\Omega}h^* = 1 \quad (\text{for } \dot{h^*} < 0). \tag{3.26}$$

For $\Omega \to \infty$ (no hydrostatic effects), Eq. (3.25) can be solved analytically with the solution given by Bosanquet [11] to be

$$h^* = \sqrt{t^* - (1 - e^{-t^*})}. \tag{3.27}$$

By numerical means the deviation between the analytic and the numerical solution is found to be smaller than 5 % for $\Omega \geq 96$ and $t^* \leq 100$.

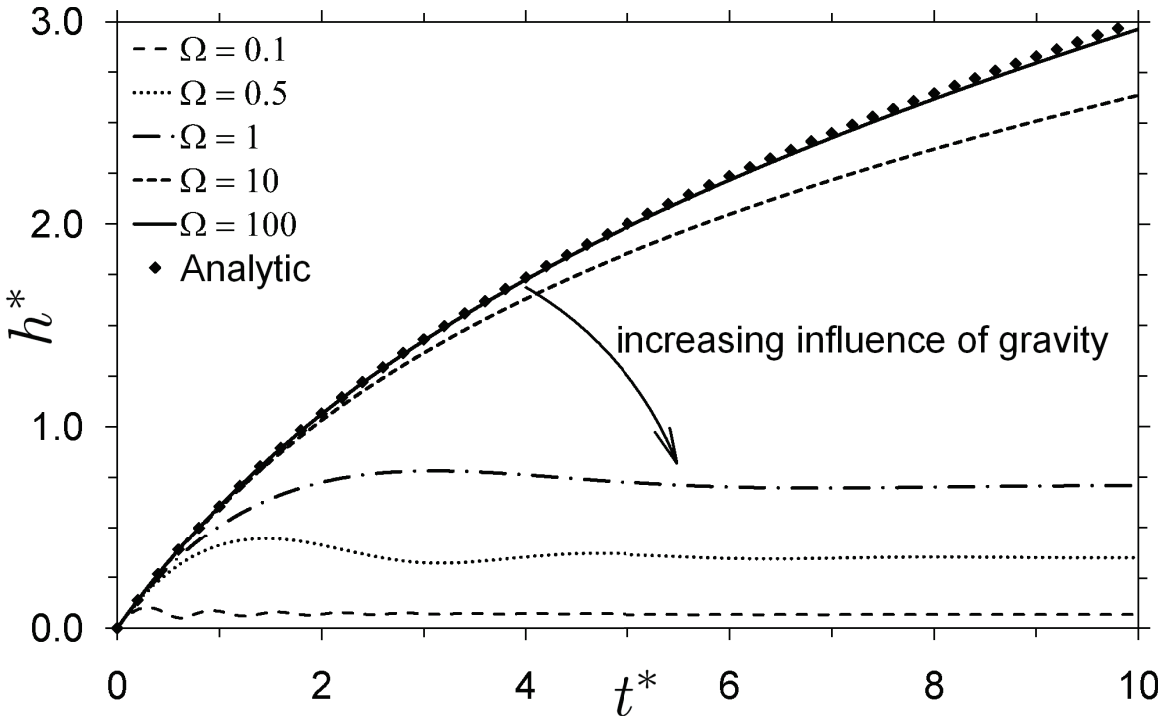


Figure 3.3: Plot showing the dimensionless numerical solution of Eqs. (3.25) and (3.26). Inertia and viscosity are the scaling forces, gravity is the basic parameter for the set of curves. The points refer to the analytic solution Eq. (3.27) for $\Omega \to \infty$ by Bosanquet.

## 3.3 Discussion

In Table 3.2 the different dimensionless variables and $\Omega$ are examined further on. It can be observed that they are related to the indicated forces and well known dimensionless numbers as displayed in Table 3.3. In Table 3.2, $\cos(\theta)$ appears as an independent dimensionless parameter. Note that the three figures (Figs. 3.1, 3.2, 3.3) shown in the previous sections all represent solutions of the same five cases (equal $\Omega$). Due to the different scalings however, their shapes bear no direct resemblance. From a general point of view, the three scaling options are all equivalent for describing the problem of capillary rise. However, for some cases there can be a benefit of choosing a certain scaling method. In the following, two of these cases shall be discussed:

All forces are effective

To investigate the impact of a certain parameter one can choose it to be the basic parameter. Then the two remaining parameters must act as scaling parameters. If, for example, viscous effects and gravity are chosen to be scaling forces (parameters), then $\Omega$, the basic parameter for the set of curves, will reflect the influence of inertia.

Table 3.2: Overview of dimensionless variables and $\Omega$. See Table 3.3 for description of dimensionless numbers.

| Variable | Dimensionless numbers | $\sim$ Forces |
|---|---|---|
| $h^{\dagger}$ | $\sim \frac{\mathrm{Bo}}{\cos(\theta)}$ | $\frac{\text{gravity}}{\text{surface tension}}$ |
| $t^{\dagger}$ | $\sim \frac{\mathrm{Bo}^2}{\mathrm{Ca}\,\cos(\theta)}$ | $\frac{(\text{gravity})^2}{\text{viscous}\ \cdot\ \text{surface tension}}$ |
| $h^{\ddagger}$ | $\sim \frac{\mathrm{Bo}}{\cos(\theta)}$ | $\frac{\text{gravity}}{\text{surface tension}}$ |
| $t^{\ddagger}$ | $\sim \sqrt{\frac{\mathrm{Bo}}{\mathrm{Fr}^2\cos(\theta)}}$ | $\sqrt{\frac{(\text{gravity})^3}{(\text{inertia})^2\ \cdot\ \text{surface tension}}}$ |
| $h^{*}$ | $\sim \frac{\mathrm{Oh}}{\sqrt{\cos(\theta)}}$ | $\frac{\text{viscous}}{\sqrt{\text{inertia}\ \cdot\ \text{surface tension}}}$ |
| $t^{*}$ | $\sim \frac{1}{\mathrm{Re}}$ | $\frac{\text{viscous}}{\text{inertia}}$ |
| $\Omega$ | $\sim \sqrt{\frac{\cos(\theta)}{\mathrm{Bo}\,\mathrm{Ga}}}$ | $\frac{\sqrt{\text{surface tension}\ \cdot\ \text{viscous}}}{\text{gravity}}$ |

One of the forces can be neglected

For some cases it is possible to neglect the influence of a certain force, e.g. in microgravity the hydrostatic term can be neglected. This also applies for experiments where only the initial time period of the capillary rise is investigated, while for later time stages in small capillaries one can usually neglect inertia. The neglected force can not be used as a scaling force, thus the one remaining scaling option should be chosen. In this case the neglected force will act as basic parameter for the set of curves. However, the plotted solution is reduced to a single curve as the basic dimensionless parameter $\Omega$ will equal 0 or $\infty$.

## 3.4 Conclusion

This chapter has demonstrated that one can use the Buckingham $\pi$ theorem to systematically derive three different scaling options. Each option consists of a set of two dimensionless vari-

Table 3.3: List of the relevant dimensionless numbers for capillary rise.

| Abbrev. | Name | Equation | Forces |
|---|---|---|---|
| Bo | Bond number | $\frac{\rho g R^2}{\sigma}$ | $\frac{\text{gravity}}{\text{surface tension}}$ |
| Ga | Galileo number | $\frac{g R^3 \rho^2}{\mu^2}$ | $\frac{\text{gravity}}{\text{viscous}}$ |
| Ca | Capillary number | $\frac{\mu v}{\sigma} \sim \frac{\mu R}{\sigma t}$ | $\frac{\text{viscous}}{\text{surface tension}}$ |
| Oh | Ohnesorge number | $\frac{\mu}{\sqrt{R \rho \sigma}}$ | $\frac{\text{viscous}}{\sqrt{\text{inertia} \cdot \text{surface tension}}}$ |
| Re | Reynolds number | $\frac{\rho R v}{\mu} \sim \frac{\rho R^2}{\mu t}$ | $\frac{\text{inertia}}{\text{viscous}}$ |
| Fr | Froude number | $\frac{v}{\sqrt{gR}} \sim \sqrt{\frac{R}{g t^2}}$ | $\frac{\text{inertia}}{\text{gravity}}$ |
| $\cos(\theta)$ | Contact angle | - | - |

ables and one basic dimensionless parameter. The different options found are discussed and numerical as well as analytic solutions of the momentum balance are shown in dimensionless form. Generally, the different scaling options are absolutely equivalent in terms of describing the problem. However, using the right scaling can help to identify the influence of a certain parameter to be investigated. Also for some special cases (e.g. microgravity) the choice is limited to a single scaling method. These findings can help to choose an appropriate scaling to present experimental data of capillary rise, and they may also help to systematically plan an experimental campaign in advance by defining the experimental matrix to be investigated.

## 3.5 Excursion - Applying the Buckingham $\pi$ Theorem

The following section aims to clarify the procedure deriving the scalings. As an example the choice has been made that $a$ (inertia) shall be the basic parameter and $b$ (viscosity) and $c$ (gravity) shall be the scaling parameters.

One finds five (5) dimensional units:

$a$ $[\frac{\mathrm{s}^2}{\mathrm{m}^2}]$
$b$ $[\frac{\mathrm{s}}{\mathrm{m}^2}]$
$c$ $[\frac{1}{\mathrm{m}}]$
$h$ [m]
$t$ [s]

and two (2) fundamental units:

time [s]
length [m]

Thus one will obtain $5-2=3$ dimensionless $\pi$ parameters that characterize the problem. The table of fundamental units reads as given in Table 3.4.

Table 3.4: The fundamental units of the system.

| - | $a$ | $b$ | $c$ | $h$ | $t$ |
|---|---|---|---|---|---|
| seconds | 2 | 1 | 0 | 0 | 1 |
| meters | -2 | -2 | -1 | 1 | 0 |

According to the Buckingham $\pi$ theorem the system of equations evolves as follows

$$\begin{pmatrix} 2 & 1 & 0 & 0 & 1 \\ -2 & -2 & -1 & 1 & 0 \end{pmatrix} \cdot \begin{pmatrix} \pi_{1,a} & \pi_{2,a} & \pi_{3,a} \\ \pi_{1,b} & \pi_{2,b} & \pi_{3,b} \\ \pi_{1,c} & \pi_{2,c} & \pi_{3,c} \\ \pi_{1,h} & \pi_{2,h} & \pi_{3,h} \\ \pi_{1,t} & \pi_{2,t} & \pi_{3,t} \end{pmatrix} = \begin{pmatrix} 0 & 0 & 0 \\ 0 & 0 & 0 \end{pmatrix}. \tag{3.28}$$

This system is under-determined, and one is allowed to choose three parameters in each $\pi$ vector.

Viscous effects and gravity as scaling forces (index †)

Here $a$ (inertia) shall be the basic parameter, while $b$ (viscosity) and $c$ (gravity) shall be the scaling parameters. One can set for an appropriate scaling for $h$ that $\pi_{1,a}=0$, $\pi_{1,h}=1$, and

$\pi_{1,t} = 0$. A parameter for $t$ can be found by setting $\pi_{2,a} = 0$, $\pi_{2,h} = 0$, and $\pi_{2,t} = 1$. To find the basic dimensionless parameter one may use $\pi_{3,a} = -1/2$ (this is chosen to be consistent with $\Omega$ as defined by Quéré et al. [79], other choices lead to linearly dependent solutions), $\pi_{3,h} = 0$, and $\pi_{3,t} = 0$. Now one can solve to obtain:

$$\begin{pmatrix} \pi_{1,a} & \pi_{2,a} & \pi_{3,a} \\ \pi_{1,b} & \pi_{2,b} & \pi_{3,b} \\ \pi_{1,c} & \pi_{2,c} & \pi_{3,c} \\ \pi_{1,h} & \pi_{2,h} & \pi_{3,h} \\ \pi_{1,t} & \pi_{2,t} & \pi_{3,t} \end{pmatrix} = \begin{pmatrix} 0 & 0 & -1/2 \\ 0 & -1 & 1 \\ 1 & 2 & -1 \\ 1 & 0 & 0 \\ 0 & 1 & 0 \end{pmatrix} \tag{3.29}$$

Thus the Buckingham $\pi$ theorem provides two dimensionless variables and one dimensionless basic parameter.

$$\pi_1^\dagger = a^0 b^0 c^1 h^1 t^0 \tag{3.30}$$

$$\pi_2^\dagger = a^0 b^{-1} c^2 h^0 t^1 \tag{3.31}$$

$$\pi_3^\dagger = a^{-\frac{1}{2}} b^1 c^{-1} h^0 t^0 \tag{3.32}$$

Inertia and gravity as scaling forces (index ‡)

Here $b$ (viscosity) shall be the basic parameter, while $a$ (inertia) and $c$ (gravity) shall be the scaling parameters. One can set for an appropriate scaling for $h$ that $\pi_{1,b} = 0$, $\pi_{1,h} = 1$, and $\pi_{1,t} = 0$. A parameter for $t$ can be found by setting $\pi_{2,b} = 0$, $\pi_{2,h} = 0$, and $\pi_{2,t} = 1$. To find the basic dimensionless parameter one may use $\pi_{3,b} = 1$, $\pi_{3,h} = 0$, and $\pi_{3,t} = 0$. Now one can solve to obtain:

$$\begin{pmatrix} \pi_{1,a} & \pi_{2,a} & \pi_{3,a} \\ \pi_{1,b} & \pi_{2,b} & \pi_{3,b} \\ \pi_{1,c} & \pi_{2,c} & \pi_{3,c} \\ \pi_{1,h} & \pi_{2,h} & \pi_{3,h} \\ \pi_{1,t} & \pi_{2,t} & \pi_{3,t} \end{pmatrix} = \begin{pmatrix} 0 & -1/2 & -1/2 \\ 0 & 0 & 1 \\ 1 & 1 & -1 \\ 1 & 0 & 0 \\ 0 & 1 & 0 \end{pmatrix} \tag{3.33}$$

Thus the Buckingham $\pi$ theorem provides two dimensionless variables and one dimensionless basic parameter.

$$\pi_1^\ddagger = a^0 b^0 c^1 h^1 t^0 \tag{3.34}$$

$$\pi_2^\ddagger = a^{-\frac{1}{2}} b^0 c^1 h^0 t^1 \tag{3.35}$$

$$\pi_3^\ddagger = a^{-\frac{1}{2}} b^1 c^{-1} h^0 t^0 \tag{3.36}$$

Inertia and viscous effects as scaling forces (index $*$)

Here $c$ (gravity) shall be the basic parameter, while $a$ (inertia) and $b$ (viscosity) shall be the

scaling parameters. One can set for an appropriate scaling for $h$ that $\pi_{1,c} = 0$, $\pi_{1,h} = 1$, and $\pi_{1,t} = 0$. A parameter for $t$ can be found by setting $\pi_{2,c} = 0$, $\pi_{2,h} = 0$, and $\pi_{2,t} = 1$. To find the basic dimensionless parameter one may use $\pi_{3,c} = -1$ (this is chosen to be consistent with $\Omega$ as defined by Quéré et al. [79], other choices lead to linearly dependent solutions), $\pi_{3,h} = 0$, and $\pi_{3,t} = 0$. Now one can solve to obtain:

$$\begin{pmatrix} \pi_{1,a} & \pi_{2,a} & \pi_{3,a} \\ \pi_{1,b} & \pi_{2,b} & \pi_{3,b} \\ \pi_{1,c} & \pi_{2,c} & \pi_{3,c} \\ \pi_{1,h} & \pi_{2,h} & \pi_{3,h} \\ \pi_{1,t} & \pi_{2,t} & \pi_{3,t} \end{pmatrix} = \begin{pmatrix} -1/2 & -1 & -1/2 \\ 1 & 1 & 1 \\ 0 & 0 & -1 \\ 1 & 0 & 0 \\ 0 & 1 & 0 \end{pmatrix} \tag{3.37}$$

Thus the Buckingham $\pi$ theorem provides two dimensionless variables and one dimensionless basic parameter.

$$\pi_1^* = a^{-\frac{1}{2}} b^1 c^0 h^1 t^0 \tag{3.38}$$

$$\pi_2^* = a^{-1} b^1 c^0 h^0 t^1 \tag{3.39}$$

$$\pi_3^* = a^{-\frac{1}{2}} b^1 c^{-1} h^0 t^0 \tag{3.40}$$

# Chapter 4

# The transition from inertial to viscous flow

## 4.1 Introduction

The following chapter is based on the publication "The transition from inertial to viscous flow in capillary rise" by N. Fries and M. Dreyer [36]. When dealing with the problem of capillary rise it is of great interest to know which forces (e.g. inertia, viscous forces, gravity) are dominant. This is based on the fact that one has to make certain assumptions to obtain analytical solutions for the momentum balance. These assumptions are mostly the neglect of certain forces (see subsections of 3.2). This, however, limits the validity of the derived equations to certain time intervals where these forces can actually be neglected [11, 61, 81, 104]. Stange et al. [95, 96] separate the individual time stages by means of dimensionless numbers. Ichikawa and Satoda [47] compare several previous works, present experimental results and conduct a dimensional analysis. Quéré et al. [78, 79] investigate the inertia dominated flow period. Subsequent time stages ($t \gg 0$) with influence of gravity are discussed in [35, 112].

In this chapter some light shall be shed on the different stages of capillary rise and the transitions between them. The focus is on cylindrical tubes although all calculations presented in the following are equally valid for porous media, as the pore structure parameters $K$, $R_s$ and $\phi$ can be included in the parameters $a$, $b$ and $c$ (see Eq. (3.4)). As previously introduced the simplified momentum balance of a liquid inside a capillary tube reads (see Eq. (2.48))

$$\frac{2\sigma\cos(\theta)}{R} = \frac{d\left(\rho h\dot{h}\right)}{dt} + \frac{8\mu h}{R^2}\dot{h} + \rho g h. \tag{4.1}$$

## 4.2 Analytical solutions for defined time domains

In the following several approaches to obtain analytical solutions of the momentum balance are discussed.

### 4.2.1 Purely inertial time domain

For the very first moments after the liquid contacts the tube Quéré [78] takes the following approach: Neglecting the viscous and the gravity term in Eq.(4.1) gives

$$\frac{2\sigma\cos(\theta)}{\rho R} = \frac{d\left(h\dot{h}\right)}{dt} = \dot{h}^2 + h\ddot{h}. \tag{4.2}$$

Quéré solves the differential equation (see section A.1) giving a capillary rise with constant velocity

$$h = t\sqrt{\frac{2\sigma\cos(\theta)}{\rho R}} = \frac{t}{\sqrt{a}}. \tag{4.3}$$

### 4.2.2 Visco-inertial time stage

Bosanquet [11] finds a solution featuring the inertial and viscous term resulting in the following differential equation

$$\frac{d}{dt}\left(h\dot{h}\right) + \frac{b}{a}h\dot{h} = \frac{1}{a}. \tag{4.4}$$

He obtains (see section A.2 for the derivation)

$$h^2 = \frac{2}{b}\left[t - \frac{a}{b}\left(1 - e^{\frac{-b}{a}t}\right)\right], \tag{4.5}$$

which is also used by Ichikawa and Satoda [47] in dimensionless form. Note: For $t \to \infty$ Eq. (4.5) converges into the Lucas-Washburn equation which will be presented next.

### 4.2.3 Purely viscous time stage

For the intermediate flow period Lucas [61] and Washburn [104] neglect the influence of inertia and the influence of gravity. They find (see Eq. 5.4 for the derivation)

$$h^2 = \frac{\sigma R\cos(\theta)}{2\mu}\,t = \frac{2}{b}\,t. \tag{4.6}$$

### 4.2.4 Viscous and gravitational time stage

During the later stages of capillary rise gravity can no longer be neglected. This time stage shall not be the focus of the current chapter, however it will be briefly discussed here for completeness. As will be derived in chapter 5, where this topic is explicated, one can generalize that for $h > 0.1\, h_{eq}$ gravity has to be considered. Here, $h_{eq}$ is the equilibrium height where the hydrostatic pressure balances the capillary pressure (see Eq. (4.9)). Analytic solutions (neglecting inertia) are given by Washburn [104] in implicit form (see section A.3 for the derivation)

$$t(h) = -\frac{hb}{c} - \frac{b}{c^2}\ln\left(1 - ch\right), \tag{4.7}$$

and by Fries and Dreyer [35] in explicit form (see Eq. (5.15) for the derivation)

$$h(t) = \frac{1}{c}\left[1 + W\left(-e^{-1-\frac{c^2 t}{b}}\right)\right]. \tag{4.8}$$

Here $W(x)$ is the Lambert W function. Finally one can calculate the equilibrium height (where capillary pressure equals hydrostatic pressure) to be [61]

$$h_{eq} = \frac{2\sigma\cos(\theta)}{\rho g R} = \frac{1}{c}. \tag{4.9}$$

## 4.3 Separation of time stages

One can derive three transition times (see Fig. 4.3):

- $t_1$ is the transition time between the purely inertial and the visco-inertial stage,
- $t_{2,S}$ is the time when the solution by Quéré and the Lucas-Washburn equation provide the same rise rate [96],
- $t_{2,Q}$ is the time when the solution by Quéré and the Lucas-Washburn equation provide the same height [78],
- $t_3$ is the transition time between visco-inertial and the purely viscous stage.

As stated, the purely inertial flow period shows a rise with constant velocity. Both solutions by Quéré Eq. (4.3) and Bosanquet Eq. (4.5) show this linear behavior in the beginning. At some point - in contrast to the solution by Quéré - Eq. (4.5) deviates to lower values as viscous effects become more important. One can find the point where viscous effects have to be taken

into account by the following approach: To obtain the time when both solutions reach a certain level of disagreement (e.g. 3% deviation) one may write

$$0.03 = \frac{h_{Quere}(t_1) - h_{Bosanquet}(t_1)}{h_{Quere}(t_1)}. \tag{4.10}$$

To solve this equation numerical methods have to be applied as no analytical form could be found. This is also the reason why the calculations are explicated here for a single level of deviation (3%) only. Numerical calculation yields

$$t_1 = \frac{0.0232 R^2 \rho}{\mu} = \frac{0.1856 a}{b}, \tag{4.11}$$

and using Eq. (4.5) provides

$$h_1 = 0.0318 \sqrt{\frac{R^3 \rho \sigma \cos(\theta)}{\mu^2}} = \frac{0.1800\sqrt{a}}{b}. \tag{4.12}$$

Stange et al. [96] find the time when the rise rates of the equation by Quéré and Lucas-Washburn are equal ($\dot{h}_{Quere} = \dot{h}_{Lucas-Washburn}$) to be

$$t_{2,S} = \frac{R^2 \rho}{16 \mu} = \frac{a}{2b}. \tag{4.13}$$

Quéré [78] calculates the time when the heights of his solution and the Lucas-Washburn equation intersect so that $h_{Quere} = h_{Lucas-Washburn}$ (as shown in Fig. 4.1). By equating the heights, he obtains

$$t_{2,Q} = \frac{R^2 \rho}{4 \mu} = \frac{2a}{b}, \tag{4.14}$$

and Eq. (4.3) or (4.6) give

$$h_{2,Q} = 0.3536 \sqrt{\frac{R^3 \rho \sigma \cos(\theta)}{\mu^2}} = \frac{2\sqrt{a}}{b}. \tag{4.15}$$

Quéré denotes this $t_{2,Q}$ as $t^*$. Here, however, $t_{2,Q}$ shall be used to prevent confusion with the dimensionless time introduced in the previous chapter. $t_{2,S}$ and $t_{2,Q}$ are feasible, "general" indicators for the transition from the inertial to the viscous time period. However, they do not provide information on when the influence of inertia is negligible and the Lucas-Washburn equation is sufficient to describe the capillary rise. To obtain such a measure one can take the equation given by Bosanquet [11] (visco-inertial stage) and the Lucas-Washburn solution (purely viscous). For $t \to \infty$ both solutions converge into each other. The time of 3% deviation in the predicted heights is defined by

$$0.03 = \frac{h_{LucasWashburn}(t_3) - h_{Bosanquet}(t_3)}{h_{LucasWashburn}(t_3)}. \tag{4.16}$$

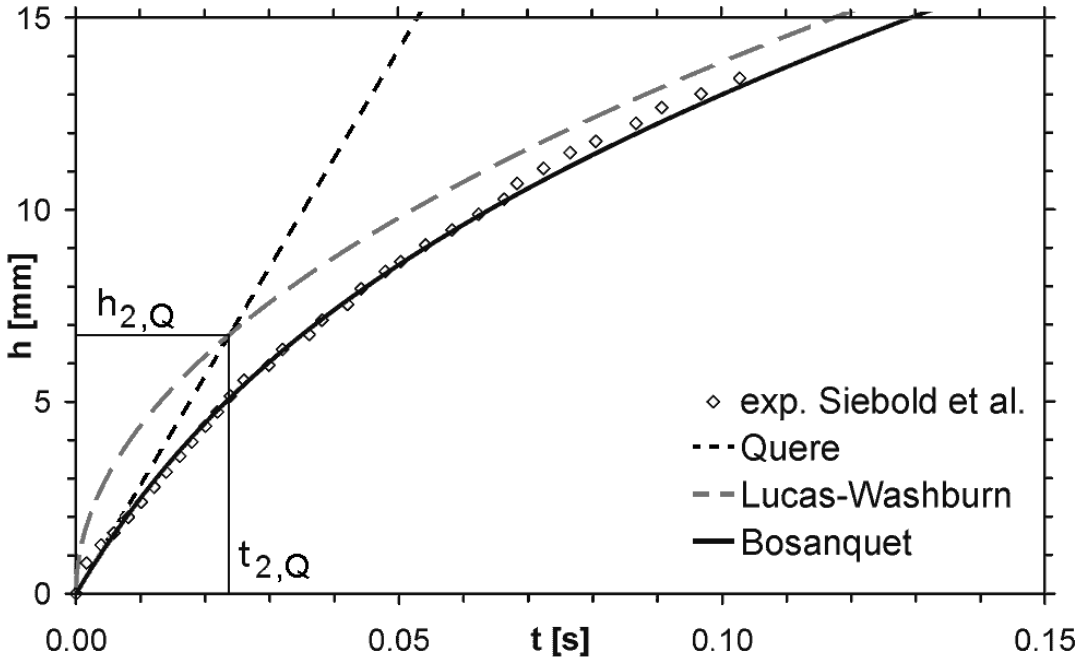


Figure 4.1: Comparison of analytic solutions with experimental results by Siebold et al. [89] using pentane in a glass tube with 191 $\mu$m radius. A constant contact angle of 73° (as found by Siebold et al.) has been used for the calculations. Note: This angle differs from the static contact angle.

In analogy to the derivation of $t_1$ only numerical methods were found to solve this equation, so one obtains

$$t_3 = \frac{2.1151 R^2 \rho}{\mu} = \frac{16.921 a}{b}. \tag{4.17}$$

Using Eq. (4.5) gives

$$h_3 = 0.9975 \sqrt{\frac{R^3 \rho \, \sigma \cos(\theta)}{\mu^2}} = \frac{5.6429 \sqrt{a}}{b}. \tag{4.18}$$

Fig. 4.2 displays the development of the pressures involved in the capillary rise process plotted over time. It can be observed that in the beginning the convective acceleration pressure ($\dot{h}^2$) dominates, while the local acceleration ($h\ddot{h}$) pressure is negative. However, the viscous pressure builds up fairly fast and overtakes the convective acceleration. For setups with gravity, which are not considered here, the hydrostatic pressure would rise and eventually dominate. Finally it would become equal to the capillary pressure.

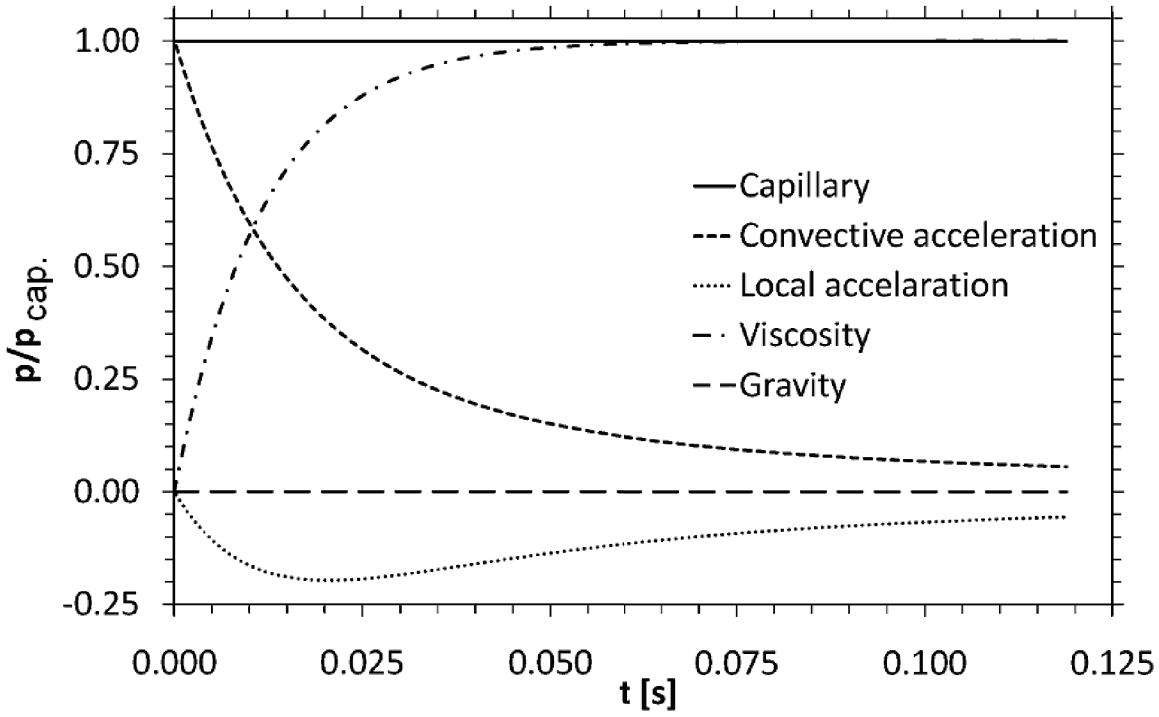


Figure 4.2: Plot of the pressures normalized by the capillary pressure versus time. The case displayed in Fig. 4.1 is considered. Note that the effect of gravity is neglected and thus is set to zero, as also done by all equations plotted in Fig. 4.1.

## 4.4 Discussion in dimensionless form

In the following the dimensionless scaling provided by Ichikawa and Satoda [47], as described in section 3.2.3 is used. In rearranged form it reads

$$t^* = \frac{8\mu}{\rho R^2} t = \frac{b}{a} t, \tag{4.19}$$

and

$$h^* = \sqrt{\frac{16\mu^2}{\rho R^3 \sigma \cos(\theta)}}\ h = \frac{b}{\sqrt{2a}}\, h. \tag{4.20}$$

For an expression of this terms in dimensionless numbers see Table 3.2. This scaling can be used to transform the analytical solutions into a dimensionless form. The solution by Quéré [78] Eq. (4.3) then reads

$$h^* = \frac{t^*}{\sqrt{2}}. \tag{4.21}$$

The equation by Bosanquet [11] Eq. (4.5) changes to

$$h^* = \sqrt{t^* - (1 - e^{-t^*})}, \tag{4.22}$$

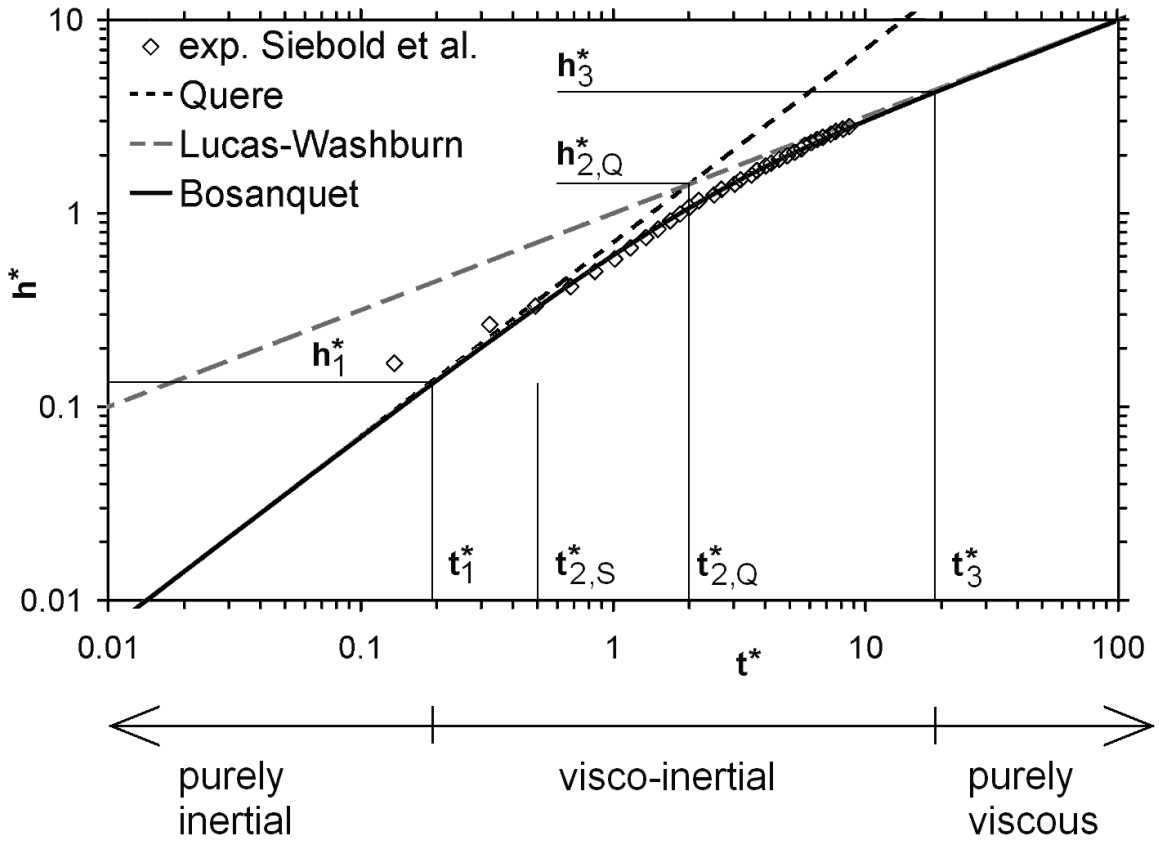


Figure 4.3: Dimensionless diagram showing an overview of the initial time stages of capillary rise. The same case as shown in Fig. 4.1 is considered.

and the Lucas-Washburn equation [61, 104] Eq. (4.6) reads

$$h^* = \sqrt{t^*}. \tag{4.23}$$

In Fig. 4.3, these equation are plotted in logarithmic scale. The points of transition between the time periods are shown. Using the presented scalings the points of transition, determined by Eqs. (4.11-4.18), can be given in dimensionless form, see Tables 4.1 and 4.2. The two tables each represent different levels of allowed deviation (1% and 3%). For 1% deviation the transition from purely inertial to visco-inertial flow (index 1) occurs earlier, while the transition from visco-inertial to purely viscous flow (index 3) occurs later when compared to the 3% deviation case. Thus, restricting the allowed deviation expands the time range where both forces have to be accounted for.

Table 4.1: Dimensionless values of the transition points. Note that for index 1 and 3 a deviation of 3% is assumed.

| $t_1^*$ | $h_1^*$ | $t_{2,S}^*$ | $t_{2,Q}^*$ | $h_{2,Q}^*$ | $t_3^*$ | $h_3^*$ |
|---|---|---|---|---|---|---|
| 0.1856 | 0.1273 | 0.5000 | 2.0000 | 1.4142 | 16.921 | 3.9901 |

Table 4.2: Dimensionless values of the transition points for 1% deviation (index 1 and 3).

| $t_1^*$ | $h_1^*$ | $t_{2,S}^*$ | $t_{2,Q}^*$ | $h_{2,Q}^*$ | $t_3^*$ | $h_3^*$ |
|---|---|---|---|---|---|---|
| 0.0606 | 0.0424 | 0.5000 | 2.0000 | 1.4142 | 50.251 | 7.0179 |

## 4.5 Conclusion

In this chapter the different time stages during the early stages of capillary rise have been dscussed. It is concluded that the purely inertial and the purely viscous flow period are separated by a visco-inertial stage where both effects have to be considered. By means of mathematical rearrangement the times and heights where the transition between the time periods occur have been derived. This provides a tool which allows to calculate which terms of the momentum balance have to be taken into account to obtain a solution of sufficient precision. Up to now, the time where the solution for the inertial and the viscous rise provide the same height has been used as a measure. However, it can now be stated that it takes about eight times as long for the flow to become independent of inertial effects ($8\,t_{2,Q}^* \approx t_3^*$ for 3% deviation).

# Chapter 5

# Analytical solutions including the gravity term

## 5.1 Introduction

The following chapter is based on the publication "An Analytic Solution of Capillary Rise Restrained by Gravity" by N. Fries and M. Dreyer [35]. Regarding the behavior of a liquid brought into contact with a vertical, small tube as shown in Fig. 1.1, it can be seen that at first a fairly fast flow into the structure develops. Later the rise of the liquid will continuously slow down until finally a static state is reached. The basis for the calculations presented in this chapter shall be the simplified momentum balance of liquid within a capillary tube as introduced previously in Eq. (2.48)

$$\underbrace{\frac{2\sigma\cos(\theta)}{R}}_{1} = \underbrace{\rho g h}_{2} + \underbrace{\frac{8\mu h}{R^2}\dot{h}}_{3} + \underbrace{\rho\frac{d(h\dot{h})}{dt}}_{4}. \tag{5.1}$$

In Eq. (5.1), the individual terms from left to right refer to:

1. The capillary pressure
2. The gravity term (hydrostatic pressure)
3. The viscous pressure loss (Hagen-Poiseuille)
4. The inertia terms (local and convective)

When porous media are investigated the Darcy law as introduced in section 2.5 can be used

$$\frac{2\sigma\cos(\theta)}{R_s} = \rho g h + \frac{\phi\mu h}{K}\dot{h} + \rho\frac{d(h\dot{h})}{dt}. \tag{5.2}$$

To experimentally obtain the two parameters $R_s$ and $K$ one can do a first evaluation of the equilibrium height in the static case to obtain the radius $R_s$ for the capillary pressure. Later the permeability $K$ can be obtained by fitting the calculated liquid rise curve to experimental values.

The differential equations (5.1) and (5.2) cannot be easily solved analytically, instead numerical methods may be used. However, as sometimes an analytical solution is favorable, solutions can be found for certain flow regimes where individual terms of Eqs. (5.1) and (5.2) can be neglected. Stange [95] claims that there are four time regimes. For small times the inertia term dominates, later the convective losses in the entry region (not modeled here), then the viscous term and finally the hydrostatic term. For infinite times a static state is reached where the hydrostatic pressure balances the capillary pressure. As applications of capillary flow or experiments are often bound to certain time regimes, it is feasible to neglect the corresponding terms in Eq. (5.1) to obtain analytical solutions. In the following two of these are presented.

## 5.2 Viscous dominated flow

Lucas [61] and Washburn [104] consider a flow regime where the influence of inertia as well as the influence of gravity can be neglected. Thus, Eq. (5.1) simplifies to

$$\frac{2\sigma\cos(\theta)}{R} = \frac{8\mu h\dot{h}}{R^2}. \tag{5.3}$$

Rearranging gives

$$h\frac{dh}{dt} = \frac{\sigma R\cos(\theta)}{4\mu}. \tag{5.4}$$

Solving this ordinary differential equation with the initial condition $h(0) = 0$ by means of separation of variables leads to the well-established Lucas-Washburn equation as previously introduced in section 4.2.3:

$$h^2 = \frac{\sigma R\cos(\theta)}{2\mu}t \mathrel{\widehat{=}} \frac{4\sigma\cos(\theta)}{\mu}\frac{K}{\phi R_s}t \mathrel{\widehat{=}} \frac{2}{b}t. \tag{5.5}$$

The Lucas-Washburn solution is probably the most used equation when it comes to the characterization of capillary transport or “wicking” in capillary tubes, porous media or the capillaries in packed powder. However, the fairly simple - and thus nice to handle - Eq. (5.5) has some limitations. For small times the fluid velocity is approaching infinity, which is not feasible. This discrepancy can be explained with the neglect of the inertia term. Also when flow is occurring in a vertical capillary under gravity there is no limit for the maximum reachable height which

originates from neglecting the gravity term. In the following sections the gravity term shall not be neglected which still allows to give an analytical solution in terms of $t(h)$ - as already shown by Washburn in 1921 - and in terms of $h(t)$ as will be presented later.

## 5.3 Viscous and hydrostatic dominated flow regime

To extend the Lucas-Washburn equation to flows where gravity and thus hydrostatic pressure has to be taken into account only the inertia term of Eqs. (5.1) or (5.2) is neglected giving for Eq. (5.2):

$$\frac{2\sigma\cos(\theta)}{R_s} = \rho g h + \frac{\phi}{K}\mu h\dot{h}. \tag{5.6}$$

Rearranging gives

$$\dot{h} = \frac{2\sigma\cos(\theta)}{\phi\mu}\frac{K}{R_s}\frac{1}{h} - \frac{\rho g}{\mu}\frac{K}{\phi}, \tag{5.7}$$

valid for $h \neq 0$ as there is a singularity. To simplify the equation one may introduce the previously introduced constants $a$, $b$ and $c$ (capillary tube and Darcy version) reducing Eq. (5.7) to

$$\dot{h} = \frac{1}{bh} - \frac{c}{b}. \tag{5.8}$$

As mentioned above, an analytical solution to this differential equation is given by Washburn [104] or Lukas and Soukupova [62]. It is calculated as following: Eq. (5.8) is rewritten to

$$dt = \frac{bh\,dh}{1-ch}. \tag{5.9}$$

After integration as shown in section A.3 one obtains

$$t = -\frac{bh}{c} - \frac{b}{c^2}\ln(1-ch) + C. \tag{5.10}$$

To find the unknown constant $C$ the initial condition

$$h(t \to 0) = 0 \tag{5.11}$$

can be used to give

$$C = 0. \tag{5.12}$$

This leads to the following implicit analytical form

$$t = -\frac{bh}{c} - \frac{b}{c^2}\ln(1-ch), \tag{5.13}$$

which is the result of Washburn [104] or Lukas and Soukupova [62] in terms of $t = t(h)$. Hamraoui and Nylander [41] find this solution to diverge as the liquid approaches the equilibrium

height. Zhmud et al. [112] evolve a long term asymptotic solution in terms of $h(t)$, as shown here in rearranged form

$$h(t) = \frac{1}{c}(1 - e^{-\frac{c^2 t}{b}}). \tag{5.14}$$

To obtain a more accurate solution for $h(t)$ a new approach is followed. Eq. (5.13) is multiplied by $-c^2/b$, and 1 is subtracted on both sides

$$-1 - \frac{c^2 t}{b} = ch - 1 + \ln(1 - ch), \tag{5.15}$$

which by taking it to the power of $e$ gives after rearrangement

$$-e^{-1-\frac{c^2 t}{b}} = (ch - 1)e^{ch-1}. \tag{5.16}$$

At this point, the Lambert W function $W(x)$ named after Johann Heinrich Lambert, and defined by an inverse exponential function

$$x = W(x)e^{W(x)} \tag{5.17}$$

can be used to solve for $h$. It can be seen that Eq. (5.16) follows the form

$$y(t) = x(h)e^{x(h)}. \tag{5.18}$$

By definition the W function can be written as

$$y(t) = W(y(t))e^{W(y(t))}. \tag{5.19}$$

Relating Eq. (5.18) and Eq. (5.19) gives

$$x(h)e^{x(h)} = W(y(t))e^{W(y(t))}. \tag{5.20}$$

From this it can be seen that

$$x(h) = W(y(t)). \tag{5.21}$$

Coming back to Eq. (5.16) the inverse properties of the Lambert W function can be used to give

$$ch - 1 = W\left(-e^{-1-\frac{c^2 t}{b}}\right). \tag{5.22}$$

After rearranging, one obtains

$$h(t) = \frac{1}{c}\left[1 + W\left(-e^{-1-\frac{c^2 t}{b}}\right)\right], \tag{5.23}$$

which is a full analytical solution in terms of $h = h(t)$, and can be verified as shown in section A.4. In the following it is referred to this solution as the "extended solution". In Fig. 5.1

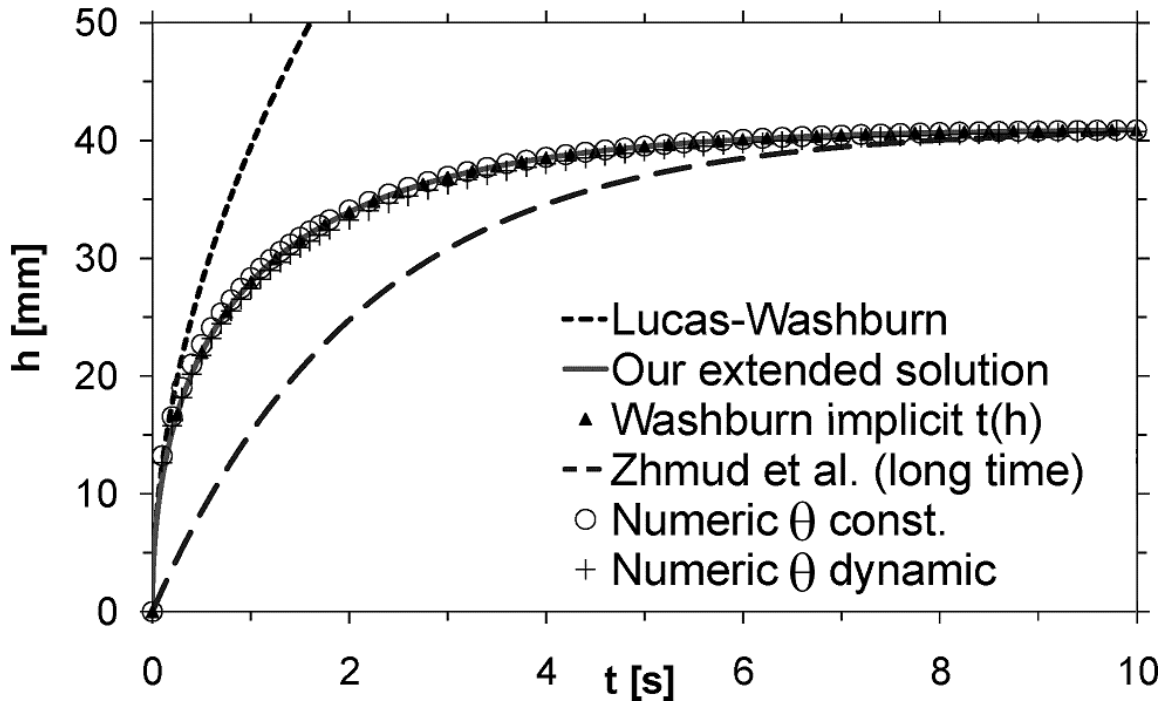


Figure 5.1: Different analytical and numerical solutions for silicone fluid (SF 0.65) in a 0.1 mm radius borosilicate glass capillary. Height $h$ is plotted versus time $t$. Extended solution denotes Eq. (5.23).

this extended solution is calculated and plotted for a setup using silicone fluid (SF 0.65) in a 0.1 mm radius borosilicate glass capillary. The liquid properties given in table 7.2 are used, and a contact angle of $\theta_s = 16.3°$ as found by Stange [95] is applied. The other lines in Fig. 5.1 refer to the Lucas-Washburn equation in Eq. (5.5) and the long time asymptotic solution by Zhmud et al. [112] in Eq. (5.14). The two numerical simulations are calculated with constant contact angle and dynamic contact angle as done by Chebbi [19], respectively. For the numerical simulations inertia is neglected and for the dynamic contact angle the equation given by Jiang et al. [48] (see section 2.4.4.1) is used. Fig. 5.2 displays a plot of the effective pressures for the same case as discussed above. Note that the convective and local acceleration terms (inertia) are shown, although these terms are neglected in the extended solution Eq. (5.23). It can be observed from Fig. 5.2 that the inertial terms - for the time stage considered - are small compared to the other terms and disappear for longer times. In the beginning the capillary pressure is mainly balanced by viscous friction, while with increasing height the hydrostatic pressure becomes dominant.

Further information on the Lambert W function as defined in Eq. (5.17) and its application is given in [22], [43] and [101]. Its solutions are partly in the complex plane, but switch to real

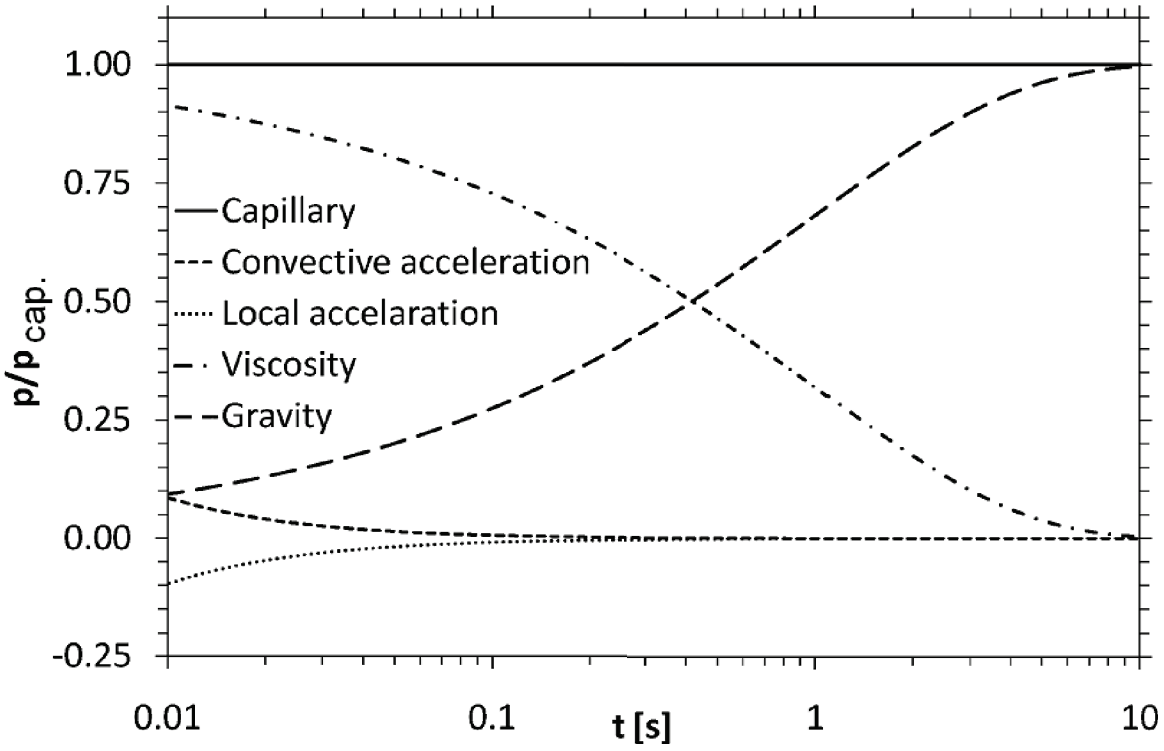


Figure 5.2: Plot of the pressures normalized by the capillary pressure versus time. The case displayed in Fig. 5.1 is considered.

values for $-1/e \leq x$ as shown in Fig. 5.3. Also, the Lambert W function has been used to solve differential equations before. For example Barry et al. [5] use the Lambert W function to give an analytical solution to a transcendental equation related to this present work. To calculate water movement in unsaturated soil they use the following differential equation

$$\alpha^* A \frac{dA}{dt} = 1 - A. \tag{5.24}$$

Here $\alpha^*$ denotes a constant with dimension [s] and $A$ a dimensionless "function of time $t$" [5]. Solving for the initial condition $A(t \to 0) = 0$ gives an equation featuring the Lambert W function

$$A(t) = 1 + W\left(-e^{\left(\frac{-t}{\alpha^*}-1\right)}\right). \tag{5.25}$$

Barry et al. [5] mention that it can be used to calculate infiltration as well as capillary rise of moisture in soils. The solution is - besides the different notations used in soil science - identical to the dimensionless version of the extended solution as given in Eq. (5.40). This is feasible as both models describe the same physical processes, one describing the motion of moisture in soils, the other describing the capillary rise in porous media and capillary tubes.

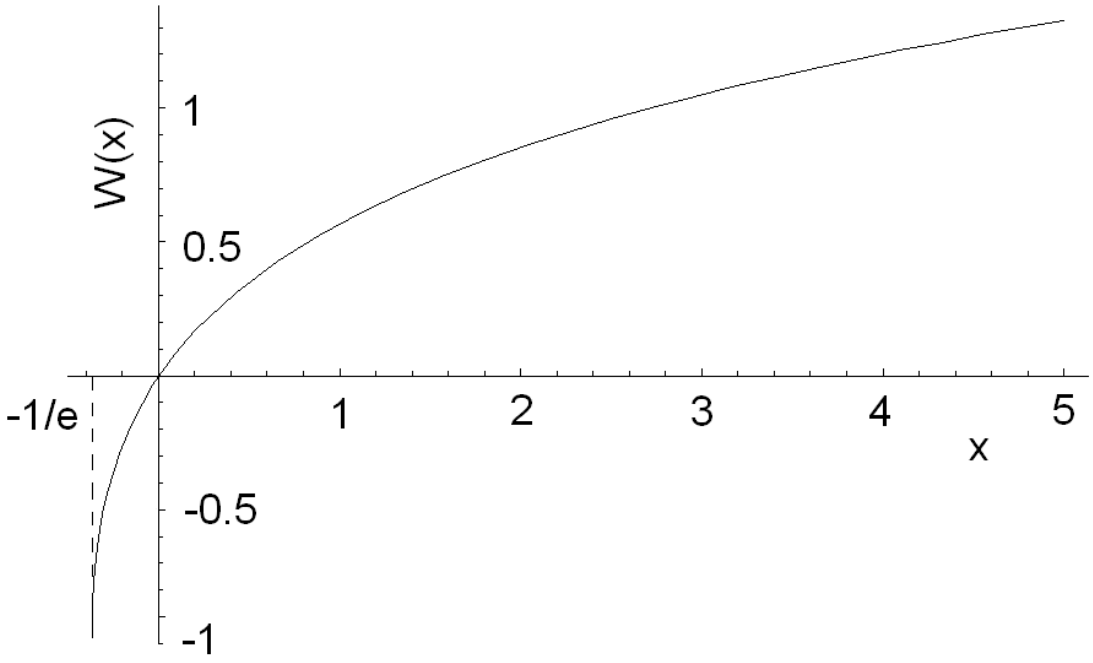


Figure 5.3: Characteristics of the upper branch of the Lambert W function for $-1/e \leq x \leq 5$.

### 5.3.1 Practical evaluation of the Lambert W function

When applying Eq. (5.23) to practical problems it is important to be able to calculate the numerical value of the Lambert W function. In many commercial mathematical programs the Lambert W function is already included to be found as W[x] or ProductLog[x]. It is also possible to use spreadsheet calculation programs that don't feature Lambert W. In this case it is required to write a macro using the "goal seek feature" or use other iterative solvers. Otherwise an approximation expression for $W(x)$ that covers the relevant range can be applied. For this work such an approximate function is given by Barry et al. [5] (slightly rearranged) as

$$W(x) \approx -1 + \frac{\sqrt{2+2ex}}{1+\frac{4.13501\sqrt{2+2ex}}{12.7036+\sqrt{2+2ex}}}. \tag{5.26}$$

For the upper branch this equation accounts for the relevant range of $-e^{-1} \leq x \leq 0$ with a maximum relative error of 0.1%. Further details on both branches of the Lambert W function are provided in section 8.1, Fig. 8.2 or [22].

### 5.3.2 Time to reach the equilibrium height

Regarding Eq. (5.23) one may notice that for infinite time the height $h$ converges into a maximum value $h_{eq}$. This is the point where the hydrostatic pressure equals the capillary

pressure, or mathematically $W(0) = 0$. This gives

$$h_{eq} = h(t \to \infty) = \frac{1}{c} = \frac{2\sigma\cos(\theta)}{R\rho g}. \tag{5.27}$$

As $h$ approaches $h_{eq}$ at some point the height increase is so small that one may speak of a static state. To find the time needed to reach this point, a static state time $t_s$ is here defined where $h$ reaches $(1-\epsilon)$ times $h_{eq}$. E.g. if $\epsilon = 0.01$, $h$ would have to reach 99% of $h_{eq}$. One may write

$$h(t_s) = (1-\epsilon)\, h_{eq}. \tag{5.28}$$

Using Eq. (5.27) and Eq. (5.23) gives

$$(1-\epsilon)\,\frac{1}{c} = \frac{1}{c}\left[1 + W\left(-e^{-1-\frac{c^2 t_s}{b}}\right)\right]. \tag{5.29}$$

After rearranging one obtains

$$-\epsilon = W\left(-e^{-1-\frac{c^2 t_s}{b}}\right), \tag{5.30}$$

and with Eq. (5.17)

$$-\epsilon e^{-\epsilon} = -e^{-1-\frac{c^2 t_s}{b}}. \tag{5.31}$$

To obtain $t_s$

$$-1 - \frac{c^2 t_s}{b} = \ln(\epsilon) - \epsilon, \tag{5.32}$$

and finally

$$t_s = \frac{b}{c^2}\left[-\ln(\epsilon) + \epsilon - 1\right]. \tag{5.33}$$

This may also be written with all variables to give (for $\epsilon = 0.01$, corresponding to $h = 99\%$ of $h_{eq}$)

$$t_s \approx \frac{3.62\, b}{c^2} \mathrel{\widehat{=}} 3.62\frac{16\,\sigma\mu\cos(\theta)}{\rho^2 g^2}\frac{1}{R^3} \mathrel{\widehat{=}} 3.62\frac{2\,\sigma\mu\cos(\theta)}{\rho^2 g^2}\frac{\phi}{R_s K}. \tag{5.34}$$

### 5.3.3 Flow velocity

To obtain the flow velocity $\dot{h}(t)$ it is necessary to differentiate the height $h(t)$. For the Lucas-Washburn equation one obtains

$$\dot{h}(t) = \sqrt{\frac{1}{2b\,t}}, \tag{5.35}$$

while using the extended solution including gravity yields

$$\dot{h}(t) = -\frac{c}{b}\,\frac{W\left(-e^{-1-\frac{c^2 t}{b}}\right)}{1 + W\left(-e^{-1-\frac{c^2 t}{b}}\right)}. \tag{5.36}$$

Both velocity functions are only defined for $t > 0$. Further details on differentiating the Lambert W function can be found in section A.4.

### 5.3.4 Dimensional analysis

To generalize the obtained solutions, the introduction of dimensionless numbers is always of interest. The following calculations use the dimensionless scaling introduced in chapter 3. Viscous effects and gravity are applied as scaling forces to obtain $h^\dagger$ and $t^\dagger$ as shown in section 3.2.1. Thus,

$$h^\dagger = ch = \frac{h}{h_{eq}} = \frac{\rho g R}{2\sigma\cos(\theta)}h \mathrel{\widehat{=}} \frac{\rho g R_s}{2\sigma\cos(\theta)}h, \tag{5.37}$$

and

$$t^\dagger = \frac{c^2 t}{b} = \frac{3.62t}{t_s} = \frac{\rho^2 g^2 R^3}{16\mu\sigma\cos(\theta)}t \mathrel{\widehat{=}} \frac{\rho^2 g^2}{2\,\mu\sigma\cos(\theta)}\frac{R_s K}{\phi}t. \tag{5.38}$$

$h^\dagger$ can be regarded as the height normalized by the equilibrium height. $t^\dagger$ normalizes the time with the time to reach the static state and a factor of 3.62 (calculated using $\epsilon = 0.01$). Thus, from Eq. (5.34) it can be derived that if $t^\dagger$ is larger than 3.62 a static state is reached as shown in Fig. 5.4.

Using these dimensionless numbers the Lucas-Washburn equation in Eq. (5.5) as well as the extended solution in Eq. (5.23) can be made dimensionless providing

$$h^\dagger = \sqrt{2\,t^\dagger}, \tag{5.39}$$

for the Lucas-Washburn equation and

$$h^\dagger = 1 + W\left(-e^{-1-t^\dagger}\right) \tag{5.40}$$

for the extended solution including the gravity term. Fig. 5.4 shows that in the beginning the Lucas-Washburn solution fits good to the extended solution in Eq. (5.23), however tends to deviate to higher values for longer times since gravity is neglected. In anticipation of later results Fig. 5.6 displays a close up of the relevant region. For $t^\dagger > 3.62$ the extended solution reaches a static state. Regarding the velocity of the extended solution in Eq. (5.36) one may derive a dimensionless number for the flow velocity, the "capillary velocity number" $v^\dagger$

$$v^\dagger = \frac{b\,\dot{h}}{c} = \frac{8\dot{h}\mu}{\rho g R^2} \mathrel{\widehat{=}} \frac{\phi\dot{h}\mu}{\rho g K}. \tag{5.41}$$

$v^\dagger$ can be interpreted as viscous forces in relation to gravity forces

$$v^\dagger = \frac{\mathrm{Ca}}{\mathrm{Bo}}. \tag{5.42}$$

Using $t^\dagger$ and $v^\dagger$ the flow velocity can be rewritten as

$$v^\dagger = \sqrt{\frac{1}{2t^\dagger}} \tag{5.43}$$

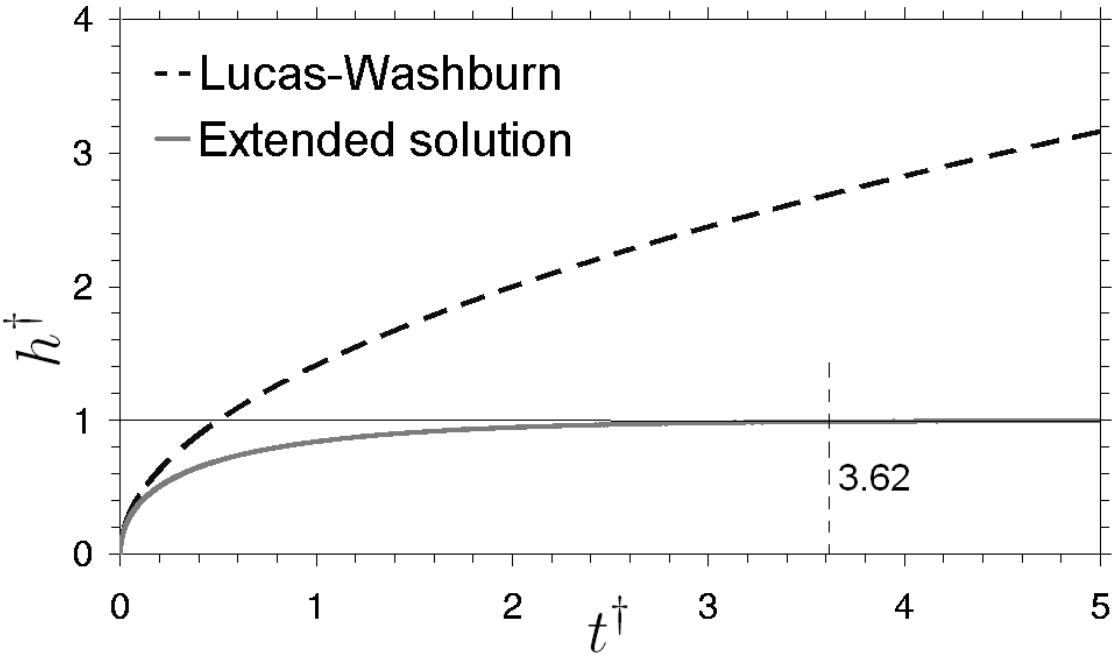


Figure 5.4: Dimensionless representation of the Lucas-Washburn equation and the extended solution Eq. (5.23). The static state is reached for $t^\dagger \geq 3.62$.

for the Lucas-Washburn equation and

$$v^\dagger = \frac{-W\left(-e^{-1-t^\dagger}\right)}{1+W\left(-e^{-1-t^\dagger}\right)} \tag{5.44}$$

for the extended solution including the gravity term. These results are plotted in Fig. 5.5.

## 5.4 Validity of the Lucas-Washburn equation

When comparing the Lucas-Washburn equation Eq. (5.5) and the extended solution Eq. (5.23) one may notice that the Lucas-Washburn equation is preferable due to its simplicity, however, it is not valid for increasing time. The following chapter discusses a method for deciding to which time $t_w$ the Lucas-Washburn equation may be used when taking into account an acceptable error. For times $t > t_w$ the extended solution including gravity has to be considered. This chapter intends to give more insight to this question. If the acceptable discrepancy is - for example - 1% one may write:

$$(100\% - 1\%)\, h_{Lucas\ Washburn} = h_{extended\ solution} \tag{5.45}$$

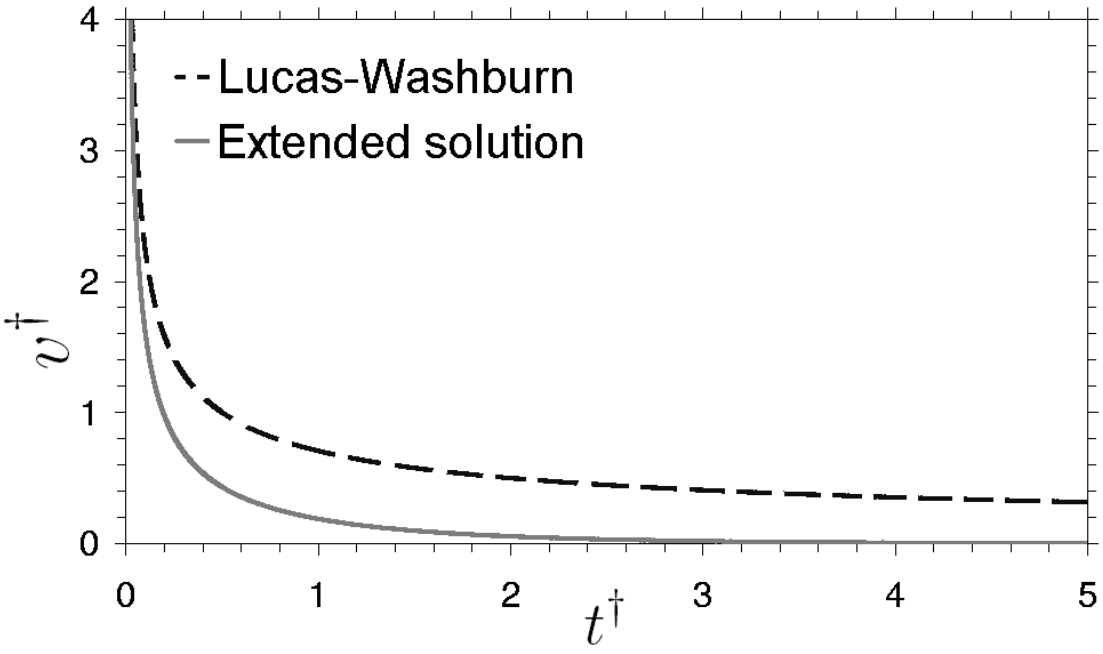


Figure 5.5: Dimensionless representation of the flow velocity calculated by differentiating the Lucas-Washburn equation and the extended solution Eq. (5.23).

equal to

$$(1-0.01)\sqrt{\frac{2}{b}t_w} = \frac{1}{c}\left[1+W\left(-e^{-1-\frac{c^2 t_w}{b}}\right)\right], \tag{5.46}$$

with

$$\sqrt{\frac{2}{b}t} = \sqrt{\frac{\sigma R\cos(\theta)}{2\mu}t} \tag{5.47}$$

representing the Lucas-Washburn equation Eq. (5.5). To solve the transcendental equation Eq. (5.46) for $t_w$ the following approach is used. Considering the dimensionless number $t^\dagger$ one may assume that the solution $t_w$ of Eq. (5.46) can be expressed by means of this number

$$t_w = t_w^\dagger \frac{b}{c^2}, \tag{5.48}$$

with $t_w^\dagger$ being the unknown value. Substituting $t_w$ in Eq. (5.46) gives

$$0.99\sqrt{2t_w^\dagger} = 1+W\left(-e^{-1-t_w^\dagger}\right). \tag{5.49}$$

This transcendental equation can now be solved by means of numerical methods giving $t_w^\dagger = 0.0004523$. Thus the Lucas-Washburn equation can be used up to $t = 0.0004523\, a/b^2$ if an error of 1% is accepted. At this point, the height reached may again be expressed in terms of $h^\dagger$

$$h_w^\dagger = \frac{h_w}{h_{eq}} = 1+W\left(-e^{-1-t_w^\dagger}\right), \tag{5.50}$$

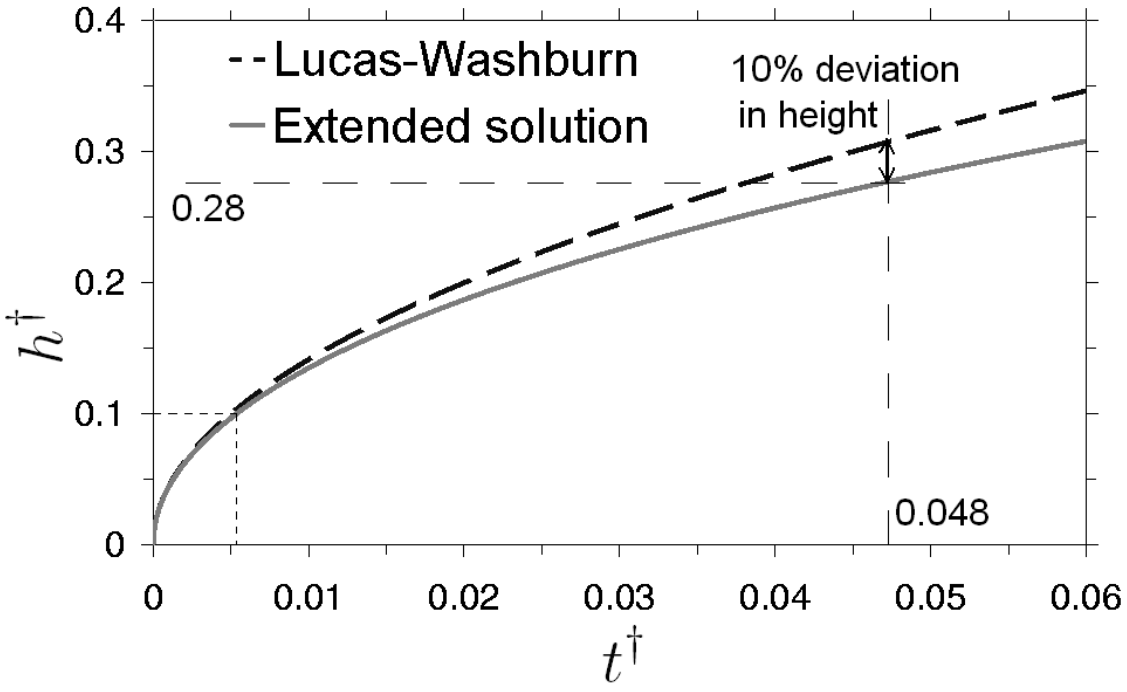


Figure 5.6: Dimensionless representation of the Lucas-Washburn equation and the extended solution Eq. (5.23). The mark represents 10% deviation.

giving $h_w^\dagger = h_w/h_{eq} = 0.029775$ for an error of 1%. Values for further errors are given in Table 5.1. Generalizing, it can be concluded that under gravity the Lucas-Washburn equation can be used up to about 10% of the equilibrium height. At this height an error of 3.54% is made. In anticipation of later results the criterion is applied to experimental data in Fig. 7.7.

Table 5.1: Further values for different errors.

| error | $t_w^\dagger = t_w\, c^2/b$ | $h_w^\dagger = h_w/h_{eq}$ |
|---|---|---|
| 1% | 0.0004523 | 0.029775 |
| 3.54% | 0.0053605 | 0.1 |
| 5% | 0.0115465 | 0.144366 |
| 10% | 0.0475088 | 0.277424 |

## 5.5 Experimental evidence

To verify the obtained results the investigation done by Stange [95] can be used as a benchmark. He examines the fluid rise in capillary tubes made of borosilicate glass with different radii.

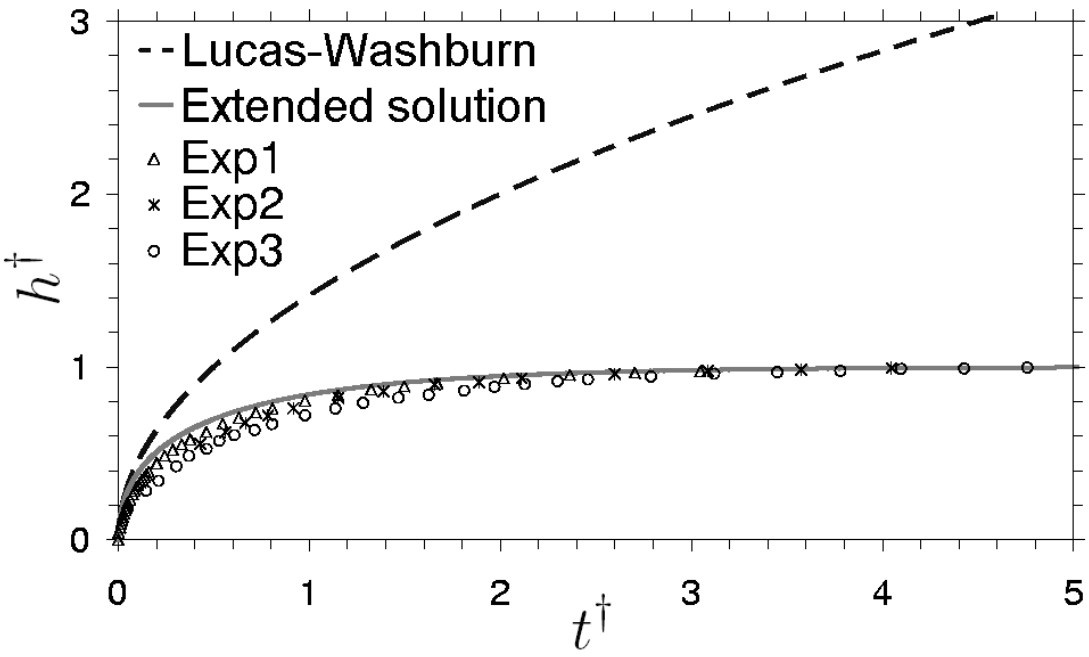


Figure 5.7: Dimensionless experimental results ($\psi \neq 0$) by Stange [95] as described in Table 5.2. Extended solution denotes Eq. (5.23).

Also the angle of inclination $\psi$, as introduced in section 2.4.5, is varied. Two different liquids, silicone fluid (SF 1.0) and Fluorinert engineering fluid (FC 77) are used. The liquid properties given by Stange [95] for the corresponding experiment temperatures are applied. The height recordings are performed by optical means and are plotted in dimensionless form in Fig. 5.7. The previously introduced dimensionless capillary height number $h^\dagger$ and the capillary time number $t^\dagger$ are used.

Table 5.2: Experimental data by Stange.

| Name | Inner radius | Fluid | Inclin. $\psi$ | $\theta$ |
|---|---|---|---|---|
| Exp1 | 0.088 mm | SF1 | 32.3° | 16.3° |
| Exp2 | 0.104 mm | FC77 | 32.3° | 28.0° |
| Exp3 | 0.1405 mm | SF1 | 88.7° | 16.3° |

From the dimensionless plot it can be seen that the experimental data by Stange matches the values predicted by the extended solution Eq. (5.23). Especially for the static state values a good consistency can be observed. For $t^\dagger$ between 0.2 and 1.4 some deviation to lower results

can be seen. This may be explained by the assumptions taken, e.g. the neglect of entry effects or assuming a constant contact angle.

## 5.6 Evaluation for a general initial condition

In this section, the phenomenon of a falling capillary meniscus is investigated. This occurs if the initial position of the meniscus is above the equilibrium height. The equilibrium height is defined as the level where all forces are balanced and thus no movement of the meniscus occurs, e.g. the capillary pressure is equal to the hydrostatic pressure. A scenario for capillary fall in a tube could be a sudden increase of acceleration: If a capillary tube is filled with liquid in weightlessness (e.g. onboard a spacecraft) a hydrostatic pressure will build if the spacecrafts thrusters fire during a maneuver and the setup is exposed to acceleration. Depending on the tube diameter and the acceleration, the resulting equilibrium height may be "below" the actual meniscus position and a downward motion will evolve. The following brief literature review shall give an overview of some of the research done on capillary fall and drainage: In 1955 Batel [6] investigates the humidity remaining after drying in a centrifuge, but also gives an equation describing the dynamics of liquid drainage. Nenniger and Storrow [33] present an analytical model and a comparison with experimental results of the drainage of packed beds. Mason and Mellor [69] use simulations to investigate drainage and imbibition in a random packing of spheres. Schaefer et al. [84] experimentally determine the drainage of sand columns, further work by other authors is given in [10, 34, 63]. In 2002 Lorenceau et al. [60] focus on vertical pipes and gravitational oscillations. It is concluded that the viscosity of the fluid is of major importance and several mathematical models are presented. The problem of capillary fall has also been addressed by Schäffer and Wong [85], however mainly to investigate the stick-slip behavior on rough surfaces. In 1998, they investigate the dynamics of contact line pinning in capillary rise and fall. In glass capillaries with a rough surface they find stick-slip behavior, however for smooth surfaces no pinning is observed. In 2000, Schäffer and Wong [86] give further results on this topic and discuss differences between theory and experimental observations. They conclude that the dynamics of capillary fall and capillary rise differ due to the invisible liquid film coating the surface during capillary fall [109]. In a recent paper Fries and Dreyer [35] use the 1D momentum balance of a liquid in a porous medium to derive an analytical solution to the problem of capillary rise affected by gravity. In this section the application of the solution to a broader set of capillary flows such as rise, fall and drainage is discussed.

The basis for the calculations presented in the following is Eq. (5.8)

$$\dot{h} = \frac{1}{bh} - \frac{c}{b}. \tag{5.51}$$

Here it is important to mention again that the assumptions described in section 2.4.6 are taken. Also, in this chapter on the gravitational regime, all inertial forces (local and convective) are neglected. For certain cases it might be of interest to consider a more general definition of the previously used initial condition ($h(t \to 0) = 0$) like (see Fig. 5.8)

$$h(t_0) = h_0. \tag{5.52}$$

This leads to

$$h(t) = \frac{1}{c}\left\{1 + W\left[(-1 + ch_0)e^{-1+c(-\frac{c}{b}(t-t_0)+h_0)}\right]\right\}, \tag{5.53}$$

as is shown in section A.5. Regarding Eq. (5.53) it can be seen that for $t_0 = 0$ and $h_0 = 0$ the expression is equal to Eq. (5.23), the extended solution derived before. Varying $t_0$ will simply shift the begin of the motion on the time axis. It is more interesting to determine the effect of varying initial height $h_0$, and therefore to find a dimensionless parameter reflecting this variable. Concerning the parameter $h_0$ one may define

$$\delta = c\, h_0 = \frac{h_0}{h_{eq}}. \tag{5.54}$$

Thus, as $h_0$ refers to the initial height, the following interpretation can be given: as $1/c$ is the equilibrium height, $\delta$ is the initial height normalized by the equilibrium height. When $\delta$ is equal to zero the initial height is zero and "normal" capillary rise occurs. If $\delta$ is 0.5 the initial height is already 50% of the equilibrium height and the liquid only has to rise by another half to reach equilibrium state. When $\delta = 1$ the liquid is already at equilibrium and no further movement will occur. Finally, when the initial liquid height is above the equilibrium height ($\delta > 1$) the fluid will move downwards and approach the equilibrium height from above.
With the parameters introduced above, Eq. (5.53) can be rewritten as

$$h^\dagger = 1 + W\left[(\delta - 1)e^{\delta - 1 - t^\dagger}\right]. \tag{5.55}$$

Again, viscous effects and gravity are applied as scaling forces to obtain $h^\dagger$ and $t^\dagger$ as shown in section 3.2.1. The implicit $t(h)$ solution of Eq. (5.53) has been used in dimensional form by Washburn [104] and Batel [6]. Wong and Schäffer [109] also evaluate the experimental results in smooth capillary tubes with this equation. Printing Eq. (5.55) with varying normalized initial heights $\delta$ yields Fig. 5.9. The lower part of the diagram ($\delta < 1$) refers to capillary rise, while

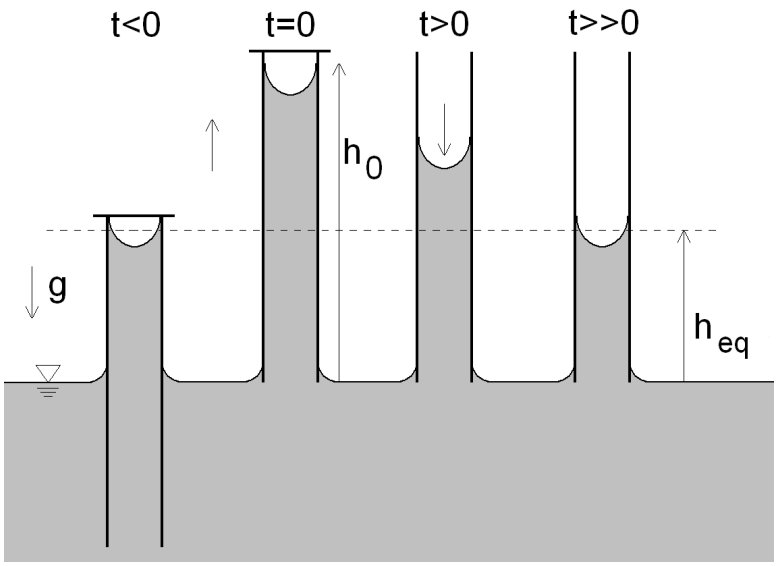


Figure 5.8: Schematic drawing of an experiment with initial position above the equilibrium height. At $t = 0$ the upper seal is opened. $h_0$ denotes the initial height while $h_{eq}$ is the equilibrium height.

the upper part refers to capillary fall. It is notable that the upper part is not just a simple reflection of the lower one. This is physically accounted for in a longer liquid column for the upper case than for the lower one. This results in higher viscous effects and thus the meniscus will take longer time to reach the equilibrium height.
For completeness it shall be mentioned that for the rising and falling case different inflow and outflow conditions may occur at the tube end. Besides the fact that inertia (local and convective) are not considered in the presented model, for the descending case the $\dot{h}^2$ term in the momentum balance Eq. (2.44) may be neglected as discussed in section 2.4.4.2.

### 5.6.1 Time to reach the equilibrium height

As the meniscus approaches the equilibrium height, its velocity decreases. Finally the movement is so slow, that one may consider this a static state. In this chapter the time necessary for the liquid to reach 99% (capillary rise), or 101% (fall) of the equilibrium height is determined. Setting $h^\dagger$ in Eq. (5.55) to 0.99 or 1.01 gives

$$t_s^\dagger = \delta - 1 - \ln \frac{-0.0099005}{\delta - 1}, \tag{5.56}$$

for $0 \leq \delta \leq 0.99$ (capillary rise), and

$$t_s^\dagger = \delta - 1 - \ln \frac{0.0101}{\delta - 1} \tag{5.57}$$

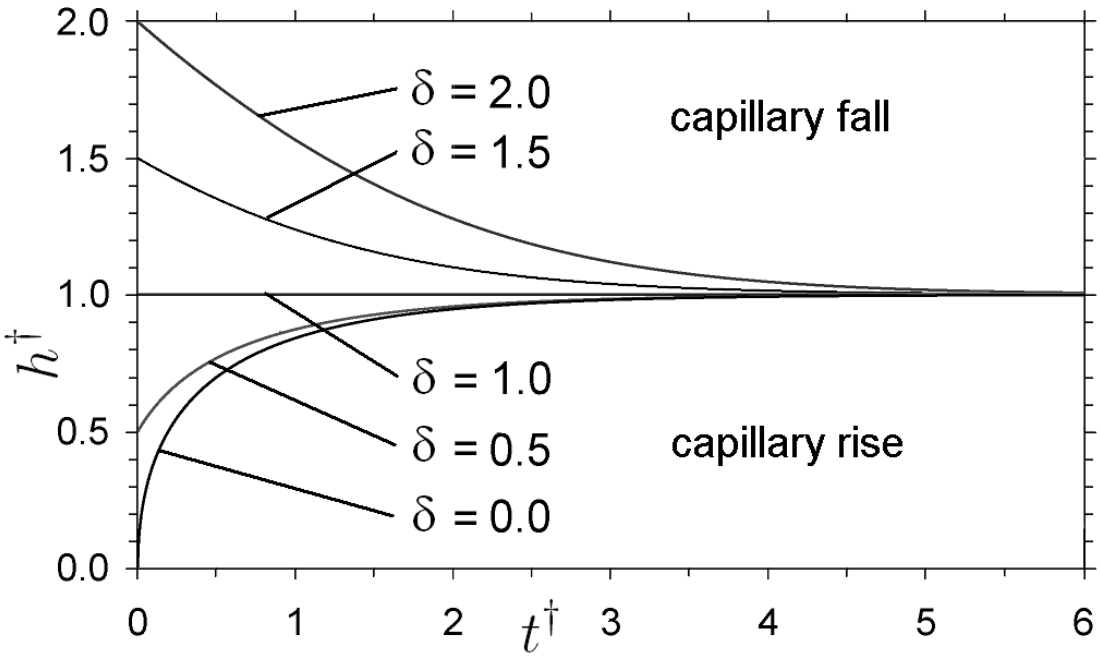


Figure 5.9: Dimensionless analytical solution plotted for different dimensionless initial heights $\delta$. The lower part of the diagram refers to capillary rise while the upper one describes capillary fall.

for $1.01 \leq \delta$ (capillary fall), respectively. These solutions are plotted in Fig 5.10. Again, due to the reasons given at the end of the previous section there is no symmetry axis at $\delta = 1$.

### 5.6.2 Comparison with experimental results from literature

In this section the analytical solution Eq. (5.55) is compared to experimental results taken from literature [85]. Fig. 5.11 shows the dynamic behavior of water in a 250 $\mu m$ diameter smooth surface glass tube. The dots refer to values obtained by Schäffer and Wong from image recordings, while the lines depict the calculated movement with the presented analytical solution. Two different cases are plotted, one featuring an initial position below the equilibrium height (capillary rise) and one starting above the equilibrium height (capillary fall). As can be seen from Fig. 5.11, the calculated lines match the experimental results fairly well. Especially for capillary fall, good consistency is observed, while there are some deviations for capillary rise. These deviations may be explained by the assumption made, especially choosing a constant contact angle of $\theta = 0$. The receding contact angle for the capillary fall may match this assumption well, however the dynamic advancing contact angle for the capillary rise may differ.

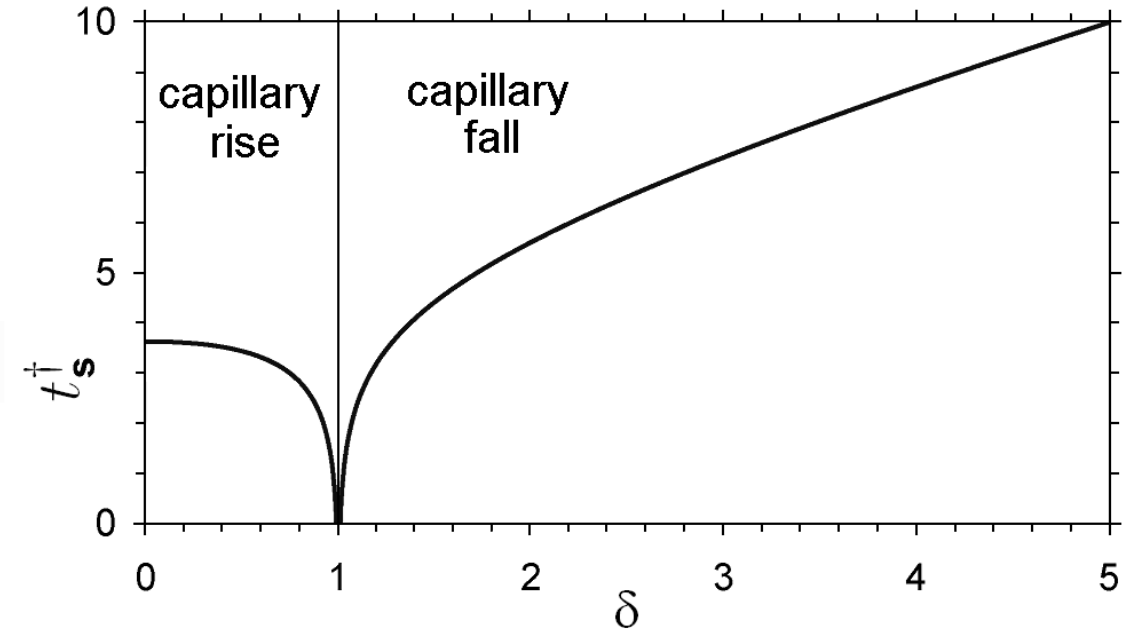


Figure 5.10: Dimensionless time $t_s^\dagger$ to reach static state as a function of dimensionless initial height $\delta$.

Wong and Schäffer [109] also discuss the deviations. They find that an invisible liquid film coating the surface during capillary fall can explain the difference between the rise and fall process. Good agreement is eventually reached in the comparison for the final equilibrium height for both cases.

## 5.7 Conclusion

A method for deriving an analytical solution to the momentum balance of a liquid in a capillary tube or porous medium is presented. The well-established Lucas-Washburn equation is shown as well as an extended solution introduced which is obtained by mathematical rearrangement of the implicit Washburn solution. The extended solution includes the gravity term (hydrostatic pressure) and enables the calculation of the liquid rise behavior for longer times. The time necessary to reach a static state is examined and several relevant dimensionless numbers are found. By means of these numbers, a dimensionless plot of the Lucas-Washburn equation and the extended solution including gravity is plotted. The flow velocity is obtained by differentiating the height and a dimensionless number for its description is found. Also the error made when neglecting gravity and using the Lucas-Washburn equation is determined. Furthermore,

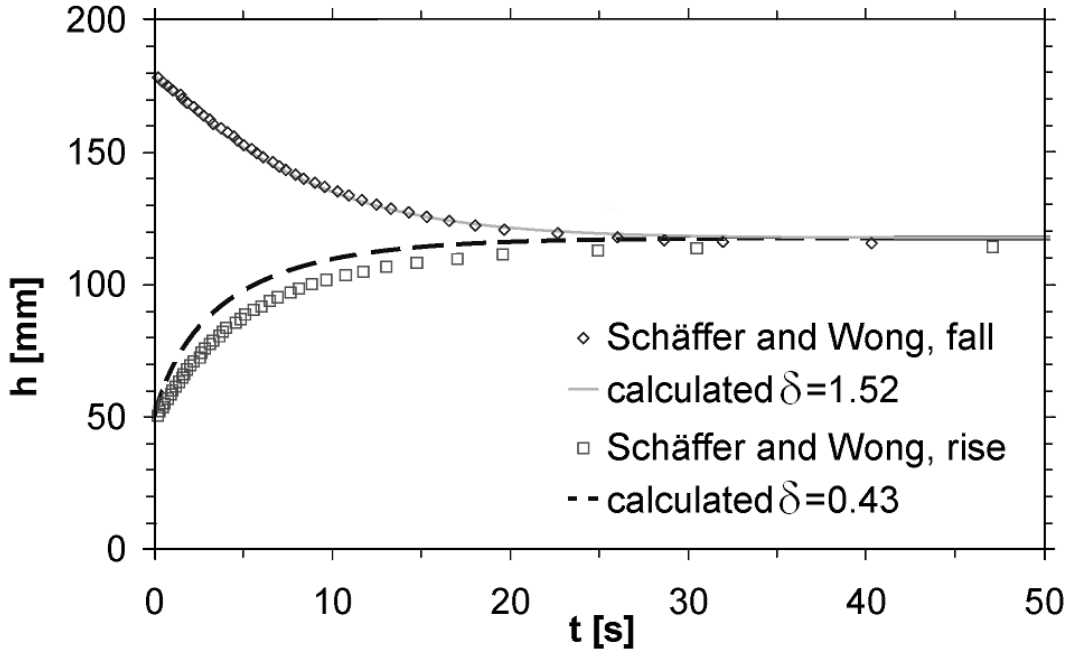


Figure 5.11: Comparison of experimental results by Schäffer and Wong [85] (water in 250 $\mu m$ diameter glass capillary) and the presented analytical solution.

an analytical solution for a more general initial condition is introduced which allows to evaluate the capillary fall of liquids. This is also discussed by means of dimensionless numbers and a plot showing the rise and fall regime is presented. A comparison of the derived mathematical solution with experimental literature values shows fairly good agreement.

# Chapter 6

# A basic macroscopic numerical simulation with FLOW-3D

To analyze the wicking of liquids into porous materials one can either perform experiments, use analytical models, or perform numerical simulations. Prior to considering a simulation tool reliable, a simple test case should be simulated for testing the model. Comparing the numerical results with experimental results allows to verify the model including the corresponding parameters. In this chapter the commercial CFD software FLOW-3D is used for a brief description and verification of its implemented porous media model. This solver is able to run a direct microscopic simulation of the wicking process as it occurs in porous media. For this kind of setup it is necessary to import the exact geometry of the porous structure with the individual pores and to define the surface tension, surface contact angle, density and viscosity of the liquid. Using free surface calculation methods the solver can simulate the wicking in every single pore. This technique, however, has some limitations, in particular when it comes to the simulation of a complete porous medium and not just an elementary cell. Due to the small size of the pores (some $\mu$m) in comparison to the typical relevant size of a porous medium ($\sim$50 mm), high numbers of meshing cells are necessary to resolve the individual pores and their characteristic geometry. Even when using new computer hardware the available calculation power is not sufficient to simulate wicking within reasonable time (e.g. several days calculation time). A first option to solve this problem is to conduct a microscopic numerical simulation of only a small, representative volume of the structure. The pore structure parameters $K$, $R_s$ and $\phi$ can be extracted from this microscopic simulation and then be used in a macroscopic simulation. The second option, which will be applied in the following, is to use experimental data to extract these parameters. FLOW-3D features a macroscopic porosity model, which does not simulate

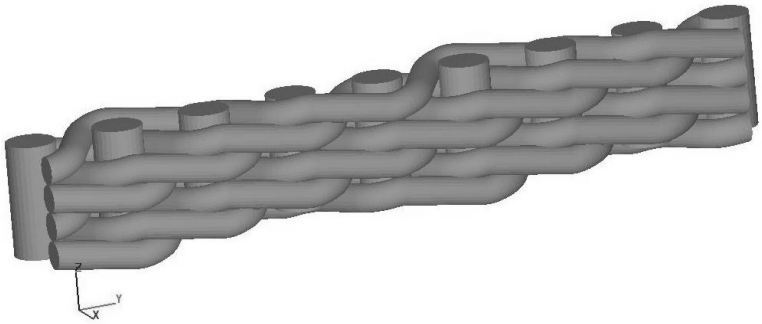

Figure 6.1: Digital representation of a DTW 200x1400 weave showing its microscopic structure.

the wicking of the liquid into the individual pores, but it uses integral (macroscopic) capillary pressure and flow resistance models to calculate the overall behavior of a porous medium in contact with a wetting liquid. Therefore much less cells are necessary when compared to a microscopic simulation, which drastically decreases the required calculation time. FLOW-3D solver 9.0.2 and interface 9.0.3 are used, applying the incompressible one fluid model with gravity effects (when desired). As the interface between wetted and dry medium is assumed to be sharp, no unsaturated flow occurs. So, choosing the volume fraction dependent model is a possible option for wicking simulation. This model uses the following drag correlation: In the modified Navier-Stokes equations solved by FLOW-3D (see FLOW-3D user manual v93 section 3.3.12) a term $-K_f\ v_i$ is added to the right hand side to account for flow losses in porous media or baffles. Here $v_i$ is the interstitial flow velocity and $K_f$ is a drag coefficient. For the volume fraction dependent model:

$$K_f = a_F V^{-b_F}. \tag{6.1}$$

Setting $b_F$ to 0 renders $K_f$ independent of the volume fraction $V$ and thus gives a constant factor $K_f = a_F$. When using the Darcy drag model

$$\Delta p = \mu h v_s \frac{1}{K} = \mu h v_i \frac{\phi}{K} \tag{6.2}$$

leads to

$$a_F = \frac{\mu}{\rho}\frac{\phi}{K} = \nu\frac{\phi}{K}. \tag{6.3}$$

Here, $h$ is not needed in the factor whereas density $\rho$ is required. The capillary pressure is calculated in analogy to Eq. (2.27), whereas in FLOW-3D it is defined to be positive

$$\Delta p = \frac{2\sigma cos(\theta)}{R_s}. \tag{6.4}$$

Considering these coefficients, the porosity and the capillary pressure can be entered in the porous media folder under “meshing and geometry”. In the following some simulation results

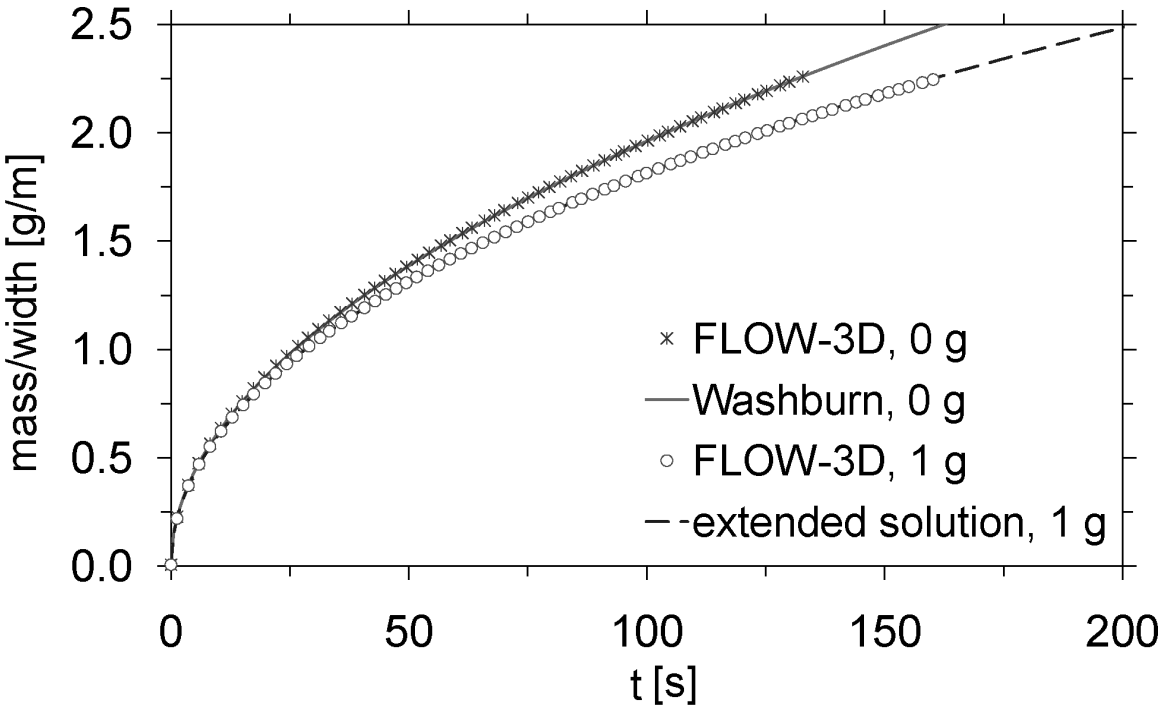


Figure 6.2: Fluid mass / width inside the weave plotted versus elapsed time. The points refer to the solutions by FLOW-3D, lines to the analytical solutions Eqs. (5.5) and (5.23). See Table 6.1 for simulation settings.

of HFE-7500 liquid wicking into a DTW 200x1400 metallic weave (warp direction) shall be presented. Here, two different cases with and without gravity are considered. The material properties like permeability etc. are taken from the experimental results presented in the next chapter (Table 7.8, mass method). The numerical results by FLOW-3D are compared to solutions of the momentum balance to verify the porous media model. The initial condition is a dry porous structure, where the boundary condition includes one boundary with a fluid fraction that is set to one to simulate the contact with the liquid reservoir. It is worth noting that the fluid volume which enters the weave is the main output parameter as it can be related to the wicking height and the fluid mass. It can be obtained in the postprocessing from the probe / general history / volume of fluid data. Fig. 6.2 shows a mass vs. time plot of the FLOW-3D simulations in comparison to the predicted values of the Lucas-Washburn equation, Eq. (5.5), neglecting gravity and the extended solution Eq. (5.23) including gravity.
A very good consistency with the simulated values of FLOW-3D can be seen, although the CFD data deviates minimally to lower values. This may be traced back to the inertia term which is considered in the FLOW-3D setup, while the analytical equations neglect it.

Table 6.1: Settings of the simulated wicking of HFE-7500 into a DTW 200x1400 metallic weave (warp direction) as presented in Fig. 6.2.

| | |
|---|---|
| Fluid properties (see Table 7.2) | |
| Density $\rho$ | 1610 [kg/m$^3$] |
| Viscosity $\mu$ | 1.24 [mPas] |
| Surface tension $\sigma$ | 16.2 [mN/m] |
| Porous solid properties (see Table 7.8) | |
| Static radius $R_s$ | 13.7 [$\mu$m] |
| Contact angle $\theta$ | 0° [-] |
| Capillary pressure $\Delta p$ | 2365 [Pa] |
| Porosity $\phi$ | 0.24 [-] |
| Permeability $K$ | 0.73 [$\mu$m$^2$] |
| Coefficient $a_F$ | 253212 [1/s] |
| Coefficient $b_F$ | 0 [-] |
| Geometry | |
| Sample size in $x$ axis | 25 [mm] |
| Number of cells in $x$ axis | 74 [-] |
| Sample size in $y$ axis | 0.149 [mm] |
| Number of cells in $y$ axis | 1 [-] |
| Sample size in $z$ axis | 50 [mm] |
| Number of cells in $z$ axis | 149 [-] |
| Boundary conditions | |
| Condition at "z min" | Specified pressure with F fraction = 1 |
| Other boundaries | Default symmetry |
| Solver settings | |
| Pressure solver | Implicit SOR |
| Viscous stress solver | Explicit |
| VOF advection | Automatic |
| Momentum advection | First order |
| Fluid flow solver | Solve momentum and continuity eq. |

# Part II

# Special investigated cases

# Chapter 7

# Linear capillary rise and the effect of evaporation

## 7.1 Introduction

The following chapter is based on the publication "The Effect of Evaporation on the Wicking of Liquids into a Metallic Weave" by N. Fries, K. Odic, M. Conrath and M. Dreyer [38]. As presented in the introduction (chapter 1.1), spacecraft Propellant Management Devices often use metallic screens to provide gas free delivery of propellant during all acceleration conditions of the flight. The screens are made of metal weaves and form passive surface tension devices. They allow propellant to penetrate but prevent gas from entering below a critical bubble point pressure. This mechanism requires the weave to be always saturated with propellant. If the screen is partially dry, wicking can be regarded as a self healing mechanism to restore saturation. Here, wicking performance strongly depends on the degree of evaporation from the porous screen. This is the motivation for this chapter, which shows how properties like the permeability of the weave are experimentally investigated, and which presents a new evaporation model that allows to predict the effect of evaporation on the capillary rise process. In addition to the investigation of a metallic weave, the capillary rise in porous filter frits is examined.

## 7.2 Applicable equations (no evaporation)

When a liquid encounters a solid medium (as shown schematically in Figs. 7.3 and 7.4), and the surface energies provide a contact angle smaller than 90°, a meniscus will rapidly form on the external surface of the structure. This process is called wetting and is applied in the Wilhelmy

plate method to measure surface tension. Here, the force acting on a plate in contact with a liquid is given by

$$F = P_b\,\sigma\cos(\theta), \tag{7.1}$$

with $P_b = 2(w+T)$ being the perimeter, $w$ the width and $T$ the thickness of the plate. If the solid medium is porous there will be also an internal wicking in addition to the external wetting. Both processes rely on the capillary pressure, but in contrast to the wetting process the internal menisci that drive the wicking are bound to the pore radius $R_s$. The internal wicking process has been discussed in the previous chapters, and the momentum balance featuring the Darcy law as introduced in section 2.5 is applied

$$-\rho\frac{d(h\dot{h})}{dt} = -\frac{2\sigma\cos(\theta)}{R_s} + \frac{\phi\mu h}{K}\dot{h} + \rho g h. \tag{7.2}$$

To extract the pore structure parameters $K$, $R_s$ and $\phi$ (see section 2.2) from capillary rise measurements some of the equations derived in the theoretical chapters of this book will be applied. For the convenience of the reader these shall be briefly reviewed in the following. As the structures investigated here typically feature pore sizes in the range of some $\mu$m inertial forces (local and convective) can be neglected for the relevant time stages (see section 3.2.1 for an evaluation of the influence of inertia). As discussed in chapter 5 on cases including gravity, an analytical solution to the momentum balance including capillary, viscous and hydrostatic forces can be given (see Eq. (5.23))

$$h(t) = \frac{1}{c}\left[1 + W\left(-e^{-1-\frac{c^2 t}{b}}\right)\right]. \tag{7.3}$$

From this the equilibrium height for $t \to \infty$ can be calculated (see Eq. (5.27))

$$h_{eq} = \frac{1}{c} = \frac{2\sigma\cos(\theta_s)}{\rho g R_s}. \tag{7.4}$$

This equation allows to determine the static radius $R_s$ if the liquid properties and $h_{eq}$ are known. To determine the parameter $K$, Eq. (7.3) may be fitted to the experimental rise data (see Fig. 7.12). However, a more convenient way is to use experimental data with $h < 0.1\,h_{eq}$. For this case, as discussed in section 5.4, gravity can be neglected accepting a minor error (3.54%). Thus a solution to the momentum balance including only capillary and viscous forces, the famous Lucas-Washburn equation Eq. (5.5), can be applied

$$h^2 = \frac{4\sigma\cos(\theta_s)}{\mu}\frac{K}{\phi R_s}t. \tag{7.5}$$

This equation shows that, for its area of validity, there is a linear correlation between $h^2$ and $t$, which easily allows to extract the conglomerate of parameters $K/(\phi R_s)$. A further method

to determine $K$ is to apply a defined pressure difference to a porous structure and measure the resulting flow rate. This was proposed by Darcy [24] as described in section 2.2.2.
To relate the imbibed fluid mass to the observed wicking height the following linear relation is assumed to hold

$$m = \phi\ \rho A_b h. \tag{7.6}$$

Here, $A_b = wT$ denotes the cross sectional area of the specimen. This equation can be applied to extract the porosity $\phi$ as discussed in section 7.3.4. With Eq. (7.6) the Lucas-Washburn equation Eq. (7.5) can be modified to give the mass gain $m$ instead of the height $h$, resulting in

$$m^2 = (A_b \phi \rho)^2 \frac{4\sigma \cos(\theta_s)}{\mu} \frac{K}{\phi R_s} t. \tag{7.7}$$

Finally all pore structure parameters can now be extracted from experimental data. $R_s$ from the maximum height, $\phi$ using a mass measurement (see Fig. 7.9), and $K$ using the capillary rise rate and the other parameters.

## 7.3 Experiments

### 7.3.1 Porous materials and fluid properties

Experiments were performed with a Dutch Twilled Weave (DTW) screen (see Fig. 7.1) typical for the use within PMDs, and filter frits with a chalk like appearance made of borosilicate glass (see Fig. 2.1 b). Filter frits are commercially available porous materials, which can be supplied with different pore sizes ranging from some $\mu$m (class P5) to several hundred $\mu$m (class P0). As they are standardized (P0-P5), inexpensive and can be machined into different specimen sizes and forms they can be regarded as an ideal material for capillary rise examinations in porous structures. Some parameters for the different classes are shown in Table 7.1.
Test liquids with similar physical properties as typical propellants for satellites (see Table 7.2) are used. All liquids used in the experiments feature a near zero contact angle with respect to the weave material, but different vapor pressures which allows to investigate the effect of evaporation. As the static contact angle $\theta_s$ between all test liquids and the weave is near zero, $\cos(\theta_s)$ is assumed to be equal to one for all experiment evaluations. Contrary to this, for the borosilicate glass frits and SF 0.65 test liquid a contact angle of $\theta_s = 16.3°$ as found by Stange [95] is applied.
The porous screen is a Dutch Twilled Weave (DTW) 200 × 1400 supplied by Spörl KG, Germany (Fig. 7.1 and Table 7.3). The samples are laser-cut to rectangular shapes with precise

Table 7.1: Characterization of the glass filter frits. The data is extracted from diagrams provided by the supplier (ROBU Glasfilter GmbH, Germany). $R_{50}$ denotes the pore radius where 50 % of the pores are smaller (or larger) compared to this radius.

| Filter frit type | pore diameter [$\mu$m] | $R_{50}$ [$\mu$m] | $\phi$ [-] |
|---|---|---|---|
| P0 | 160-250 | 95 | 0.33 |
| P1 | 100-160 | 65 | 0.34 |
| P2 | 40-100 | 35 | 0.36 |
| P3 | 16-40 | 12 | 0.41 |
| P4 | 10-16 | 5.5 | 0.42 |
| P5 | 1-1.6 | 0.675 | 0.48 |

Table 7.2: Fluid properties at 25 °C. Source: product data sheet of the listed liquids (3M for HFE 7500, FC-77, FC-72, FC-87 and Dow Corning for Silicone Fluid 0.65).

| | $\sigma$ | $\rho$ | $\mu$ | $p_v$ |
|---|---|---|---|---|
| | $10^{-3}$ [N/m] | [kg/m$^3$] | $10^{-3}$ [Pas] | $10^3$ [Pa] |
| SF 0.65 | 15.9 | 758 | 0.49 | 4.4 |
| HFE-7500 | 16.2 | 1610 | 1.24 | 2.1 |
| FC-77 | 15.0 | 1780 | 1.28 | 5.6 |
| FC-72 | 12.0 | 1680 | 0.64 | 30.9 |
| FC-87 | 9.0 | 1650 | 0.45 | 81.1 |

dimensions ($H = 50$ mm by $w = 10, 14, 16$ or 18 mm). They either have the warp wires or the weft wires running perpendicular to the screen width. If the wicking process is occurring parallel to the warp wires the flow is defined to be in warp direction, if parallel to the weft wires in weft direction. The microstructure quality of each specimen is checked using a microscope to detect any defects at the edges of the sample. Subsequently, the selected weave undergoes a cleaning protocol that removes any dust or grease left on the surface or in the interstices. This is performed using an ultrasonic bath with the metal cleaner Turco (supplier: Henkel AG, Germany).

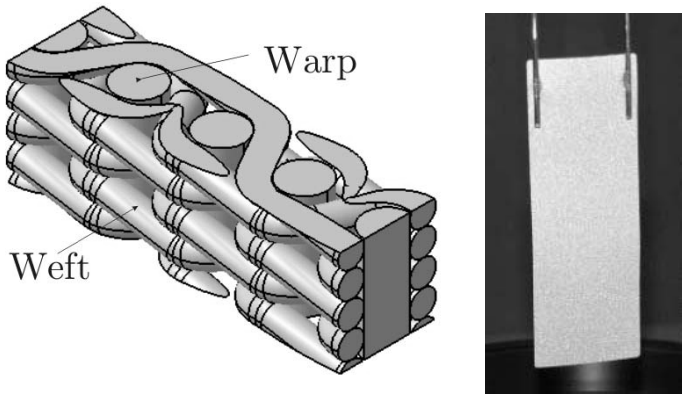


Figure 7.1: Drawing of the microstructure (left) and photograph (right) of the Dutch-Twilled weave (DTW) 200 × 1400.

Table 7.3: Properties of the weave.

| | |
|---|---|
| weave material | AISI 304 L<br>(stainless steel) |
| type<br>200 × 1400 | Dutch Twilled Weave<br>200 warp wires/inch<br>1400 weft wires/inch |
| warp wire diameter [$\mu$m] | 70 |
| weft wire diameter [$\mu$m] | 40 |
| $H$: weave height [mm] | 50 $\pm$0.01 |
| $T$: weave thickness [$\mu$m] | 149 $\pm$1 |
| $w$: weave width [mm] | (10,14,16,18) $\pm$0.01 |

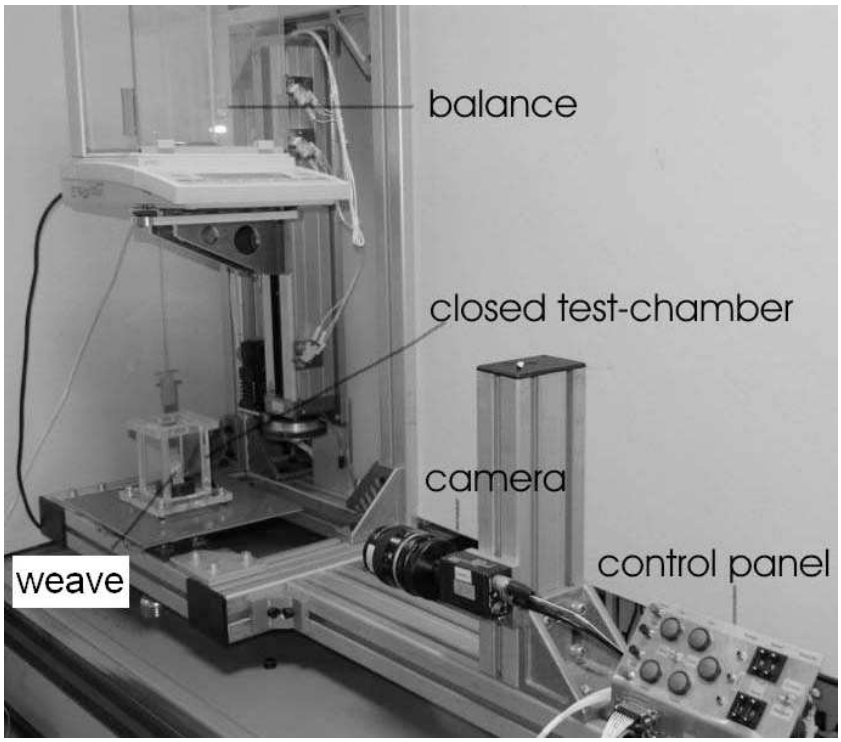


Figure 7.2: Photography of the wicking experimental setup.

### 7.3.2 Experimental setup and data acquisition

Fig. 7.2 displays an overview of the wicking experimental setup. Basically the setup consists of

- a rectangular test chamber (50x50 $mm^2$ base area, 90 mm height) that contains the test liquid and the specimen suspended above the liquid surface,
- a video camera to record the wicking liquid front height versus time,
- an electronic balance with an accuracy of $\pm 0.3$ mg to which the specimen is attached by threads.

Fig. 7.3 shows a sketch of the arrangement. The weave is positioned for 1 hour above the test liquid surface prior to the experiment start. During this time no increase in the sample mass is recorded for all test liquids which means no significant capillary condensation occurs in the weave. For experiments with filter frits the waiting period is less important as due to their higher thickness evaporation is of less importance when compared to the very thin weaves. Again, for filter frits no increase in mass was observed before contact with the liquid.
The test chamber is closed, however there are two holes in the cover to attach the specimen to the balance. Vapor diffusion through these holes can be adjusted as the size of the holes can

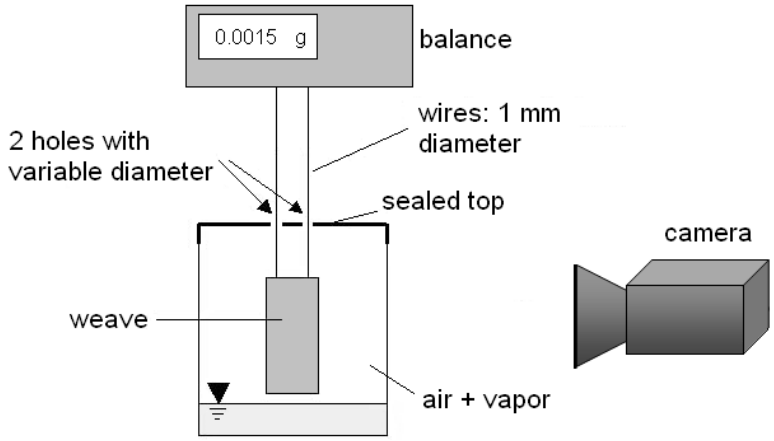


Figure 7.3: Sketch of the test chamber prior to wicking experiments.

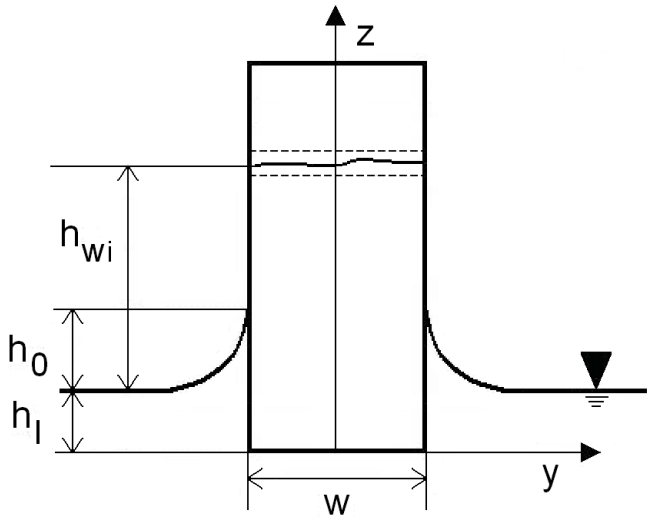


Figure 7.4: Coordinates applied to the weave sample.

be varied to investigate different evaporation rates. To further increase the evaporation rate the sealing top can be left open. The gaseous environment is therefore composed of air and vapor of the test liquid. The recording of the wicking front is done with a camera at 25 Hz. The resolution of the camera and the lens is 0.07 mm/pixel. The balance can be precisely and continuously moved up and down by means of an automated lift in order to sink the specimen into the test liquid with a constant velocity of 1 mm/s. Data acquisition is controlled using the commercial software LabVIEW. The applied coordinate system is illustrated by Fig. 7.4 where the weave is immersed in the test liquid. Here, $h_{wi}$ is the height due to the wicking process. $h_l$ is the immersion depth of the weave in the liquid, a safety length to ensure contact with the test liquid: $h_l \approx 0.55$ mm. $h_0$ is the height up to which the specimen is covered with liquid due

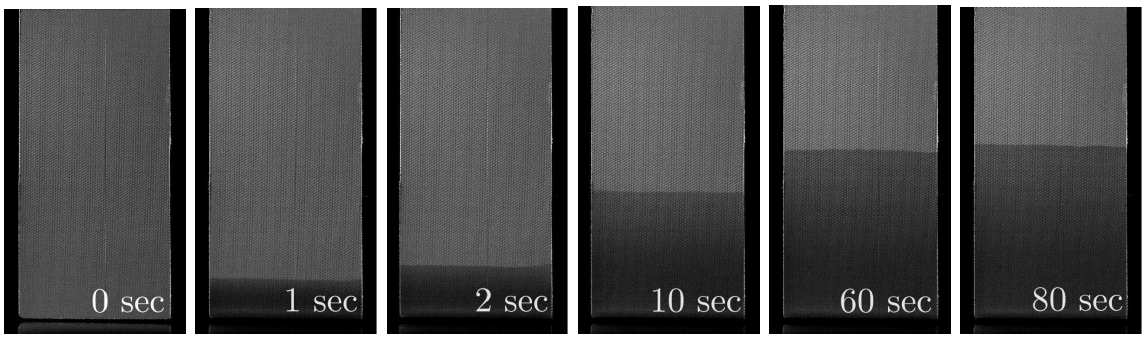


Figure 7.5: Subsequent series of images showing wicking of HFE-7500 into the weave.

to the wetting phenomenon. The overall height of the liquid front is the sum of two heights

$$h = h_{wi} + h_0, \tag{7.8}$$

while $h_l$ contributes to a decrease in measured mass due to buoyancy.

### 7.3.3 DTW: capillary rise experiments - height approach

By measuring the equilibrium wicking height $h_{\text{eq}}$ that occurs due to the balance between the capillary and the gravity forces (see Eq. (7.4)), the static radius $R_s$ can be calculated and thus, knowing $K/R_s$ from an other experiment, the permeability $K$. The equilibrium height is typically reached after about five days of liquid rise. In order to measure $h_{\text{eq}}$, an additional larger scale setup is used as $h_{\text{eq}}$ (depending on the liquid) is higher than the test chamber. The larger setup did not feature a balance but was sealed to provide a saturated environment. Due to their high volatilities no experiments were conducted with FC-72 and FC-87. Also, as noted by Kaya [52] (p.83) the experimental setup and the weave was not high enough to determine the maximum height using SF 0.65 as a test liquid. The experimental results and the calculated values of $R_s$ are presented in Table 7.4. Note that in [52] Kaya obtains a slightly different $R_s$ value for FC-77 due to usage of different liquid properties. On the right hand side of Table 7.4 a mean value for bubble point measurements performed with HFE-7500, SF 0.65 and Turco [72] is shown. The data is obtained using a commercially available pore size meter PSM 165 by Topas GmbH, Germany. This device determines the bubble point pressure and allows to calculate the maximum pore size from that measurement. It can be seen that the obtained value fits in between the $R_s$ data obtained by the maximum height method.

From Table 7.4 it can be seen that the calculated value of $R_s$ can deviate significantly from measurement to measurement. In anticipation of a later comparison with literature values

Table 7.4: Measured equilibrium heights for different test liquids in a closed large test chamber. The second line displays the corresponding calculated values of $R_s$ using the liquid properties of Table 7.2. For comparison, on the right hand side data from bubble point measurements [72] is presented.

| Fluid | HFE-7500 (exp1) | HFE-7500 (exp2) [52] | FC-77 [52] | $R$ (bubble point) [72] |
|---|---|---|---|---|
| $h_{eq}$ [mm] | 150 ± 10 | 210 ± 2.1 | 180 ± 1.8 | - |
| $R_s$ [$\mu$m] | 13.7 ± 0.95 | 9.77 ± 0.1 | 9.54 ± 0.1 | 10.08 ± 0.8 |

(see Table 7.8) it can be stated that even larger deviations of this value occur in the literature, which can be traced back to the significant impact of evaporation [38]. Though the experiments presented here (Table 7.4) were conducted in a closed test chamber, evaporation may still occur due to local temperature gradients. In the following, to be consistent with [38], a value of $R_s = (13.7 \pm 0.95)$ $\mu$m will be used. To extract the permeability $K$ out of experimental results, the linear part of $h^2(t)$ and $m^2(t)$ graphs can be used. In this domain of the wicking process the influence of gravity is negligible. Using Eq. (7.5) the parameter $K/R_s$ is extracted from the slope of the $h^2(t)$ curve. An image series of the wicking process is presented in Fig. 7.5. The single frames of an image series are then processed with the commercial software MatLab to extract the actual wicking height. At the liquid front line, a mean height out of all pixel along the total width of the weave is calculated with a standard deviation of ±5 pixel.
Fig. 7.6 shows the resulting time dependencies of the wicking height for three test liquids and a 16 mm wide screen. As expected the slope is much steeper in the beginning of the measurement and decreases in time.
In Fig. 7.7, the squared height is plotted versus time. Near the origin a constant slope can be seen where a linear regression curve is calculated using the method of least squares to extract the pore parameters. For the linear regression the experimental values between the origin of the curve and $h$ up to about 10% of the equilibrium height $h_{eq}$ are used. This is consistent with the analytical considerations presented in section 5.4, where it is predicted that for $h$ up to 10% of $h_{eq}$ gravity can be neglected accepting a minor error (3.54%). For SF 0.65 $h_{eq} = 312$ mm is calculated using $R_s = 13.7$ $\mu$m. It is visible in Fig. 7.7 that for $h > 0.1\, h_{eq}$ the meniscus heights of SF 0.65 deviate to lower values than predicted by the linear regression. This is in agreement with the analytical models and can be traced back to the influence of gravity.

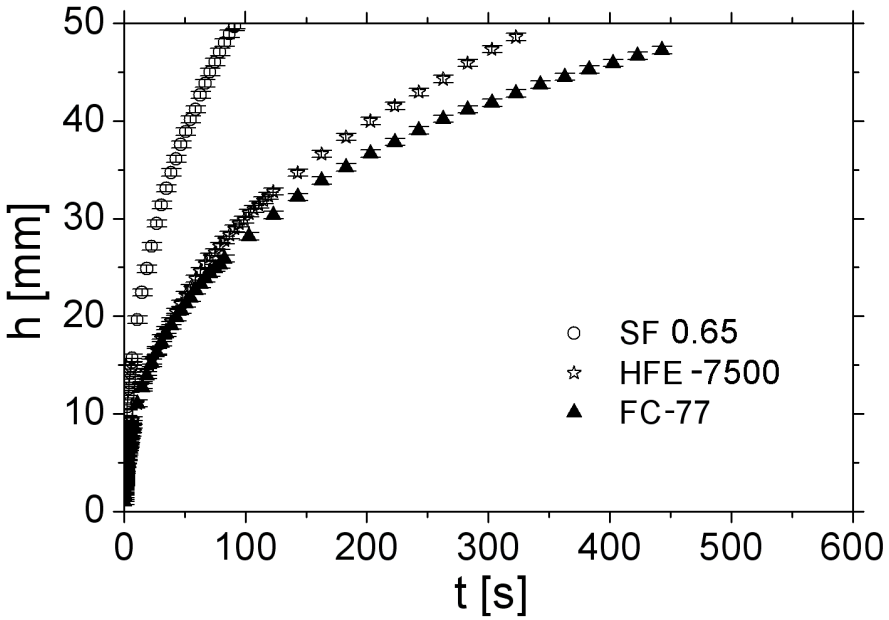


Figure 7.6: Wicking height raw data ($w = 16$ mm, warp direction) with error bars (standard deviation is $\pm 5$ pixel).

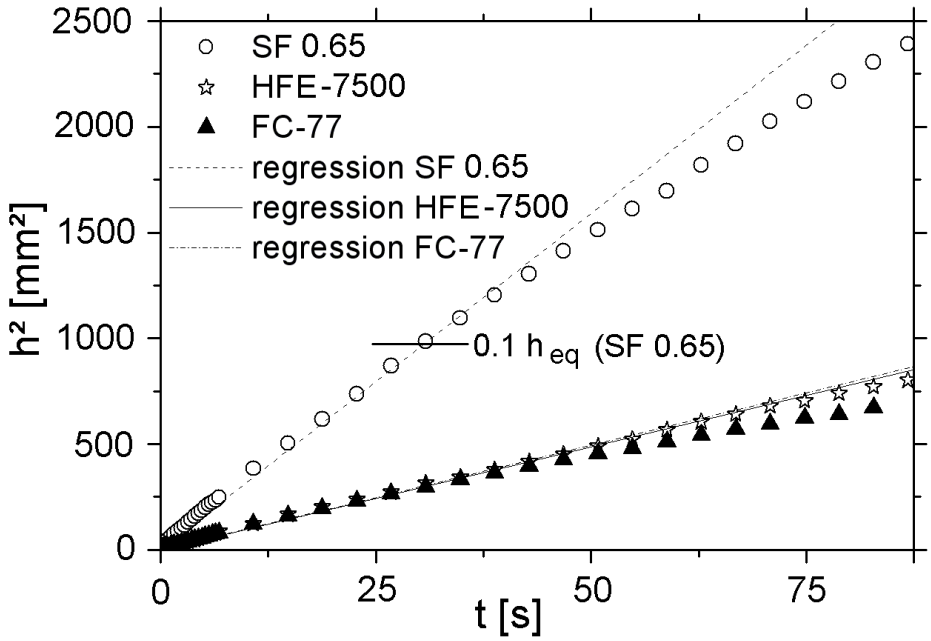


Figure 7.7: Squared height over time ($w = 16$ mm, warp direction) with linear fitting (no error bars for graph clarity). Mark at $h = 0.1\, h_{eq}$ for SF 0.65. For higher values of $h$ gravity has to be taken into account, the linear regression overestimates the values.

Table 7.5: $K/R_s$ calculated from height measurements ($w = 16$ mm, warp direction). Number in brackets is the correlation coefficient $r^2$, $\pm$ refers to the standard deviation. $K$ calculated with $R_s = 13.7$ $\mu$m.

| | $K/R_s$ (experimental) [$\mu$m] | $K$ [$\mu$m$^2$] |
|---|---|---|
| SF 0.65 | 0.0589 (0.995) | 0.81 |
| HFE-7500 | 0.0448 (0.997) | 0.61 |
| FC-77 | 0.0506 (0.992) | 0.69 |
| Average | 0.0514 $\pm$0.0071 | 0.70 $\pm$0.10 |

Table 7.5 contains the $K/R_s$ results for different fluids and their correlation coefficient. The values from Table 7.5 reveal that there is a small deviation between the measurements made with different liquids. The average is $K/R_s = 0.0514$ $\mu$m with a standard deviation of 0.0071 $\mu$m. Further measurements were also conducted using weaves with different widths ranging from 10 to 18 mm but a comparison of the results showed no significant influence of the width.

### 7.3.4 DTW: capillary rise experiments - mass approach

The chronology of a mass measurement is shown in Fig. 7.8. The curve is divided into six parts, describing the weave from the imbibition to the drying. At first, the weave is brought into contact with the test liquid inducing the wetting process. The liquid will then start to wick into the weave, while the mass will increase to finally reach a plateau value. In the absence of evaporation this corresponds to the equilibrium state between capillary and hydrostatic pressure. During the de-wetting the contact between weave and liquid is lost and the outer meniscus detaches. Finally, the last step belongs to liquid evaporation out of the weave which will only take place in unsaturated environments (e.g. open test chamber). This part of the curve is of great interest to evaluate the evaporation rate and will be described in further detail later. The result of a wicking mass versus wicking height measurement is shown in Fig. 7.9. It verifies the linear behavior and furthermore allows to calculate the "wicking effective porosity". Other methods to measure or predict the porosity of a weave are discussed in section 2.2.1 or by Armour and Cannon [2]. Using Eq. (7.6) the porosity can be calculated out of the slope (see Fig. 7.9) to be $\phi = 0.24 \pm 0.03$. Kaya [52] (p.88) applied a different method to determine the porosity, however, with fairly similar results. The weight of a completely dry specimen was measured, then the specimen submerged into HFE-7500 (known density, see Table 7.2) until it

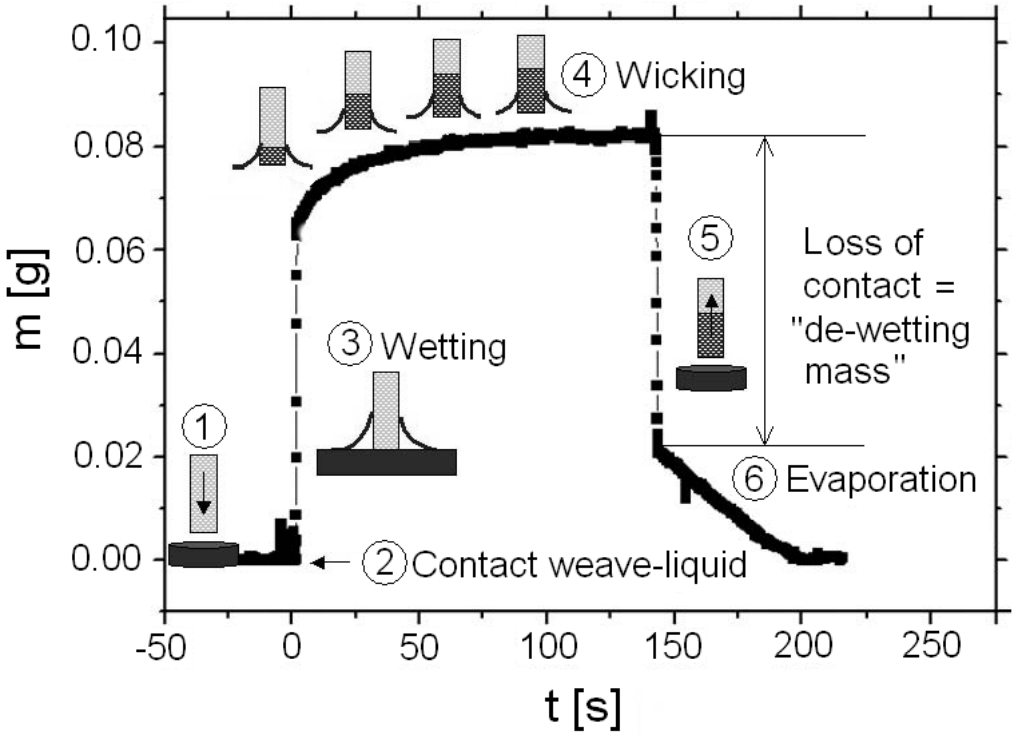


Figure 7.8: Mass versus time curve (open test chamber). Imbibition of a weave (50x16 mm) by HFE-7500. The "de-wetting mass" is measured to be 0.0613 g, while the Wilhelmy plate method Eq. (7.1) predicts 0.0533 g.

was saturated. Finally the mass of the wet specimen was determined. The difference in mass can be accounted to the liquid in the pores and by knowing the dimensions of the specimen Eq. (2.1) was used to obtain $\phi = 0.247 \pm 0.006$ based on three experiments with different specimen sizes. Comparing these results with the data provided by the supplier (Spörl KG, Germany), $\phi = 0.33$, shows that the measured, effective values are considerably lower than the value provided by the supplier. However, the supplier does not state how the porosity was measured or estimated and mark their value as approximate.

According to Eq. (7.7) mass measurements can be used to calculate pore structure parameters like the permeability of the weave. The advantage of this "mass method" is that no image processing is necessary to evaluate the wicking height from video recordings. When considering experimental investigations using cryogenic liquids the mass method is an attractive alternative. This results from a tendency of cryogenic liquids to render optical methods unpracticable due to condensation on lenses. However, the mass method also features some disadvantages when compared to the optical measurement. As the weave is basically a two dimensional medium (0.15 mm thickness compared to 16 mm width) its wetted circumference is large compared to its

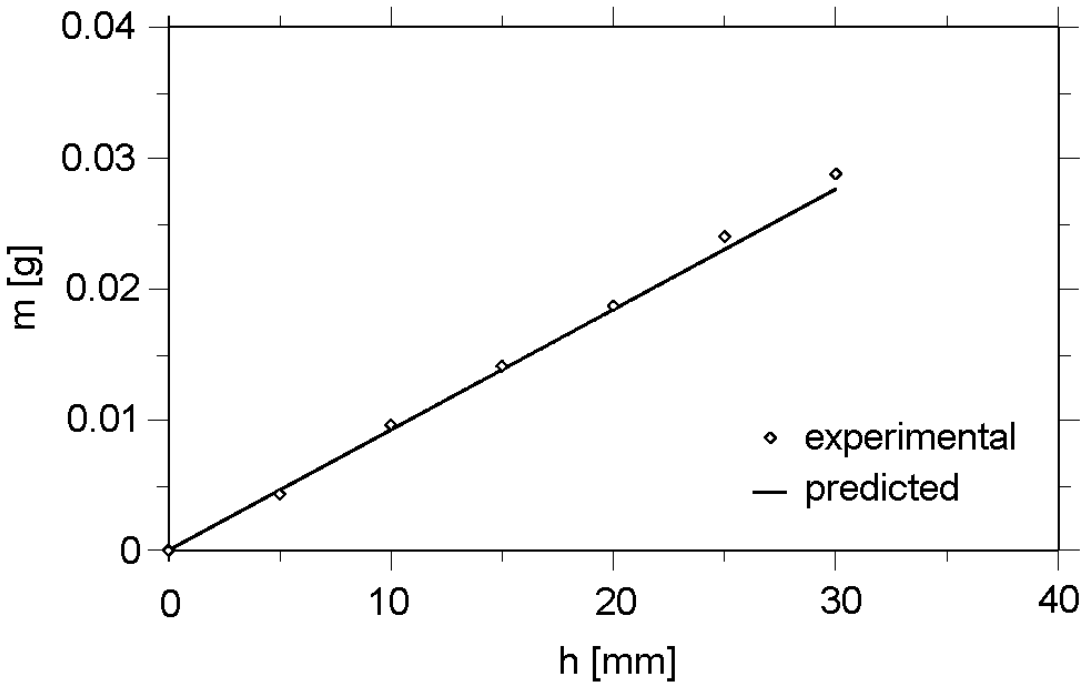


Figure 7.9: Measurement of $\phi$: Liquid mass inside the weave versus wicking height (HFE-7500 in 16 mm wide sample, warp direction). Prediction using Eq. (7.6).

volume. Thus the initial effect of wetting, the attachment of an outer meniscus to the weave, is a significant rise in mass when compared to the mass gain due to the wicking effect. As Fig. 7.8 illustrates, the wetting mass gain within a fraction of the first second is a significant portion of the total mass gain. Also, when the weave is brought into contact with the liquid, both effects occur at the same time. To obtain the "real wicking mass" the "de-wetting mass" (see Fig. 7.8) is subtracted from the mass raw data, as the initial jump in mass (in Fig. 7.8 measured to be 0.0644 g) refers to both the wetting and wicking process. For the same case the "de-wetting mass" is measured to be 0.0613 g. Using the Wilhelmy plate method Eq. (7.1) for an identical setup gives a predicted force of 0.5232 mN, which is equal to a mass of 0.0533 g. Comparing the predicted mass and the measured "de-wetting mass" shows that both are in fairly good agreement. Analogous to the height method, Fig. 7.10 shows the squared wicking mass gain plotted versus time. From the slope of the $m^2(t)$ curves the weave parameters presented in Table 7.6 were calculated using Eq. (7.7). The values of Table 7.6 show good agreement with the ones calculated with the height method (Table 7.5).

The results presented in Table 7.7 refer to the capillary rise in weft direction. It is assumed that

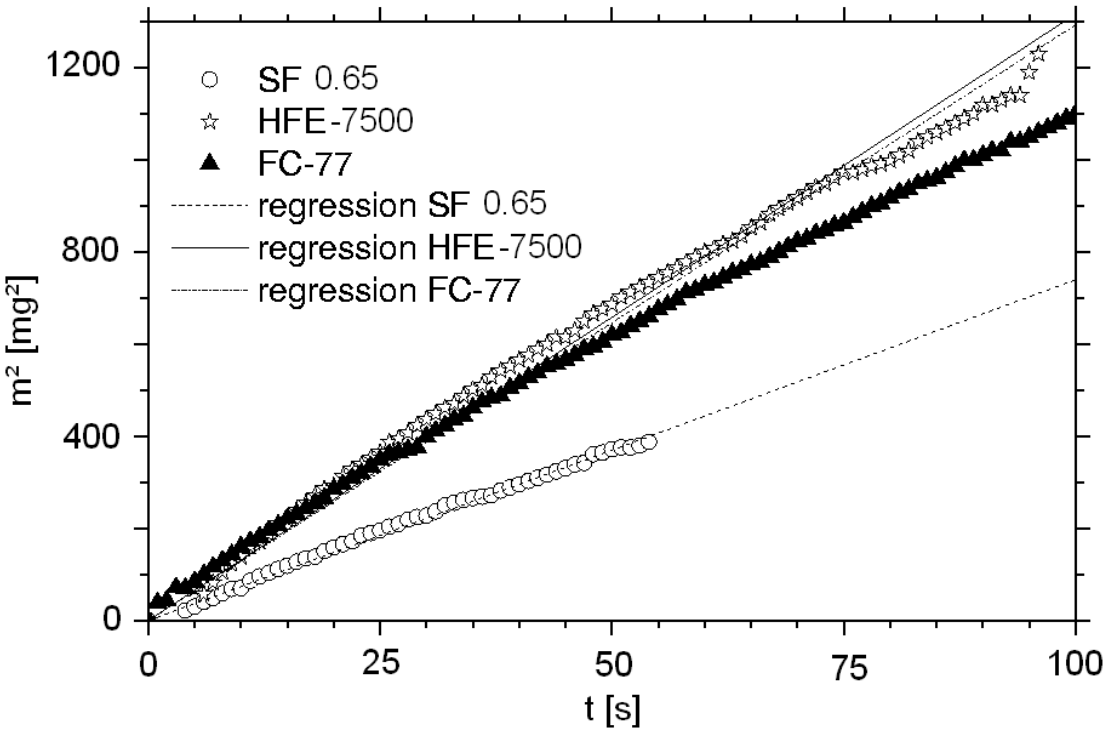


Figure 7.10: Squared mass over time (warp direction) with linear fitting (no error bars for graph clarity).

the static radius $R_s$ that defines the capillary pressure is equal for warp and weft direction. The mass and height curves for the weft direction are fairly similar to the ones in warp direction, however the liquid rises more slowly. This is due to the higher flow resistance in the weft direction. This can also be seen by the permeability $K$ in Table 7.7 which is about half the value of $K$ for the warp direction. An overview of the experimental findings is provided by Table 7.8. It also shows a comparison of the obtained results with literature which verifies the presented results to some extent. In his work [28] Dodge uses his experiments [29] - where evaporation is not suppressed - as a reference. Thus, the higher evaporation rate may explain the deviation. Dodge [28] does not use the pore parameters used in this work but his parameters can be converted by the following correlations

$$\frac{\Phi_w}{D_{\mathrm{BP}}} = \frac{2}{R_s} \tag{7.9}$$

and

$$\frac{C_w}{B_s^2} = \frac{\phi}{K}. \tag{7.10}$$

Dodge [28] defines $\Phi$ as a screen characteristic parameter (not the porosity), $D_{\mathrm{BP}}$ as the effective pore diameter, $C_w$ as a wicking friction parameter and $B_s$ as the screen thickness. Symons [98]

Table 7.6: $K/R_s$ for the warp direction calculated from mass measurements ($w$ = 18 mm). Number in brackets is the correlation coefficient $r^2$, ± refers to the standard deviation. $K$ calculated with $R_s = 13.7$ $\mu$m.

| | $K/R_s$, warp [$\mu$m] | $K$, warp [$\mu$m$^2$] |
|---|---|---|
| SF 0.65 | 0.0565 (0.993) | 0.77 |
| HFE-7500 | 0.0544 (0.996) | 0.75 |
| FC-77 | 0.0496 (0.999) | 0.68 |
| Average | 0.0535 ±0.0035 | 0.73 ±0.05 |

uses a correlation constant $c$. For the static radius in warp direction Dodge obtains $R_s$ = 88.1 $\mu$m and 124.4 $\mu$m for the weft direction. Symons uses $R_s = 7.0$ $\mu$m for warp and weft direction alike, however this value is based on the manufacturer's rated pore size. Altogether it can be seen that there is fair agreement between the $K/R_s$ values, however discrepancies for the $R_s$ results which may be explained by the sensitivity of the experiment to evaporation.

Table 7.7: $K/R_s$ for the weft direction calculated from mass measurements ($w$ = 16 mm). Numbers in brackets are correlation coefficients $r^2$, ± refers to the standard deviation. $K$ calculated with $R_s = 13.7$ $\mu$m.

| | $K/R_s$, weft [$\mu$m] | $K$, weft [$\mu$m$^2$] |
|---|---|---|
| SF 0.65 | 0.0255 (0.987) | 0.35 |
| HFE-7500 | 0.0283 (0.996) | 0.39 |
| FC-77 | 0.0259 (0.998) | 0.35 |
| Average | 0.0266 ±0.0015 | 0.36 ±0.02 |

Table 7.8: Overview - experimental results for DTW 200x1400 and comparison with literature (Dodge [28] and Symons [98]).

| | This work | Dodge | Symons |
|---|---|---|---|
| $\phi$: porosity | 0.24 ±0.03 | | 0.272 |
| $R_s[\mu m]$, warp | 13.7 ±0.95 | 88.1 | 7.0 |
| $R_s[\mu m]$, weft | 13.7 ±0.95 | 124.4 | 7.0 |
| | By height method | Dodge | Symons |
| $K[\mu m^2]$, warp | 0.70 ±0.10 | | |
| | By mass method | Dodge | Symons |
| $K[\mu m^2]$, warp | 0.73 ±0.05 | | |
| $K[\mu m^2]$, weft | 0.36 ±0.02 | | |
| $K/R_s[\mu m]$, warp | 0.0535 | 0.0408 | 0.0462 |
| $K/R_s[\mu m]$, weft | 0.0266 | 0.0132 | 0.0150 |

### 7.3.5 Filter frits: capillary rise experiments - mass approach

In the following text some experiments conducted with glass filter frits (introduced previously in section 7.3.1) are presented. The first aim is to derive their pore structure parameters $K$, $R_s$ and $\phi$ for possible future applications of these materials. The second aim is to apply some of the previously derived equations to the capillary rise of SF 0.65 in these structures.

In Fig. 7.11 some raw data from mass recordings are presented. Two different types of filter frits are used, while SF 0.65 is the test liquid. The numbers denote: 1) The initial increase in mass due to external wetting. It is, in proportion to the overall mass increase, considerably smaller when compared to the thin, metallic weaves. 2) A plateau is reached: at this point the complete specimen is filled with liquid, thus the wicking comes to a sudden stop. Note that for the frit class P1 the plateau is not reached with a kink. Here it is the hydrostatic pressure which limits the capillary rise. 3) At this point the porous specimen is lowered out of the liquid. After an initial increase in mass the mass drops when the contact is lost. After this, a very slow decrease in mass which can be attributed to evaporation can be observed (compare to Fig. 7.8, which displays a much thinner weave). Table 7.9 displays the sizes of the samples used for the capillary rise test. It also presents the actual measured de-wetting mass (plateau to plateau) and the theoretical mass predicted by the Wilhelmy plate equation Eq. (7.1). It can

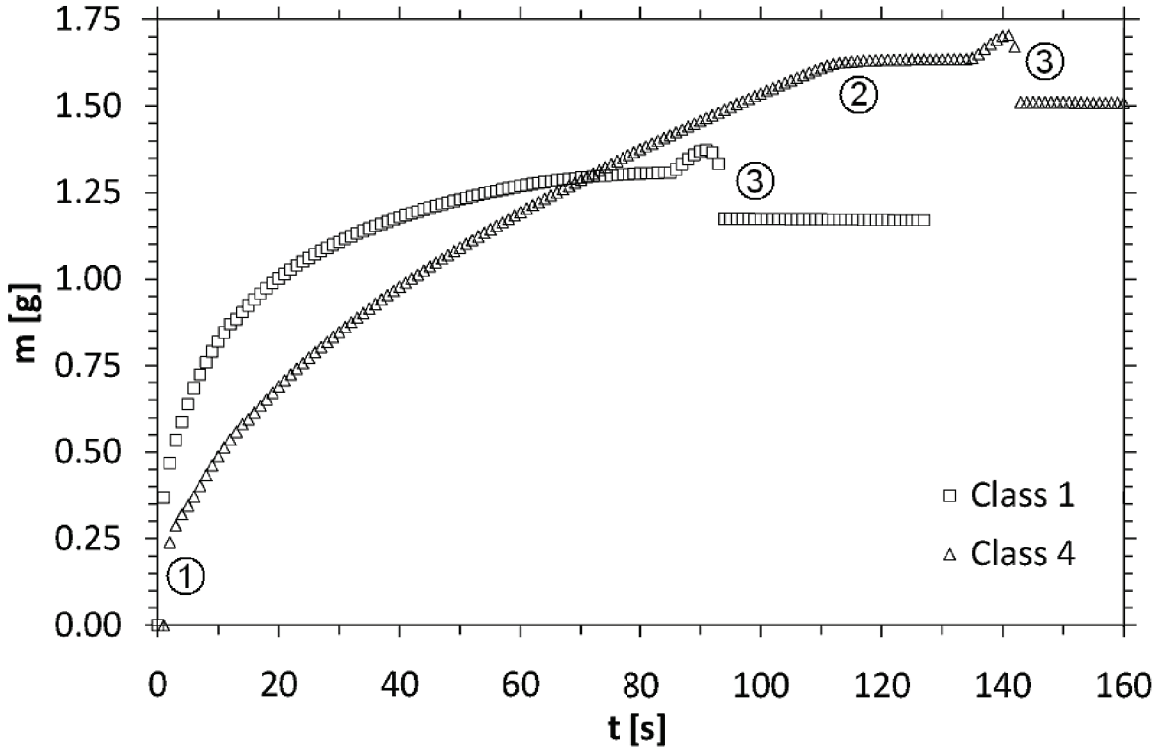


Figure 7.11: Raw mass data recording for filter frits class P1 and P4 in SF 0.65. The numbers denote stages of the experiment as described in the text. The precision of the balance is ±0.3 mg, thus no error bars are visible. However, the error of repeatability is found to be ∼10 %.

be seen that the actual mass is about two times the mass predicted by the Wilhelmy method. It is assumed that this increase in mass is contributed by liquid below the porous sample raised above mean liquid level, and not by the outer meniscus itself. This would also explain why this additional mass is missing for the very thin metallic weaves previously investigated.

Table 7.10 presents some parameters extracted from the experimental data. The porosity $\phi$ is calculated using the mass inside the wetted structure and the volume of the structure. For type P0 the specimen is beforehand completely submerged in test liquid to ensure that it is fully saturated, as the equilibrium height is lower that the height of the specimen. For the other frit types the mass after the normal rise process is taken. The obtained value is in fairly good agreement with the supplier specification, see Table 7.1. The value $K/R_s$ is determined from the linear part of the capillary rise as previously introduced for metallic weaves (section 7.3.4). Two different types of radii are shown. The first is the static radius $R_s$, for P1 - P3 obtained from fitting Eq. (7.3). The second one is a radius denoted $R$ (bubble point), which is obtained from a different experimental setup. Here a commercially available device, the PSM

Table 7.9: Specimen size of the used glass filter frit specimen.

| Filter frit type | height [mm] | $w$ [mm] | $T$ [mm] | de-wetting $m$ [g] | Wilhelmy $m$ [g] |
|---|---|---|---|---|---|
| P0 | 50 | 15.97 | 6.85 | 0.14 | 0.074 |
| P1 | 50 | 14 | 6.33 | 0.14 | 0.066 |
| P2 | 50 | 14 | 7.33 | 0.15 | 0.069 |
| P3 | 50 | 14.8 | 5.5 | 0.09 | 0.066 |
| P4 | 50 | 14.5 | 6 | 0.13 | 0.067 |
| P5 | 49.5 | 14.75 | 5 | 0.09 | 0.064 |

165 by Topas GmbH, Germany, is used to determine the bubble point, see Meistering [72]. From this bubble point the radius of the largest pore can be extracted. Here, the mean value of measurements using HFE-7500 and Topor test liquid [72] are used. For P0 no value is provided as the bubble point is lower than the allowed sensor reading of the device. Note that for class P4 and P5 $R_s$ is not determined by fitting of Eq. (7.3), as for these the curves using $R$ from the bubble point measurement already provides a fairly good agreement. Finally, Fig. 7.12 displays the height calculated using the mass measurement and Eq. (7.6). Note that the capillary rise always stops at $h = 50$ mm as this is the height of the specimen. The lines are a fit of the analytical solution Eq. (7.3) including the Lambert W function. Fairly good agreement can be observed.

Table 7.10: Overview of experimental results and the estimated errors for filter frits calculated from mass measurements.

| Filter frit type | $\phi$ [-] | $K/R_s$ [$\mu$m] | $R_s$ [$\mu$m] | $R$ (bubble point) [$\mu$m] [72] |
|---|---|---|---|---|
| P0 | 0.28 $\pm$0.03 | 0.215 $\pm$0.031 | - | - |
| P1 | 0.35 $\pm$0.04 | 0.235 $\pm$0.036 | 50 $\pm$10 | 76.7 $\pm$7.6 |
| P2 | 0.42 $\pm$0.04 | 0.187 $\pm$0.029 | 10 $\pm$2 | 37.7 $\pm$3.8 |
| P3 | 0.41 $\pm$0.04 | 0.116 $\pm$0.018 | 7.4 $\pm$1.5 | 15.3 $\pm$1.5 |
| P4 | 0.46 $\pm$0.05 | 0.083 $\pm$0.012 | - | 4.44 $\pm$0.44 |
| P5 | 0.50 $\pm$0.05 | 0.0594 $\pm$0.0089 | - | 3.74 $\pm$0.37 |

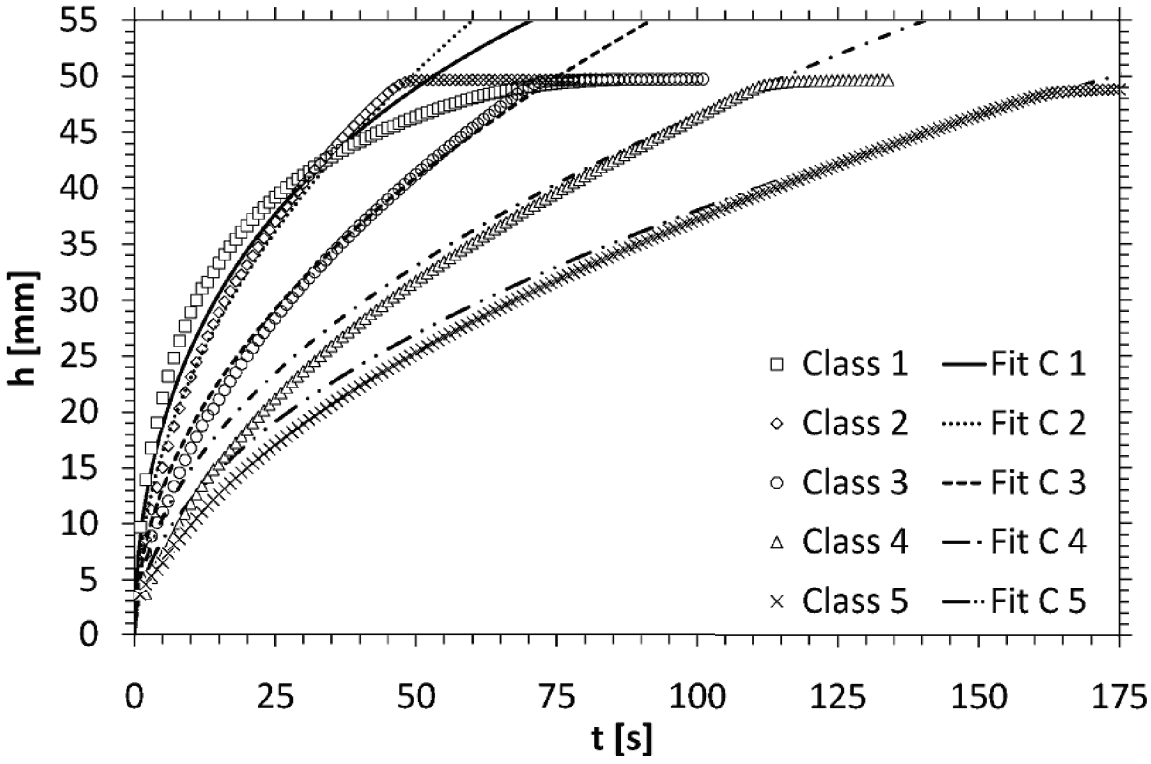


Figure 7.12: $h$ calculated from mass measurements of different filter frits in SF 0.65 (no error bars for graph clarity). The lines denote a fit of Eq. (7.3), which includes capillary, viscous and hydrostatic forces.

### 7.3.6 DTW: The effect of evaporation

Looking at Fig. 7.8, evaporation affects the periods 4 and 6. It is the only and therefore crucial mechanism for the drying period 6, which is used for its measurement. It is characterized by the evaporation rate $\dot{m}_e$ which is the mass of evaporated liquid per area and time [kg/m$^2$ s]. $\dot{m}_e$ has to be calculated individually for each experiment as it depends on the used test liquid, temperature and saturation of the surrounding air. To obtain different values of the evaporation rate the size of a ventilation hole on top of the test chamber was varied. Assuming evaporation from both sides of the weave the total mass flow due to evaporation is

$$\dot{M}_e = 2\dot{m}_e h(w + T). \tag{7.11}$$

The evaporation mass curves can roughly be divided into two drying periods. The first part of the curve is linear and corresponds to the drying when the weave is completely saturated. The second part which is nonlinear reveals a reduction of the drying rate when the amount of liquid is reduced below a certain level in the weave structure. As given by Kaviany [50], the liquid is

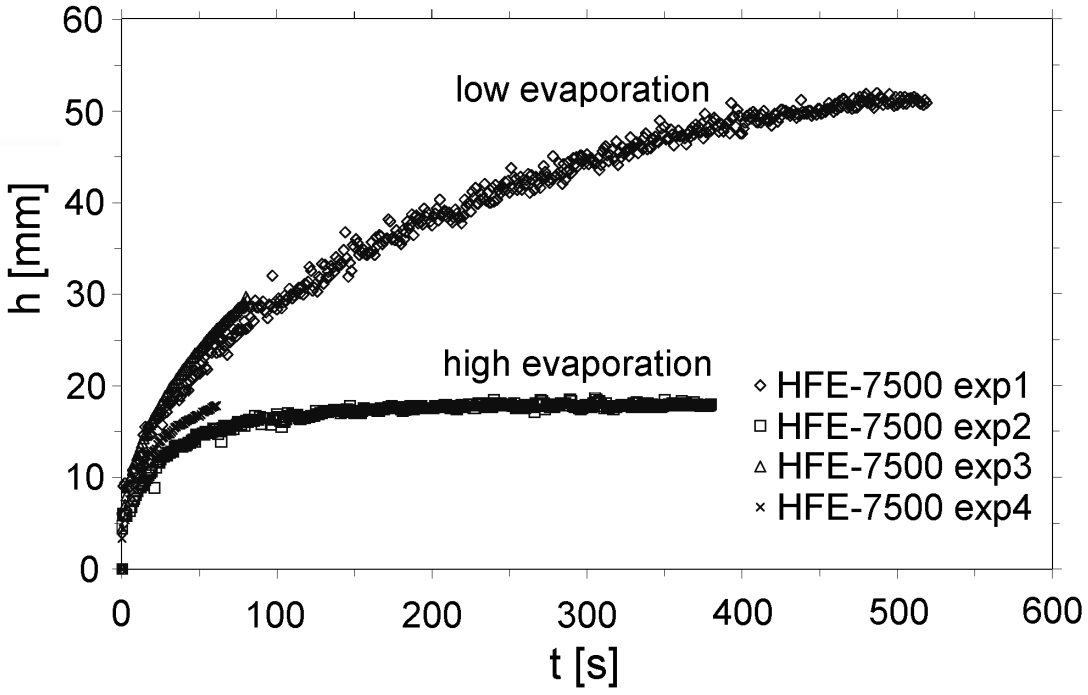


Figure 7.13: Height calculated from mass recordings of HFE-7500 wicking into the weave. The evaporation rate affects the reached height significantly. See Table 7.11 for further details.

trapped at this drying stage due to capillary forces. The effective evaporation rate which is of interest to understand the capillary rise under the effect of evaporation is the linear part. It is assumed that the weave, once the wicking front has passed, is completely saturated and thus refers to this evaporation regime. As already mentioned by Symons [98], the wicking of a liquid into a weave can be effected by evaporation or local heat sources. In this study no external heat sources were applied. However, the experimental setup allowed to investigate the influence of different evaporation rates on the capillary rise in warp direction. The evaporation occurs due to the vapor pressure of the test liquids that leads to a layer of vapor over the weave surface. Due to diffusion and convection the vapor is distributed in the surrounding air so that more liquid can evaporate. It is assumed, since only relatively small amounts of liquid evaporate, that the enthalpy of evaporation can be neglected when compared to the heat capacity of the saturated weave and heat conduction from the gaseous species. Thus the structure is assumed to be at constant temperature. As the weave is basically a two dimensional medium its outer surface is large compared to its volume which transports the liquid internally. Thus, although the evaporated amount of liquid may be comparably small, the effect of evaporation on the rise process may be large. In Fig. 7.13 the different wicking heights of the test liquid HFE-7500

are presented. The influence of evaporation is clearly visible. The experiments were either performed by Odic, Kaya [52] or the author.
Knowing about the strong effect of evaporation it is of interest to develop a model capable of explaining the process and allowing to predict the deviations from unaffected capillary rise.

## 7.4 Applicable equations (evaporation)

While the liquid rises in the metal weave it is exposed to the ambient atmosphere at the outer pores. If the surrounding gas is not saturated with the vapor of the liquid, evaporation out of these pores can occur. Due to the continuous loss of liquid due to evaporation the advance of the liquid front line will be slower than in a setup without evaporation. In this chapter the theoretical model given by Symons [98] is extended, which can then be used to explain the experimental findings. For the model presented below the assumption has been made that the evaporation is uniformly distributed and is given by the area normalized evaporation rate $\dot{m}_e$ [kg/m$^2$ s]. The evaporation rate is assumed to be constant $\dot{m}_e = const. \neq f(h, z)$. This assumption is valid if no point heat sources are affecting the local evaporation and if the transport of the gaseous (evaporated) species away from the weave is not restricted by the build up of a boundary layer (constant concentration gradient). Finally, the total evaporation mass flow $\dot{M}_e$ is given by Eq. (7.11) as stated in the previous chapter. Fig. 7.14 displays the integral and differential mass balance of the weave. It can be seen that the total mass inflow $\dot{M}(z = 0)$ is made up of two components - the mass flow necessary to supply the movement of the liquid front $\dot{M}_{\dot{h}}$ and the total evaporation mass flow $\dot{M}_e$. $\dot{M}_{\dot{h}}$ is given by

$$\dot{M}_{\dot{h}} = \phi A_b \rho \dot{h}. \tag{7.12}$$

Here, $\phi A_b$ refers to the effective bottom area of the weave. Regarding Fig. 7.14, the differential mass balance can be expressed as

$$d\dot{M}(z) = \dot{M}(z + dz) - \dot{M}(z) = -\dot{m}_e P_b dz. \tag{7.13}$$

When integrating and using the boundary condition that the total mass inflow at $z = 0$ must be equal to $\dot{M}_{\dot{h}} + \dot{M}_e$, one obtains

$$\dot{M}(z) = \dot{M}_{\dot{h}} + \dot{m}_e P_b h \left(1 - \frac{z}{h}\right). \tag{7.14}$$

The local mass flow $\dot{M}(z)$ can now be given in form of a flow velocity which is then used to calculate the viscous pressure loss. The flow velocity in the weave is composed of two parts. The

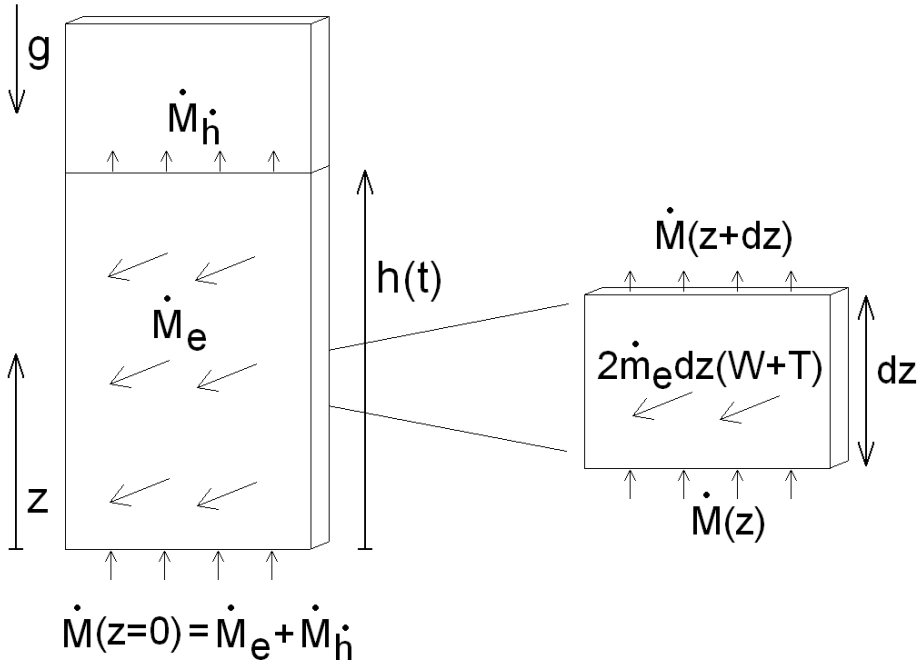


Figure 7.14: Schematic drawing displaying the mass balance of a wicking process with evaporation.

first part corresponds to the liquid front velocity $\dot{h}$, which is constant over the weave height as is $\dot{M}_{\dot{h}}$. The second is the refill velocity $v_r$ to refill the evaporated liquid, which is height dependent. Where the weave is in contact with the liquid surface ($z = 0$) the refill velocity reaches its maximum value of

$$v_{r,0} = \frac{\dot{M}_e}{\rho \phi A_b} = \frac{\dot{m}_e P_b h}{\rho \phi A_b}. \tag{7.15}$$

The assumption of a constant evaporation rate at the outer weave surface leads to a linear dependence of the refill velocity (see Eq. (7.14)) reading

$$v_r(z) = v_{r,0} \left(1 - \frac{z}{h}\right), \tag{7.16}$$

thus it can be seen that $v_r$ linearly reduces to zero at the actual height $h(t)$. Fig. 7.15 displays the velocity distribution of the liquid inside the weave. The total velocity, made up by the front line movement and the refill velocity can be given as

$$v_t(z) = \dot{h} + v_r(z). \tag{7.17}$$

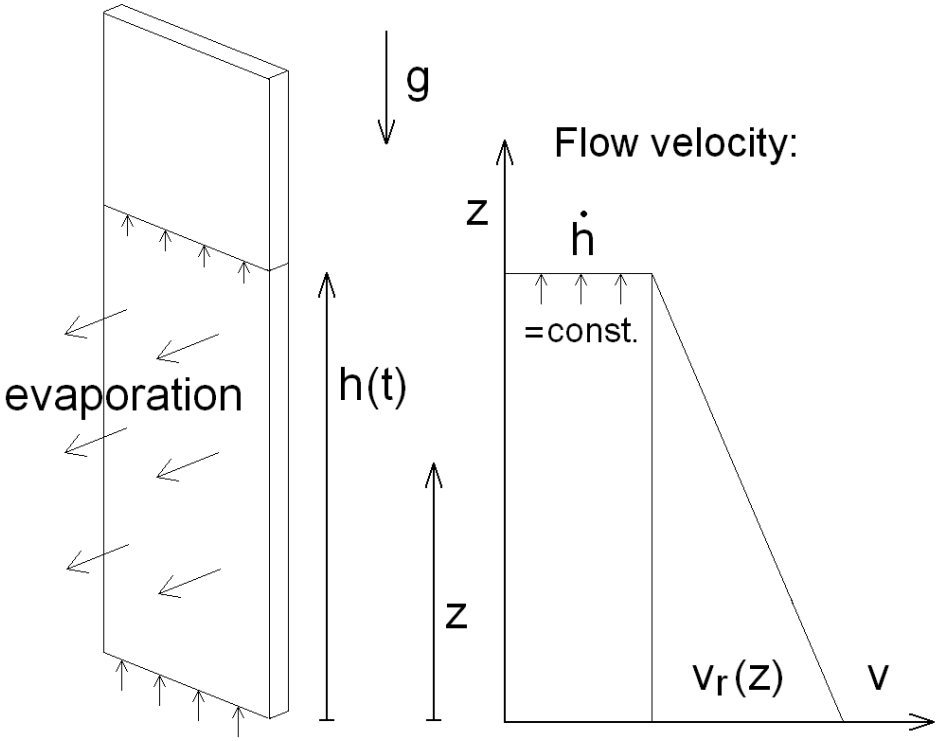


Figure 7.15: Velocities involved in a wicking process with evaporation. The total velocity consists of two components: a velocity $\dot{h}$ (constant over $z$, not constant over $t$) and a refill velocity $v_r$ which depends on the height $z$ and $t$.

The momentum balance for the case without evaporation is given in Eq. (2.49) as

$$-\rho\frac{d(h\dot{h})}{dt} = -\frac{2\sigma\cos(\theta)}{R_s} + \frac{\phi\mu h}{K}\dot{h} + \rho g h. \tag{7.18}$$

As the investigated process is a fairly slow one, inertia can be neglected, however, one has to take into account that the flow velocity in the wetted weave does not remain constant over height. Thus the viscous term (Darcy law) has to be modified to read

$$\frac{\phi}{K}\mu\int_0^h v_t(z)\,dz = \frac{\phi}{K}\mu h\left(\frac{v_{r,0}}{2} + \dot{h}\right). \tag{7.19}$$

Thus, including the effect of evaporation, the final differential equation becomes

$$\frac{2\sigma\cos(\theta_s)}{R_s} = \rho g h + \frac{\phi}{K}\mu h\dot{h} + \frac{\dot{m}_e}{2}\frac{P_b}{A_b}\frac{\mu}{\rho K}h^2. \tag{7.20}$$

Comparing this equation to the momentum balance for porous media without evaporation (e.g. Eq. (2.49)) shows that Eq. (7.20) neglects the local and convective acceleration terms, however,

a term is added to the right hand side which takes into account the losses due to evaporation. This equation can be transformed to the following form

$$\dot{h} = \frac{1}{bh} - \frac{c}{b} - \gamma h, \tag{7.21}$$

which equals Eq. (5.8) with an additional term for the losses due to evaporation. The coefficients $b$ and $c$ as previously defined are used, where $\gamma$ (representing the evaporation term) is defined as

$$\gamma = \frac{\dot{m}_e(w+T)}{\rho w T \phi}. \tag{7.22}$$

Setting $\dot{h} = 0$ in Eq. (7.21) one finds maximum (equilibrium) heights for the following different cases: i) No evaporation occurs ($\gamma = 0$) and only gravity restricts the maximum reachable height, given by

$$h_{eq,b,c} = \frac{1}{c}. \tag{7.23}$$

ii) No gravity ($c = 0$) is affecting the liquid rise, however evaporation has an effect resulting in

$$h_{eq,b,\gamma} = \sqrt{\frac{1}{b\,\gamma}}. \tag{7.24}$$

iii) Both terms (gravity and evaporation) have to be considered leading to

$$h_{eq,b,c,\gamma} = \frac{-c}{2b\,\gamma} + \sqrt{\frac{c^2}{4b^2\gamma^2} + \frac{1}{b\,\gamma}}. \tag{7.25}$$

iv) Finally no gravity and no evaporation restrict the capillary rise, hence there is no limit in the maximum reachable height, as is also predicted by the Lucas-Washburn equation.

## 7.5 Analytical solution

Starting from Eq. (7.21) one can derive an analytical expression for the time needed to reach a certain height of the liquid front $t(h)$, accounting also for evaporation and gravity. Rewriting Eq. (7.21) gives

$$\int \frac{bh}{-b\,\gamma h^2 - ch + 1} dh = \int 1 dt. \tag{7.26}$$

The solution to the first integral is given by Bronstein and Semendjajew [13] using the following definition

$$\Psi = -\frac{4\gamma}{b} - \frac{c^2}{b^2}. \tag{7.27}$$

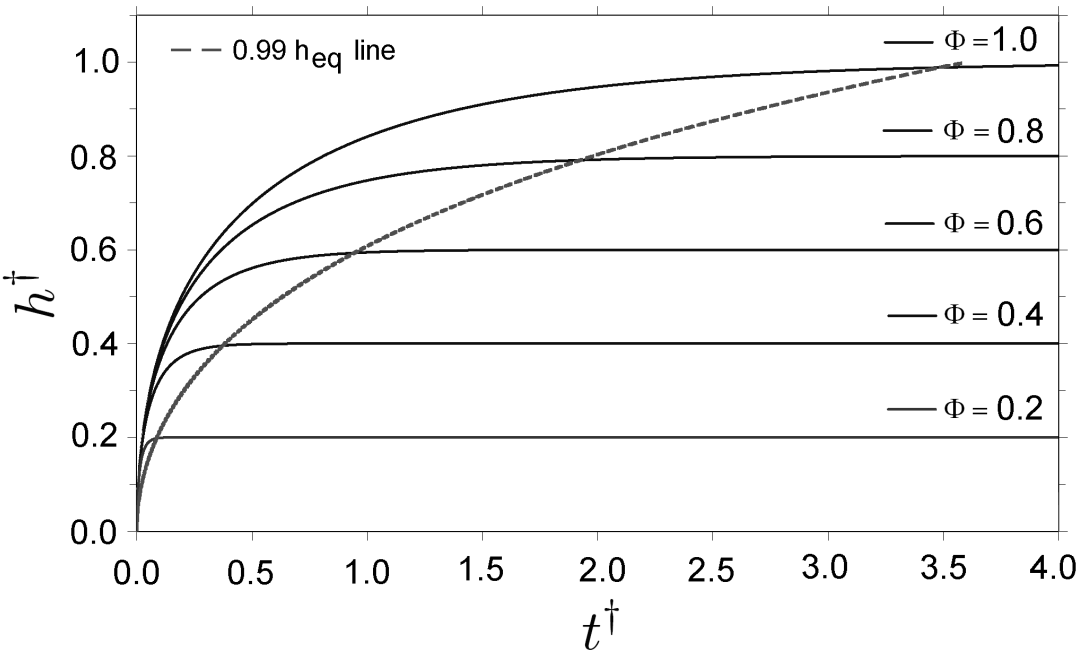


Figure 7.16: Dimensionless height over time for different values of $\Phi$. The 0.99 $h_{eq}$ line is introduced in the next section.

For $\Psi < 0$ the total solution in terms of $t = t(h)$ is

$$t = \frac{-1}{2\gamma} \ln\left(-\gamma h^2 - \frac{c}{b}h + \frac{1}{b}\right) - \frac{c}{2b\,\gamma\sqrt{-\Psi}} \cdot \ln\left(\frac{-2b\,\gamma h - c - b\sqrt{-\Psi}}{-2b\,\gamma h - c + b\sqrt{-\Psi}}\right) + C. \tag{7.28}$$

To calculate the unknown constant $C$, the initial condition $h(t \to 0) = 0$ can be used to give

$$C = \frac{1}{2\gamma} \ln\left(\frac{1}{b}\right) + \frac{c}{2b\,\gamma\sqrt{-\Psi}} \ln\left(\frac{-c - b\sqrt{-\Psi}}{-c + b\sqrt{-\Psi}}\right). \tag{7.29}$$

Thus the final solution is

$$t = \frac{1}{2\gamma}\left[-\ln\left(-b\gamma h^2 - ch + 1\right)\right] - \frac{c}{2b\,\gamma\sqrt{-\Psi}} \cdot \ln\left[\frac{(-2b\,\gamma h - c - b\sqrt{-\Psi})(-c + b\sqrt{-\Psi})}{(-2b\,\gamma h - c + b\sqrt{-\Psi})(-c - b\sqrt{-\Psi})}\right]. \tag{7.30}$$

### 7.5.1 Dimensional analysis

To compare the experimental data obtained with different fluids or under different conditions it is of great interest to have a set of dimensionless numbers to describe the problem. The

method presented in chapter 3 is used, and by applying the scaling using viscous effects and gravity as scaling forces gives $h^\dagger$ and $t^\dagger$ (see section 3.2.1, Eqs. (3.8) and (3.9))

$$h^\dagger = ch = \frac{\rho g h R_s}{2\sigma\cos(\theta)}, \tag{7.31}$$

and

$$t^\dagger = \frac{c^2 t}{b} = \frac{\rho^2 g^2}{2\mu\sigma\cos(\theta)}\frac{K R_s}{\phi}t. \tag{7.32}$$

However, $h^\dagger$ and $t^\dagger$ are not able to reflect the influence of evaporation on the wicking behavior. This can be done by relating the maximum reachable height with gravity and evaporation (Eq. (7.25)) to the maximum reachable height without evaporation (Eq. (7.23)). Using this approach a dimensionless "related maximum height" $\Phi$ is obtained

$$\Phi = \frac{h_{eq,b,c,\gamma}}{h_{eq,b,c}} = c\left(\frac{-c}{2b\,\gamma} + \sqrt{\frac{c^2}{4b^2\gamma^2} + \frac{1}{b\gamma}}\right). \tag{7.33}$$

If $\Phi$ is equal to zero no height is gained at all, the evaporation effect is so strong that it prevents any capillary rise ($\dot{m}_e \to \infty$). If $\Phi$ is equal to one, no evaporation occurs to restrict the capillary rise ($\dot{m}_e = 0$). For values of $\Phi$ in between, say 0.5, evaporation diminishes the reachable height to half the value that could be gained without evaporation.

With these parameters one can draw a dimensionless plot of the numerical solutions of Eq. (7.20) as shown in Figs. 7.16 and 7.17. The numerical solution of Eq. (7.20) is consistent with the analytical one (Eq. (7.30)).

### 7.5.2 Time needed to reach 0.99 $h_{eq}$

For infinite times the gained height converges to a maximum value $h_{eq}$. From Figs. 7.16 and 7.17 it can be seen that after a certain time depending on the evaporation rate, the height reaches a quasi steady state where no further increase in height occurs. For high evaporation rates (low values of $\Phi$) this state is reached earlier than for low evaporation rates (high values of $\Phi$). This raises the question at what time the liquid stops rising and reaches 0.99 times its equilibrium value $h_{eq}$. Using numerical methods, namely a tool written in C++, the dimensionless time $t^\dagger_{0.99}$ is found. It is defined as that time when 99% of the final height $h_{eq}$ is reached. $t^\dagger_{0.99}$ depends on the parameter $\Phi$ as can also be seen in Figs. 7.16 and 7.17. A polynomial function of fourth order is fitted to the numerically generated points which gives

$$t^\dagger_{0.99} = 1.2682\Phi^4 + 0.2157\Phi^3 + 2.122\Phi^2 - 0.0102\Phi. \tag{7.34}$$

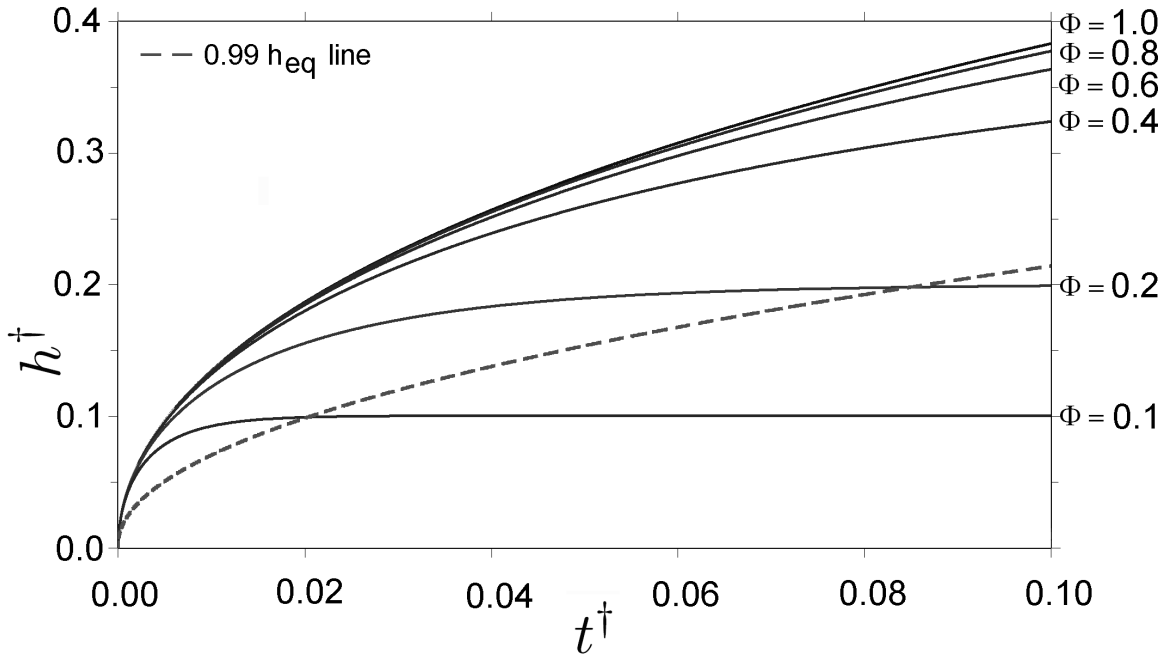


Figure 7.17: Close up of the solution displayed in Fig. 7.16 for shorter times.

The "0.99 $h_{eq}$ line" in Figs. 7.16 and 7.17 refers to the inverted value $\Phi_{0.99}(t^\dagger_{0.99})$ assuming that $\Phi$ is equal to $h^\dagger$ when 99% of it is reached. Another interpretation of the steady state line is as follows: If a liquid inside the weave is on the left hand side of the 0.99 $h_{eq}$ line in the diagram, it is still rising. If it is on the right hand of the line, it has already reached its final height $h_{eq}$ and remains static.

### 7.5.3 Evaluation of the model with experimental data (DTW)

In this section the evaporation model introduced on the previous pages shall be compared to the experimental results obtained with the Dutch-Twilled-Weave 200x1400. The experiments were either performed by Odic, Kaya [52] or the author. Figs. 7.18 and 7.19 show a comparison of experimental results and predicted values obtained with the presented model. Here the experiments are abbreviated by the liquid used and numbers as explained in Table 7.11.
Figs. 7.18 and 7.19 show that in general the experimental results qualitatively follow the predicted values. However, there seems to be a trend that the mathematical model overestimates the height. Table 7.12 displays the measured and predicted values of $\Phi$ (Eq. (7.33)) to compare the deviation between model and experiment. Apparently the calculated values are larger than the measured ones as was seen from the comparison of the height curves. The average deviation is found to be in the range of 20%. There are several parameters which could be the source of

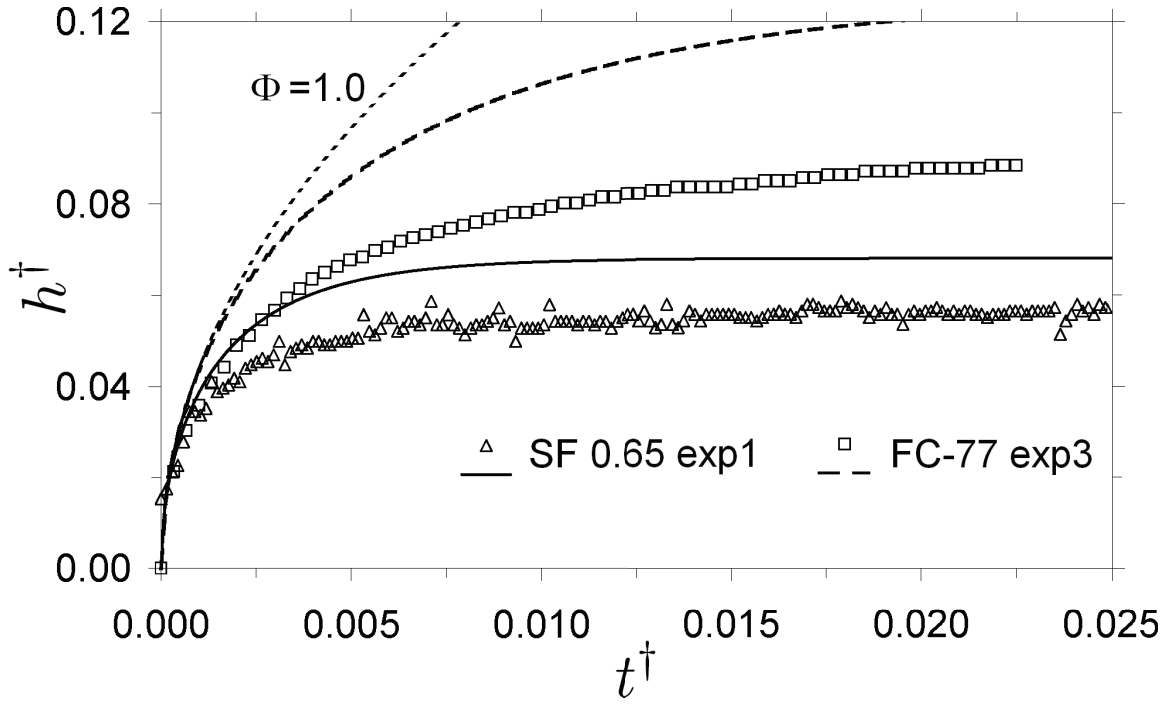


Figure 7.18: Dimensionless plot (small $t^\dagger$) of experimental results (symbols) in comparison to the values predicted by the model (lines). The $\Phi = 1$ line depicts the rise for both liquids with no evaporation. See Table 7.11 for further details.

these deviations. A high influence can be assigned to the assumption of a constant evaporation distribution all over the wet weave. If by some means the evaporation rate would be higher at the top of the weave the refill velocity $v_r(z)$ would not be a linear function of $z$ and thus more liquid would have to be transported to the top. This would lead to a higher pressure loss and may thus explain the discrepancy between theory and experimental findings. As can be seen in Table 7.11 the measured values of $\dot{m}_e$ also deviate for similar chamber apertures and test liquids. Though the deviation is not found to be in the range of some orders of magnitude, it still shows that the experimental environment (e.g. convection) is not fully reproducible and understood. Also the different levels of saturation are not considered in the presented model, and the exact determination of the local evaporation rate and the effective evaporation surface is not possible. In addition the contact angle is assumed to be constant and inertial forces (local acceleration and convective) are neglected. This, however, should only be of importance for the very early stages of the capillary rise. Despite the deviations the presented evaporation model gives a far better prediction for the capillary rise than solutions neglecting evaporation (e.g. Lucas-Washburn) and explains the experimental observations qualitatively. Also can be seen

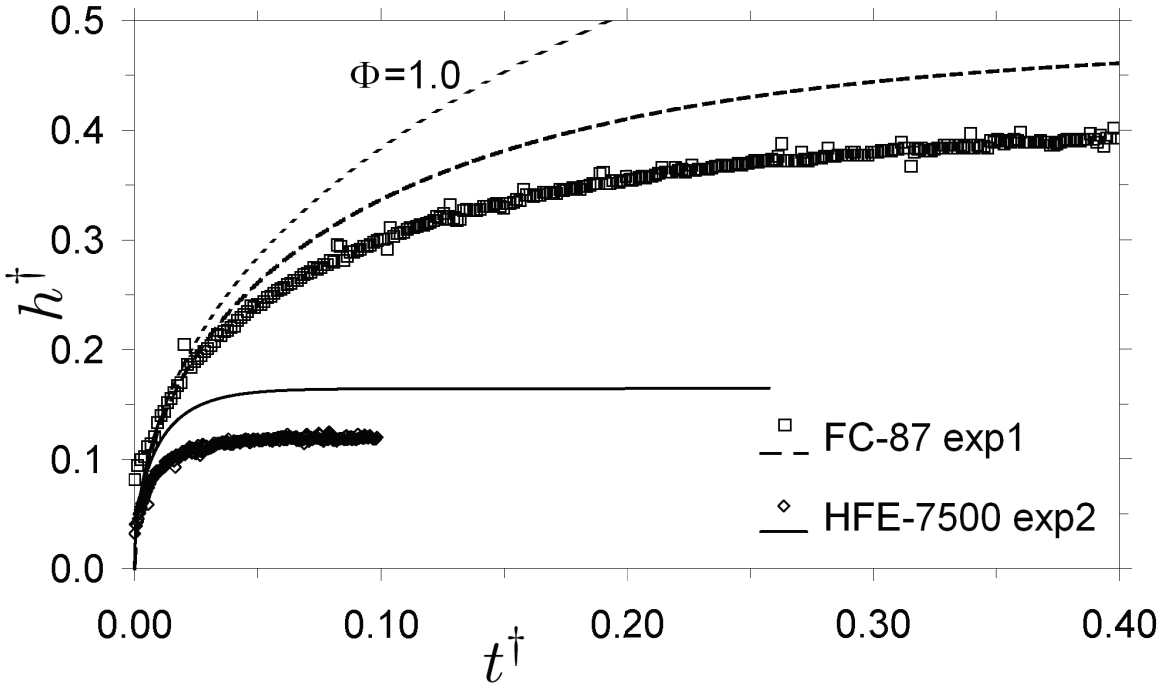


Figure 7.19: Dimensionless plot (large $t^\dagger$) of experimental results (symbols) compared to the analytical model (lines). See Table 7.11 for further details. The model tends to overestimate the height.

that realistic evaporation rates may have a major impact on the reachable wicking height. For example the last experiment shown in Table 7.12 (SF 0.65 exp1) has a measured $\Phi$ of about 0.06. This means the liquid reaches only 6% of the height that would be gained without evaporation!

Table 7.11: Experiments performed using various test liquids.

| | specimen width $w$ [mm] | chamber aperture [mm$^2$] | $\dot{m}_e$ (measured) [kg/m$^2$s] | $\Phi_{calc.}$ [-] |
|---|---|---|---|---|
| SF 0.65 exp1 | 16 | 2500 | $7.40 \times 10^{-4}$ | 0.071 |
| SF 0.65 exp2 | 18 | 55 | $4.68 \times 10^{-6}$ | 0.593 |
| SF 0.65 exp3 | 18 | 2500 | $6.58 \times 10^{-4}$ | 0.075 |
| HFE-7500 exp1 | 16 | 55 | $7.10 \times 10^{-6}$ | 0.740 |
| HFE-7500 exp2 | 16 | 2500 | $4.36 \times 10^{-4}$ | 0.169 |
| HFE-7500 exp3 | 18 | 55 | $1.81 \times 10^{-6}$ | 0.902 |
| HFE-7500 exp4 | 18 | 2500 | $4.68 \times 10^{-4}$ | 0.164 |
| FC-77 exp1 | 16 | 2500 | $2.01 \times 10^{-3}$ | 0.098 |
| FC-77 exp2 | 18 | 55 | $4.54 \times 10^{-6}$ | 0.847 |
| FC-77 exp3 | 18 | 2500 | $1.21 \times 10^{-3}$ | 0.124 |
| FC-72 exp1 | 16 | 55 | $7.52 \times 10^{-5}$ | 0.529 |
| FC-87 exp1 | 16 | 55 | $1.66 \times 10^{-4}$ | 0.494 |

Table 7.12: Experimental values of $\Phi$ compared to calculated ones.

| | $\Phi_{exp.}$ | $\Phi_{calc.}$ | $\Phi_{exp.}/\Phi_{calc.}$ |
|---|---|---|---|
| SF 0.65 exp1 | 0.057 | 0.071 | 80.3 % |
| HFE-7500 exp2 | 0.12 | 0.169 | 71.0 % |
| FC-77 exp1 | 0.059 | 0.098 | 60.2 % |
| FC-72 exp1 | 0.43 | 0.529 | 81.3 % |
| FC-87 exp1 | 0.40 | 0.494 | 80.9 % |
| average | - | - | 74.7 % |

## 7.6 Conclusion

The wicking behavior of perfectly wetting liquids in metallic weaves is studied. By means of the momentum balance the Lucas-Washburn equation and further analytical solutions are introduced. An experimental setup using a vertically positioned weave is used to investigate the wicking behavior of different liquids. The results are compared to analytical solutions and good agreement between the Lucas-Washburn equation and the experimental data is found for flow regimes where gravity and evaporation effects are negligible. From the measurements one can determine the permeability and static radius (for the capillary pressure) of the structure. No significant influence of the screen width onto the wicking process is found. However, the capillary rise in warp direction occurs about twice as fast as in weft direction as the permeabilities also differ by about this factor due to the different thicknesses of the wires and the weave structure. The results for the slope parameter $K/R_s$ are validated by previous literature, but there are discrepancies for the static radius which may occur due to the sensitivity of the experiment to evaporation. Therefore the effect of evaporation is investigated in more detail and a model is developed to explain the observed effects. An analytical solution is presented which includes both gravitational and evaporation effects in dimensionless form. Using the introduced dimensionless parameters it is possible to plot all experimental data in a single diagram to compare different fluids and evaporation rates. The experimental data supports the theoretical model, although it shows that the model tends to overestimate the reached height by about 20%.

Future investigations on this topic call for an experimental environment with variable but known ambient conditions to provide better insight into the effect of evaporation, but also to understand the impact of convection. By comparing microscopic and macroscopic numerical simulations (CFD) of two-species, two-phase systems to the obtained experimental data the models can be validated. This is one of the proposed aims for the next generation of projects within the framework of the Research Training Group PoreNet.

# Chapter 8

# Radial capillary transport

## Note on the following chapter

The following chapter is based on the joint publication "Radial capillary transport from an infinite reservoir" by M. Conrath, N. Fries, M. Zhang and M.E. Dreyer [21]. The analytical derivation and the dimensional analysis has been conducted by N. Fries while the experiments and the data analysis has been realized by the coauthors. Still the experimental data will be presented in the following chapter, as it provides a very useful validation of the theoretical considerations. Furthermore, the author likes to express his thanks to his colleagues for the fruitful cooperation and the interesting discussions.

## 8.1 Applicable equations

In this chapter a theoretical and experimental study on liquid wicking radially within a porous filter paper from an (assumed) infinite reservoir is presented. The theoretical model predicts both outward and inward radial transport and is based on Darcy's law. Nevertheless, the resulting solution for the position of the wetting front bears a strong resemblance to the radial capillary solution by Marmur [64]. The experiments are conducted with filter paper to ensure good observability and to avoid the displacement problem. With the setup described here one can examine horizontal wicking i) radially outward, and ii) linear. Using a second setup already described in the previous chapter iii) vertical linear wicking by mass method is added. All results are compared and discussed.

For the theoretical considerations two basic assumptions are made: isotropic pore distribution and absence of evaporation. An isotropic pore distribution ensures a purely circular wicking

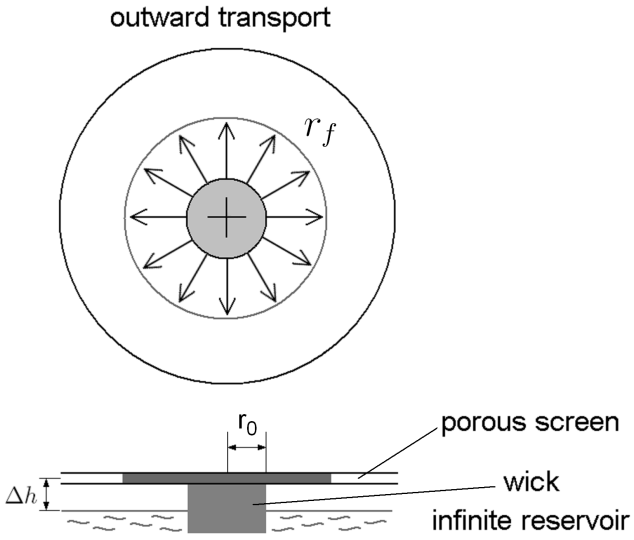


Figure 8.1: Experiment configuration and lengths for outward capillary transport.

front line. Evaporation is superimposed to the underlying mechanism of capillary transport and therefore would complicate the basic understanding. That is why it is excluded here by using a nonvolatile test liquid.

The configuration considering an outward capillary transport fed by a circular wick in the center - as illustrated in Fig. 8.1 - is investigated.

When liquid wicks within a porous material there is a driving capillary pressure along the meniscus at the edge of the spreading spot. It has to balance the viscous pressure loss inside the material itself, the viscous pressure loss in the feeding device and the inertial pressure. In this section the influence of the wick is neglected as its permeability was chosen to be much higher than the permeability of the filter paper. Hence - as introduced in the theoretical chapter of this work (Eq. (2.60)) - the momentum balance for radial capillary flow through porous structures reads as

$$\underbrace{\frac{2\sigma\cos(\theta)}{R_s}}_{surface\ tension} = \underbrace{\mu\frac{\phi}{K}\int_{r_0}^{r_f} v_r(r)dr}_{viscosity} + \underbrace{\frac{d}{dt}\left[\int_{r_0}^{r_f}\rho v_r(r)dr\right]}_{inertia} + \underbrace{\int_{v_0}^{v_f}\rho v_r dv_r}_{convective}. \tag{8.1}$$

Due to the mass balance Eq. (2.53)

$$v_r(r) = \frac{1}{r} r_f \dot{r_f}, \tag{8.2}$$

so one can substitute $v_r(r)$ and rearrange to obtain

$$1 - \underbrace{\frac{\mu\phi R_s}{2\sigma\cos(\theta)K}}_{b} r_f \frac{dr_f}{dt}\ln\left(\frac{r_f}{r_0}\right) - \underbrace{\frac{\rho R_s}{2\sigma\cos(\theta)}}_{a}\left(\frac{d}{dt}\left[r_f\frac{dr_f}{dt}\ln\left(\frac{r_f}{r_0}\right)\right] + \left(\frac{dr_f}{dt}\right)^2\left[\frac{1}{2} - \frac{r_f^2}{2r_0^2}\right]\right) = 0. \tag{8.3}$$

To ease the handling of the following calculations the previously introduced parameters $a$ and $b$ are used. Note that these parameters are differently defined in [21]. Applying the Buckingham $\pi$-Theorem, see [17] and [107], with the five (5) dimensional units $a[\mathrm{s}^2\,\mathrm{m}^{-2}]$, $b[\mathrm{s}\,\mathrm{m}^{-2}]$, $r_f[\mathrm{m}]$, $t[\mathrm{s}]$, $r_0[\mathrm{m}]$ and the two (2) fundamental units time [s] and length [m] one obtains $5-2=3$ dimensionless $\pi$ parameters that characterize the problem. Thus the Buckingham $\pi$ theorem provides us with three dimensionless scalings. First one has a dimensionless radius

$$\pi_1 = r_f^\star = \frac{r_f}{r_0}, \tag{8.4}$$

which is an aspect ratio. The second scaling is a dimensionless time

$$\pi_2 = t^\star = \frac{4}{br_0^2}t = \frac{8\sigma\cos(\theta)}{\mu r_0^2}\frac{K}{\phi R_s}t \sim \frac{1}{\mathrm{Ca}(t)}. \tag{8.5}$$

Here Ca denotes the capillary number - relating viscous forces to surface tension forces - which is given by

$$\mathrm{Ca} \sim \frac{\mu r_0}{\sigma t}. \tag{8.6}$$

Since a transient phenomenon is investigated, the capillary number is time-dependent. Eq. (8.5) also provides a characteristic time

$$t_c = \frac{t}{t^\star} = \frac{br_0^2}{4} = \frac{\mu r_0^2}{8\sigma\cos(\theta)}\frac{\phi R_s}{K}. \tag{8.7}$$

The third dimensionless parameter reads

$$\pi_3 = \frac{b^2}{a}r_0^2 = \frac{\mu^2 r_0^2}{2\sigma\cos(\theta)\rho}\frac{\phi^2 R_s}{K^2} \sim \mathrm{Oh}^2. \tag{8.8}$$

This parameter is useful for scaling the inertia term, Oh denotes the Ohnesorge number - relating viscous forces to surface tension and inertial forces

$$\mathrm{Oh} = \frac{\mu}{\sqrt{\sigma\rho L}}. \tag{8.9}$$

Using $r_f^\star$, $t^\star$ and $\pi_3$ in the momentum equation Eq. (8.3) gives the problem in a dimensionless form

$$\frac{1}{4} - r_f^\star\frac{dr_f^\star}{dt^\star}\ln\left(r_f^\star\right) - \frac{4}{\pi_3}\left(\frac{d}{dt^\star}\left[r_f^\star\frac{dr_f^\star}{dt^\star}\ln\left(r_f^\star\right)\right] + \left(\frac{dr_f^\star}{dt^\star}\right)^2\left[\frac{1-(r_f^\star)^2}{2}\right]\right) = 0. \tag{8.10}$$

As will be shown later in Table 8.8, in the experiments $\pi_3 \gg 1$ (or $\mathrm{Oh} \gg 1$, respectively), and therefore the inertial term can be neglected. Thus one seeks an analytical solution of the dimensionless equation

$$\frac{1}{4} - r_f^\star\frac{dr_f^\star}{dt^\star}\ln r_f^\star = 0. \tag{8.11}$$

To find it the method of separating the variables is used to obtain

$$r_f^{\star 2}(\ln r_f^{\star 2} - 1) = t^\star + C. \tag{8.12}$$

Assuming that the spot has the initial radius $r_0$ at the time $t = 0$, the boundary condition to find $C$ reads as

$$r_f^\star(t^\star = 0) = 1, \tag{8.13}$$

giving a special solution in terms of $t^\star(r_f^\star)$, namely

$$t^\star(r_f^\star) = r_f^{\star 2}\left(\ln r_f^{\star 2} + \frac{1}{r_f^{\star 2}} - 1\right). \tag{8.14}$$

A solution in terms of $r_f^\star(t^\star)$ can be obtained with the Lambert W function. It is defined as the inverse of $y = xe^x$ where $x = W(y)$. In a first step Eq. (8.14) is rearranged to

$$t^\star - 1 = r_f^{\star 2}(\ln r_f^{\star 2} - 1). \tag{8.15}$$

Since $1 = \ln e$ and the inversion $y = x \ln x \leftrightarrow x = y/W(y)$ applies, one finds that

$$\frac{r_f^{\star 2}}{e} = \frac{e^{-1}\,(t^\star - 1)}{W\left(e^{-1}\,(t^\star - 1)\right)}. \tag{8.16}$$

This equation is quadratic. Therefore, two different solutions $r_f^\star(t^\star)$ are possible. These are

$$r_f^\star(t^\star) = \pm\sqrt{\frac{t^\star - 1}{W\left(e^{-1}(t^\star - 1)\right)}}. \tag{8.17}$$

Due to its unphysical nature, the "-" solution is omitted. The Lambert W function is well explained in [22]. One of its properties is that it is generally complex. There are only two branches with real values which are shown in Fig. 8.2. These branches are denoted $W(0, x)$ and $W(-1, x)$, respectively. In light of this fact, the analytical solutions according to Eq. (8.17) become

$$r_f^\star(t^\star) = \sqrt{\frac{t^\star - 1}{W\left(0, e^{-1}(t^\star - 1)\right)}} \quad \text{outward transport,} \quad 0 \le t^\star \le \infty \tag{8.18}$$

$$r_f^\star(t^\star) = \sqrt{\frac{t^\star - 1}{W\left(-1, e^{-1}(t^\star - 1)\right)}} \quad \text{inward transport,} \quad 0 \le t^\star \le 1 \tag{8.19}$$

These solutions are also depicted in Fig. 8.3.

The liquid flow rate that occurs in the porous medium is also of interest. It is important to

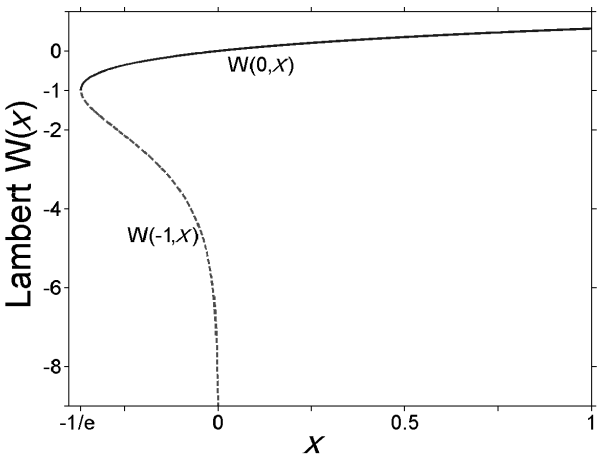


Figure 8.2: The two real-valued branches of the Lambert W function.

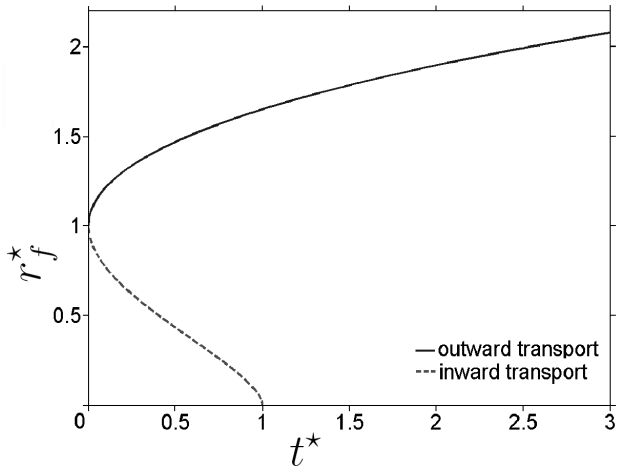


Figure 8.3: The analytical solutions for inward and outward capillary transport.

know because the model is idealized by neglecting the flow losses in the wick. As a consequence, the initial flow rate is infinite. In dimensional form, the flow rate is

$$\dot{V}(r_f, t) = \pm 2\pi T r_f \frac{dr_f}{dt}. \tag{8.20}$$

Introducing $r_f^\star$ and $t^\star$ one finds that

$$\dot{V}(r_f^\star, t^\star) = \pm \frac{8\pi T r_f^\star}{b} \frac{dr_f^\star}{dt^\star}. \tag{8.21}$$

Here, the plus sign applies for outward and the minus sign for inward transport. With $dt^\star/dr_f^\star = 2r_f^\star \ln r_f^{\star 2}$ one obtains

$$\dot{V} = \pm \frac{4\pi T}{b \ln r_f^{\star 2}}, \tag{8.22}$$

by setting $V_c = 4\pi T/b$ for the characteristic flow rate one finally arrives at

$$\dot{V}^\star = \frac{\dot{V}}{V_c} = \frac{1}{\ln r_f^{\star 2}}, \tag{8.23}$$

which is plotted in Figs. 8.4 and 8.5.

## 8.2 Experimental Apparatus

Parallel to the development of a mathematical model an experiment was built up as shown in Fig. 8.6 to investigate the radial outward wicking process. Here, an aluminum ring clamp

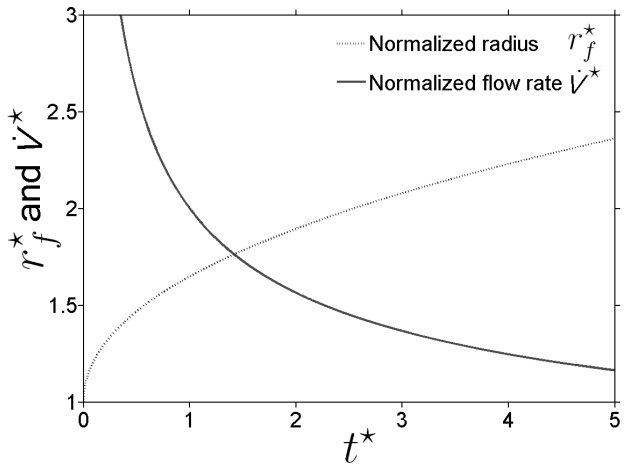


Figure 8.4: Flow rate in outward wicking.

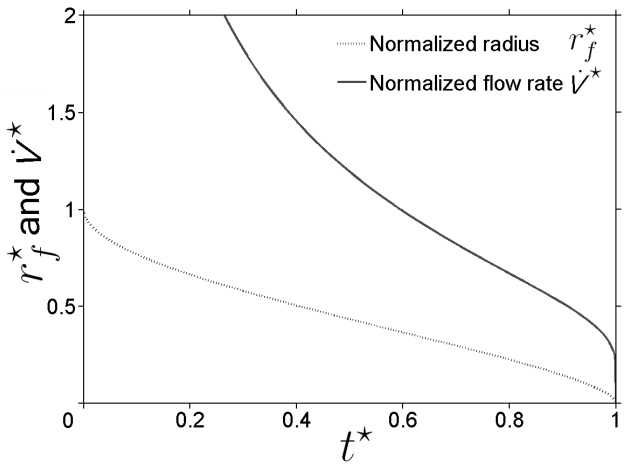


Figure 8.5: Flow rate in inward wicking.

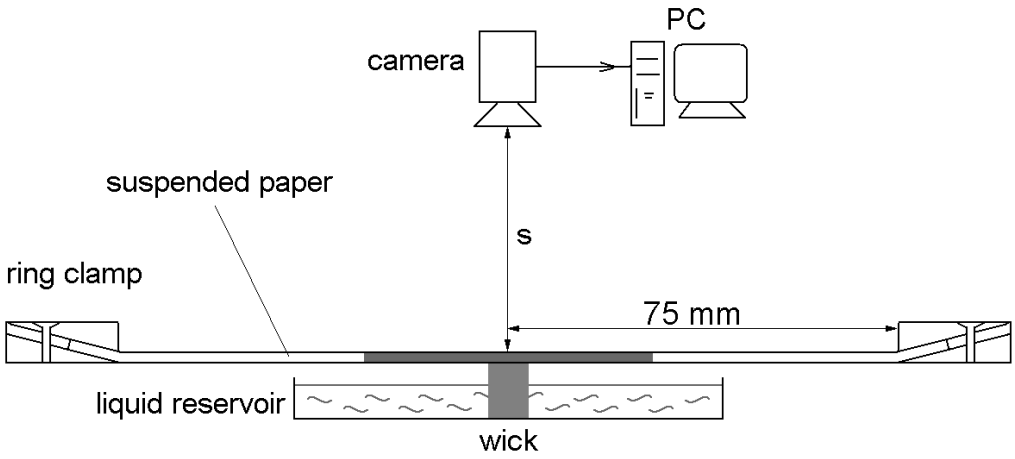


Figure 8.6: Schematics of the test setup. The distance $s$ between camera and the observed paper is about 10 times the paper diameter. The wick radius is $r_0$.

made of two parts that are joined together by screws allows to firmly suspend a filter paper. The ring clamp along with the paper is fixed horizontally, the usable paper radius being 75 mm. The height difference $\Delta h$ between paper and reservoir, see also Fig. 8.1, ranges from 5 to 8 millimeters. As porous materials four different kinds of filter paper whose properties according to the supplier are listed in Table 8.1 are used. All four papers are circular with a diameter of 185 mm and supplied by Omnilab (Bremen, Germany). While the first three papers consist of cellulose fibers that are porous itself (double porous) the fourth paper is made of borosilicate glass fibers. Paper is chosen for the experiments as it is disposable in a variety of parameters, easily purchased and most important it provides circular spots due to the isotropic fiber orientation, at least in a macroscopic point of view. The filtration time

in Table 8.1 is given by the suppliers using the Herzberg method[1]. These properties can be used to calculate the missing pore structure parameters $K$ and $\phi$ of the papers: using filtration time $t_{Hz}$ and paper thickness $d$, the permeability $K$ can be calculated with the relation $K = (Q\mu d)/(\Delta p A)$ where $Q = 100$ ml$/t_{Hz}$ is the flow rate, $\mu = 10^{-3}$ Pas the dynamic viscosity of water, $d$ the paper thickness, $\Delta p = 1000$ Pa the hydrostatic pressure of the water column and $A = 10$ cm$^2$ the filter area. The porosity $\phi$ is calculated by setting $\phi = (V_{total} - V_{solid})/V_{total}$ where $V_{total} = Ad$ and with the paper grammage $V_{solid} = m_{paper}/\rho_{solid}$, for the densities $\rho_{solid}$ one sets $\rho_{solid}$(cellulose) $= 1.5$ g/cm$^3$ and $\rho_{solid}$(borosilicateglass) $= 2.23$ g/cm$^3$, respectively. In the last line of Table 8.1 the wicking constants $b$ are calculated. To do so $\cos\theta = 1$ has been assumed, and the liquid properties in Table 8.2 have been applied.

Table 8.1: Properties of the papers that were used for the experiments according to the data sheets of supplier and producers (Omnilab, Sartorius, Whatman). Here, $R_s$ is an average pore size (Sartorius) or a particle retention size (Whatman).

| | Sartorius 391 | Whatman 589/2 | Whatman 40 | Whatman GF/B |
|---|---|---|---|---|
| by suppliers: | | | | |
| thickness $d$ [mm] | 0.21 | 0.19 | 0.21 | 0.83 |
| grammage [g/m$^2$] | 84 | 85 | 95 | 141 |
| pore size $R_s$ [$\mu$m] | 10 | 2-6 | 4 | 0.5 |
| filtration $t_{Hz}$ [s] | 180 | 140 | 340 | not specified |
| calculated: | | | | |
| permeability $K$ [$\mu$m$^2$] | 0.117 | 0.136 | 0.062 | - |
| porosity $\phi$ | 0.733 | 0.702 | 0.698 | 0.924 |
| wicking c. $b$ [s/mm$^2$] | 7.508 | 1.236-3.717 | 5.394 | - |

The test liquid that wicks in the paper is silicon oil AK5 (supplier Wacker AG, Germany) that exhibits a negligible evaporation rate. Chemically, this is Dimethylpolysiloxane with the structure $(CH_3)_3\ Si - [O - Si(CH_3)_2]_n - O - Si(CH_3)_3$ with n being around 5 since it is a blend. Its properties according to the supplier are listed in Table 8.2.

As reservoir for the test liquid a flat cylinder-shaped glass dish with 80 mm diameter and 8 mm height is used. Contrary to the assumption this is a finite reservoir, however it can be

[1]Given by the supplier to be the time for 100 ml deaerated water to pass 10 cm$^2$ filter area at a constant height of the water column being 10 cm. Different definitions using a column of 5 cm also exist.

Table 8.2: Properties of AK5 silicone oil according to the product data sheet of the supplier (Wacker AG, Germany); no errors are provided.

| kinematic viscosity $\nu$ [mm$^2$/s] | dynamic viscosity $\mu$ [mPas] | density $\rho$ [kg/m$^3$] | surface tension $\sigma$ [mN/m] |
|---|---|---|---|
| 5 | 4.6 | 920 | 19.2 |

regarded as infinite since the amount of liquid needed to completely wet a thin paper causes no perceptible loss in its fill height. The liquid transport from the reservoir to the paper is enabled by different kinds of wicks. For the experiments on outward transport (see left-hand picture of Fig. 8.1) cylindrical wicks made of glass frits (Por.0, pore radius 80−125 $\mu$m, supplier Robu Glas, Hattert in Germany) are used. They feature an appearance that is similar to sandstone. Three glass frit wicks with radii $r_0$ of 2.05 mm, 2.5 mm and 10 mm are used. The radii of the outward wicks were checked with a sliding caliper giving an accuracy of $\pm$12.5 $\mu$m.

The liquid reservoir with the wick is placed on top of a small lifting jack. Therefore, to initiate contact, the jack is manually operated until the wick touches the paper and liquid is observed to spread. A digital camera is positioned about 150 cm above the paper to record the wicking process in the paper. The camera is a B/W-CCD video camera module (CM8, Intravision) with a resolution of 768 x 576 pixel and a Nikkor 24 mm lens that is linked to a personal computer. Screenshots are recorded every 10 s which gives several hundred or thousand images for the whole wicking process. These image series are processed by Matlab routines using the Canny-algorithm to detect the wicking front line, see Fig. 8.7. More precisely, the single frames are transformed into grey-scale matrices. All the pixels outside the observation radius are overwritten with an average grey-scale value of the dry area to avoid the detection of wrong edges. Now, the Canny method finds edges by looking for local maxima of the grey-scale gradient. This gradient is calculated using the derivative of a Gaussian filter. The method uses two thresholds, to detect strong and weak edges, and includes the weak edges in the output only if they are connected to strong edges. This method is therefore less likely than others to be fooled by noise, and more likely to detect true weak edges. As Fig. 8.7 demonstrates, the detected front lines are overlaid on the original images to check its accuracy. Because the detected front line must always be closed it can be filled to obtain a binary spot as shown in the last picture of Fig. 8.7. The amount of pixels contained in the binary spot gives the spot area $A_{spot}$, the average spot radius $r_f$ is found by setting $A_{spot} = \pi r_f^2$.

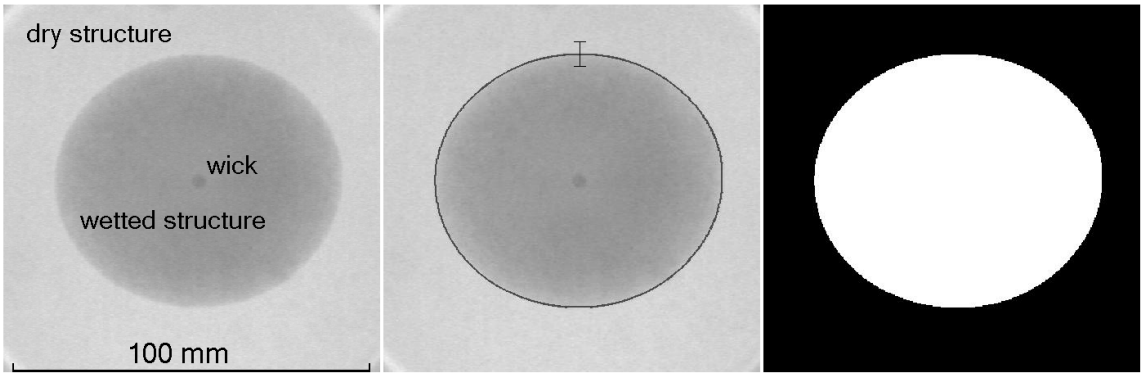


Figure 8.7: Evaluation with Matlab. Left picture: original. Center picture: detected wicking front line overlaid on the original. Right picture: binary spot.

**Error estimation** Errors in the measured data are expected due to the 1) inhomogeneity of the papers and the uncertanity in the liquid properties, 2) pixel resolution, 3) edge detection, 4) fluctuations of height difference $\Delta h$ between paper and reservoir, 5) wick radius $r_0$ and 7) contact conditions between wick and paper.

1. The magnitude of paper inhomogeneity is estimated by evaluating the azimuthal fluctuations in $r_f(t)$. It is found to be less than 10 % of the actual mean radius. In addition, the liquid properties presented in Table 8.2 include an error of unknown magnitude. For the following calculations it is assumed to be 5 %. Thus, for these two points an uncertainty of 15 % is assigned.

2. The recorded images of the wicking process have a resolution of 0.3 mm/pixel. Hence, the error due to limited resolution is about 0.15 mm.

3. Edges in cellulose paper (Sartorius 391, Whatman 589/2 and Whatman 40) are found to be rather sharp independent of the wetted spot size. Here, the greyscale value between wetted and dry area drops within 2 pixels which makes an accuracy of $\pm 0.3$ mm. In contrast, the spots in glass paper exhibit a diffuse edge that becomes even more diffuse as the spot size increases. Here, the edge detection has an accuracy of 15 %.

4. Fluctuations of the reservoir height lead to additional or decreased hydrostatic pressure that has to be balanced by the surface pressure at the meniscus. Using the liquid properties provided by Table 8.2, a one millimeter fluctuation of $\Delta h$ provides a pressure difference of 9.2 Pascal. Using the averaged pore or particle retention size of the papers as given by the suppliers, see Table 8.1 (and assuming that it is of same size order as

the wicking pores), one can estimate the capillary pressure $p_\sigma = 2\sigma/R_s \approx 4000$ Pascal. During the experiments, a maximum height fluctuation of below 5 mm occured which yields 1 % of the surface pressure. Hence, the expected error is $\pm 0.5$ %.

5. The wick radii for outward wicking are 2.05 $\mu$m, 2.5 $\mu$m and 10 $\mu$m with a tolerance of $\pm 12.5$ $\mu$m. With the theoretical solution, see Eq. (8.18), one can determine the impact of these tolerances. By setting $r_f^\star \rightarrow r_f^\star[1 \pm (tolerance/r_0)]^{-1}$ one finds the expected errors to depend on the wick size. They will be $+1.21/-1.23$ % for the 2.05 mm wick, $+1.01/-0.99$ % for the 2.5 mm wick and $\pm 0.25$ % for the 10 mm wick.

6. For the variations of the contact conditions between wick and paper no error has been assigned. Nevertheless, this issue is addressed in the "discussion" section.

An overview of the expected errors is provided by Table 8.3.

Table 8.3: Overview on the expected errors in the experiments.

| $r_0$ of wick | paper & liq. | pixel res. | edge d. | $\Delta h$ var. | $r_0$ var. | $\sum$ |
|---|---|---|---|---|---|---|
| cellulose p. | | | | | | |
| 2.05 mm | 15% | 0.15 mm | 0.3 mm | 0.5% | 1.22% | $\pm(16.72\% + 0.45$ mm) |
| 2.50 mm | 15% | 0.15 mm | 0.3 mm | 0.5% | 1.00% | $\pm(16.50\% + 0.45$ mm) |
| 10.0 mm | 15% | 0.15 mm | 0.3 mm | 0.5% | 0.25% | $\pm(15.75\% + 0.45$ mm) |
| glass p. | | | | | | |
| 2.05 mm | 15% | 0.15 mm | 15% | 0.5% | 1.22% | $\pm(31.72\% + 0.15$ mm) |
| 2.50 mm | 15% | 0.15 mm | 15% | 0.5% | 1.00% | $\pm(31.50\% + 0.15$ mm) |
| 10.0 mm | 15% | 0.15 mm | 15% | 0.5% | 0.25% | $\pm(30.75\% + 0.15$ mm) |

## 8.3 Results

The described setup was used to conduct experiments on horizontal i) linear and ii) radially outward transport. Moreover, reference data for iv) vertical linear transport were obtained in another setup that is described in [35]. The reference data from the two linear experiments (horizontal and vertical strip) provide us with a basis to predict the radial outward wicking process.

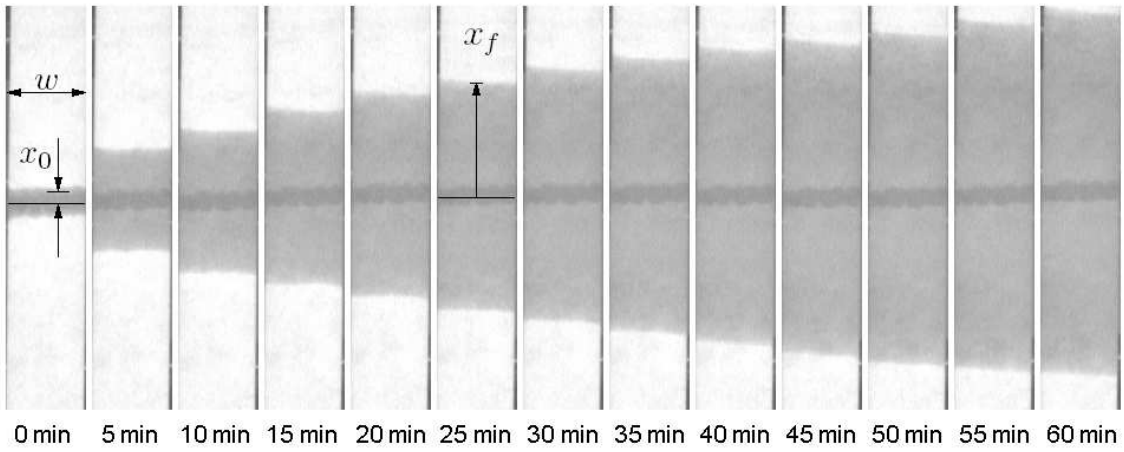


Figure 8.8: Evolution of the wetted area in horizontal wicking. The strip width is $w = 20$ mm, the initial distance $x_0 = \pm 3$ mm.

### 8.3.1 Reference measurement - linear transport

**Wicking into a horizontal strip** From a theoretical point of view, capillary transport in a horizontal strip is the most simple compared to other arrangements because it is linear and independent of gravity. Hence, as early as 1921, Washburn [104] found that the covered distance $x_f(t)$ of the front line should evolve as

$$x_f^2 = \frac{2}{b}t, \tag{8.24}$$

as previously introduced in Eq. (5.5). Again, images of the imbibed strips are recorded every 10 seconds to obtain image series as displayed in Fig. 8.8. These images are submitted to Matlab image processing routines to transform them analogously to Fig. 8.7. Here, the area of the binary spot is $A_{spot} = 2wx_f(t)$ yielding $x_f(t)$. The ring clamp in the setup is used to diametrally suspend a paper strip of $w = 20$ mm width. It is fed by a bar wick of 40 mm width that extends on both sides of the strip as illustrated by Fig. 8.9. As soon as contact between wick and strip is established the liquid imbibes the porous material in both directions starting from $x_f(t = 0) = \pm x_0$. The resulting data for all four papers in terms of $x_f^2$ over $t$ according to Eq. (8.24) is shown in Fig. 8.10. That exposition enables a linear fit to find the parameter $b$. As one would expect, all four curves are straight lines. This fact is also supported by the regression coefficients $\rho_h$ (see for example [14] for definition) of the fits provided for all papers in Table 8.4.

**Wicking into a vertical strip** The course of action here resembles the horizontal case. One difference is that the specimen is not fed by a wick but dipped into the liquid and a mass

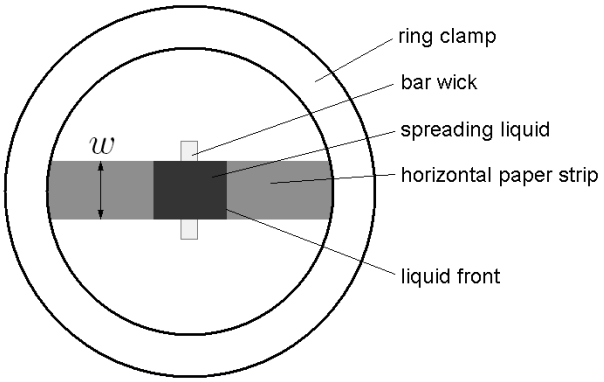


Figure 8.9: Experimental arrangement for the horizontal strip experiments (top view).

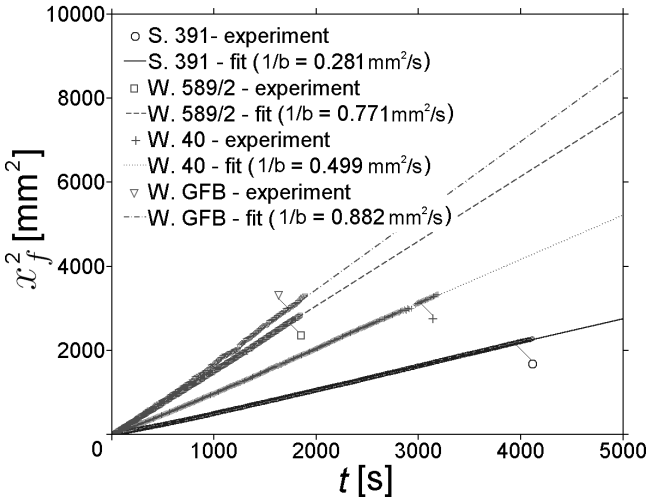


Figure 8.10: Reference measurement in horizontal strips of the four test papers. Steeper slopes indicate faster wicking.

measurement is recorded. Consequently, a wetting jump occurs in the beginning. It is followed by a capillary rise period which is mainly governed by capillarity and viscous flow losses alone before hydrostatics becomes important. Only the linear initial part of the $x_f^2(t)$ plot is used for the fit. Detailed information of the procedure is given in [35]. The regression coefficients $\rho_v$ for the linear fits in the vertical case are also provided by Table 8.4.

From both strip experiments the parameter $b$ is extracted, which can be regarded as a wicking constant. This combination of material, liquid and porous properties applies for wicking problems unaffected by the particular geometry. Its mean value $\overline{b}$ is calculated as well as its error $\Delta b$, see Table 8.4. Here, the mean value is defined as $\overline{b} = (b_h + b_v)/2$ and the error is defined as $\Delta b = \sqrt{(b_h - \overline{b})^2 + (b_v - \overline{b})^2}$.

### 8.3.2 Radial outward wicking

Each of the four different filter papers was investigated with the three different wick sizes, thus providing 12 outward wicking experiments. In preliminary experiments the reproducibility of the data presented has been checked. This was done by measuring the total duration of the wicking process several times. It was found that these durations are within the error margins due to paper anisotropy which were discussed in the error estimation above. In favor of clarity only one representative run per parameter set was picked which was then recorded and evaluated.

Table 8.4: Reference data for the wicking parameter $b$, gained from strip wicking experiments in horizontal and vertical direction.

| | Sartorius 391 | Whatman 589/2 | Whatman 40 | Whatman GFB |
|---|---|---|---|---|
| Horizontal $b_h$ [s/mm$^2$] | 3.559 | 1.297 | 2.004 | 1.134 |
| Regression coeff. $\rho_h$ | 0.9996 | 0.9998 | 0.9396 | 0.9999 |
| Vertical $b_v$ [s/mm$^2$] | 3.425 | 1.473 | 1.637 | 1.167 |
| Regression coeff. $\rho_v$ | 0.9999 | 0.9997 | 0.9991 | 0.9992 |
| Mean value $\overline{b}$ [s/mm$^2$] | 3.492 | 1.385 | 1.821 | 1.151 |
| Error $\Delta b$ [s/mm$^2$] | $\pm$0.095 | $\pm$0.125 | $\pm$0.259 | $\pm$0.023 |

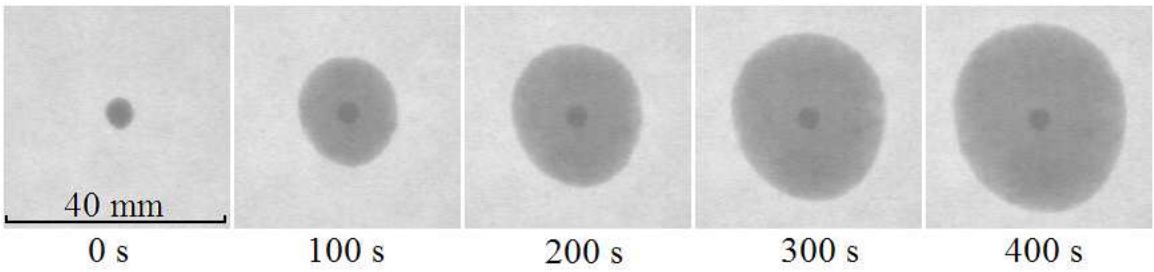


Figure 8.11: Evolution of the wetted area in radially outward transport using cellulose paper.

Figs. 8.11 and 8.12 give an impression on how the observed spots evolve in cellulose paper and glass fiber paper, respectively. Obviously, cellulose paper provides a sharp edge while it is a blurred edge in glass paper. The reasons for this very different edge contrast might be due to i) the porosity of the cellulose fibers itself while the glass fibers are non-porous, ii) different wetting conditions, iii) the higher thickness of the glass paper. Nonetheless, this effect which makes the Matlab evaluation of the wetted spots more difficult is not anticipated.
Both the experimental data points $r_f(t)$ and the model predictions $r_f(t)$ that are based upon the linear reference data are presented in Figs. 8.13 - 8.16. The predictions are obtained by rearranging Eq. (8.14) into its dimensional form

$$t(r_f) = \frac{b\, r_f^2}{4} \left[ \ln\left(\frac{r_f^2}{r_0^2}\right) + \frac{r_0^2}{r_f^2} - 1 \right] , \tag{8.25}$$

applying for $b$ the $\overline{b}$-value provided by the linear reference experiments, see Table 8.4. In all four figures the experimental data-curves are within the expected error margins. Therefore, one can state that the linear reference experiments are useful to predict the outward radial wicking process.

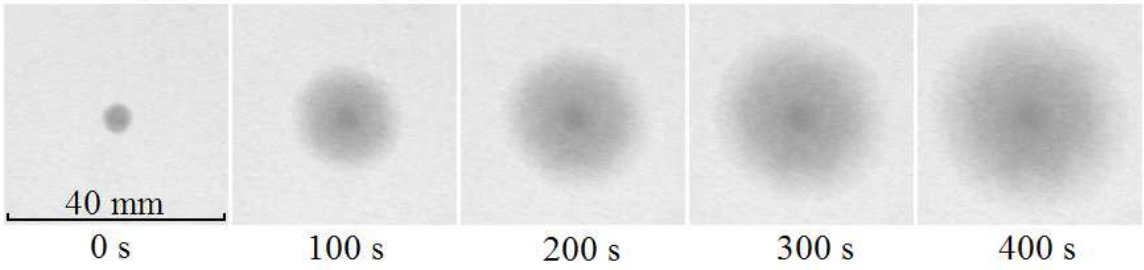


Figure 8.12: Evolution of the wetted area in radially outward transport using glass fiber paper. Although hard to perceive, there is a distinct front line on the outer rim of the diffuse spot on which the edge detection algorithm is attuned.

Table 8.5: The wicking parameter $b$, gained from fits of Eq. (8.25) to the outward wicking experiments with 3 different wicks. To compare with the linear experiments see Table 8.4.

| Values for $b$ [s/mm$^2$] | Sartorius 391 | Whatman 589/2 | Whatman 40 | Whatman GFB |
|---|---|---|---|---|
| $r_0 = 2.05$ mm | 3.493 | 1.180 | 1.967 | 0.784 |
| $r_0 = 2.5$ mm | 3.463 | 1.114 | 1.665 | 1.012 |
| $r_0 = 10$ mm | 3.708 | 1.244 | 2.028 | 0.881 |
| Mean value $\overline{b}$ | 3.555 | 1.179 | 1.887 | 0.892 |
| Error $\Delta b$ | $\pm$0.134 | $\pm$0.065 | $\pm$0.194 | $\pm$0.114 |

Analogous to Table 8.4, the values of $b$ gained by fitting Eq. (8.25) to the data of the outward wicking experiments are provided in Table 8.5. Here, $\overline{b} = (b_1 + b_2 + b_3)/3$ and $\Delta b = \sqrt{0.5\left[(b_1 - \overline{b})^2 + (b_2 - \overline{b})^2 + (b_3 - \overline{b})^2\right]}$. However, throughout the four figures not a single data-curve actually coincides with the prediction. Instead, it can be observed that the data-curves sometimes intersect the prediction-curves. This cannot be explained by a mismatching value of $\overline{b}$ alone because shifting $\overline{b}$ would lead to prediction-curves completely above or below the data. This issue is addressed in the 'discussion' section.

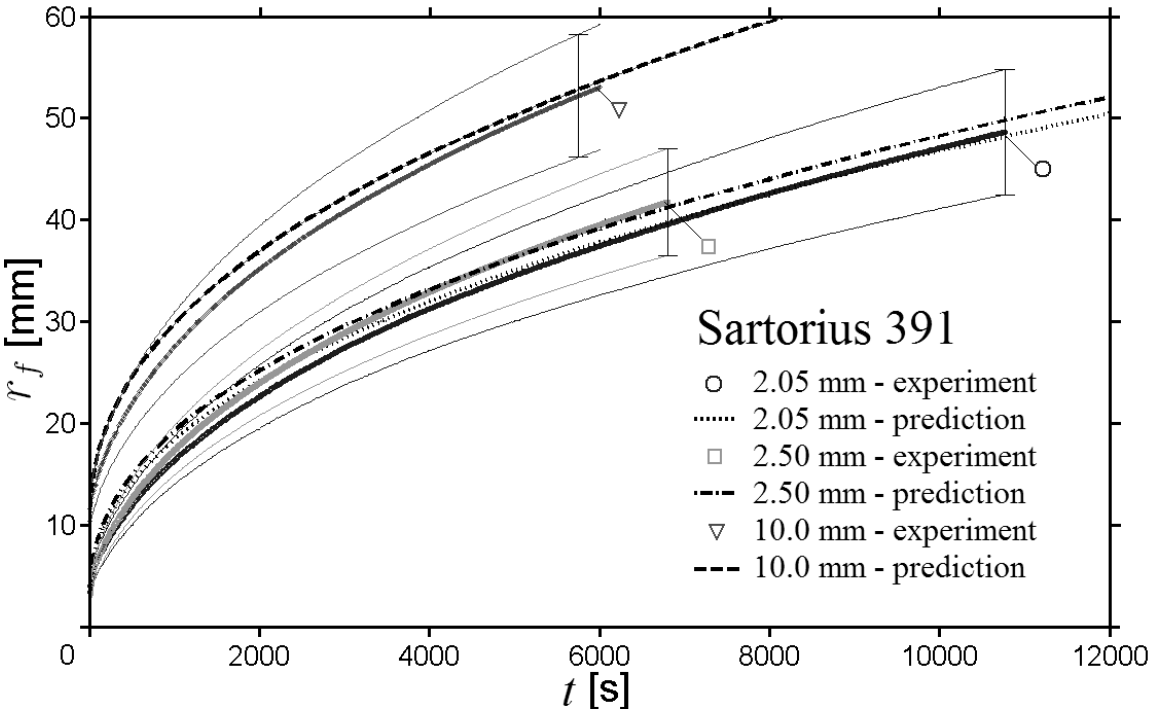


Figure 8.13: Diagram showing radius versus time for outward wicking in Sartorius 391 filter paper. The predictions are based on linear reference experiments (more exactly on the $\bar{b}$-value in Table 8.4).

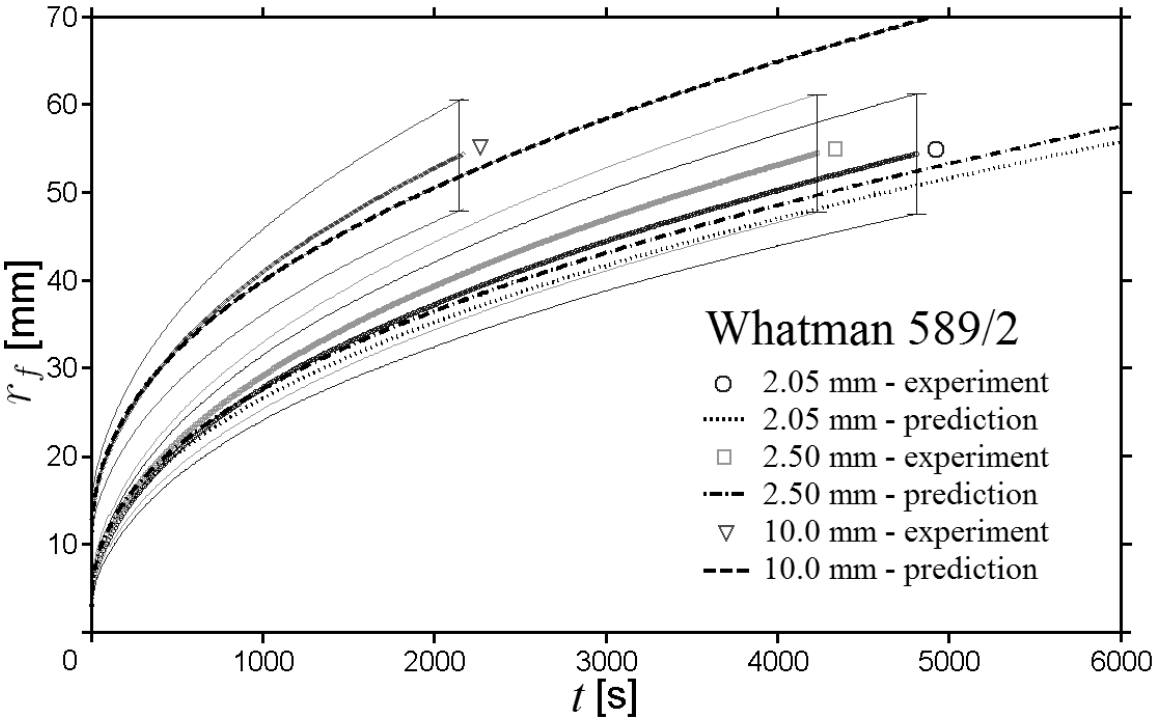


Figure 8.14: Diagram showing radius versus time for outward wicking in Whatman 589/2 filter paper.

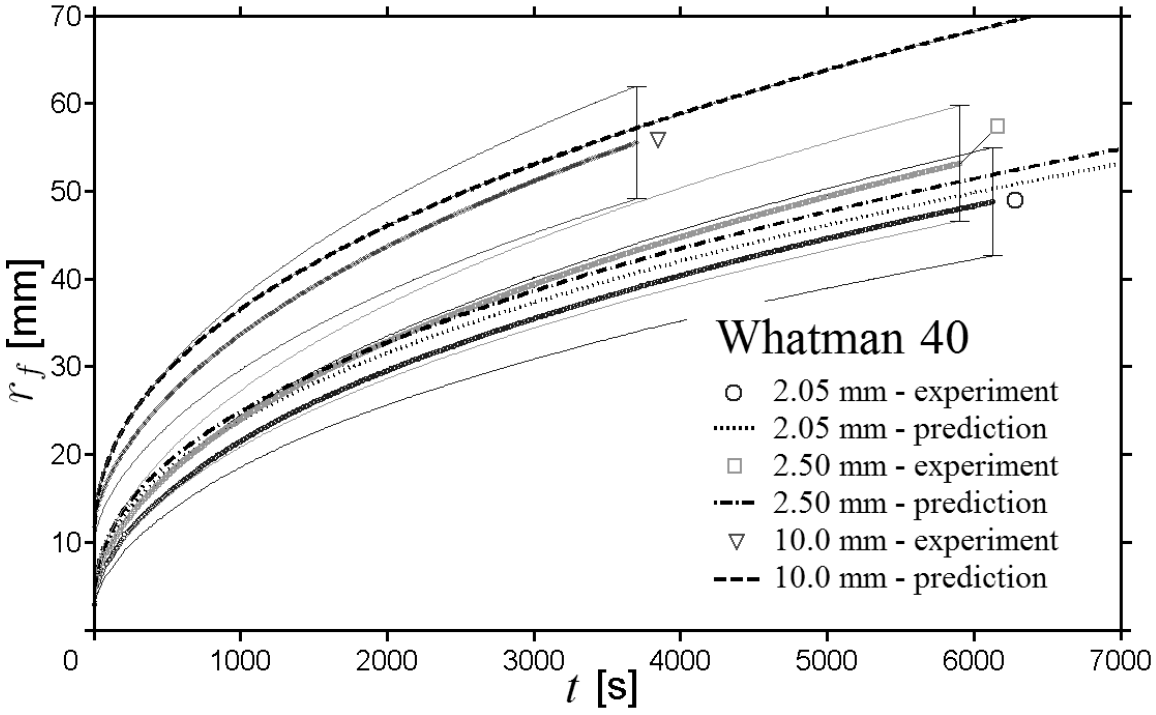


Figure 8.15: Diagram showing radius versus time for outward wicking in Whatman 40 filter paper.

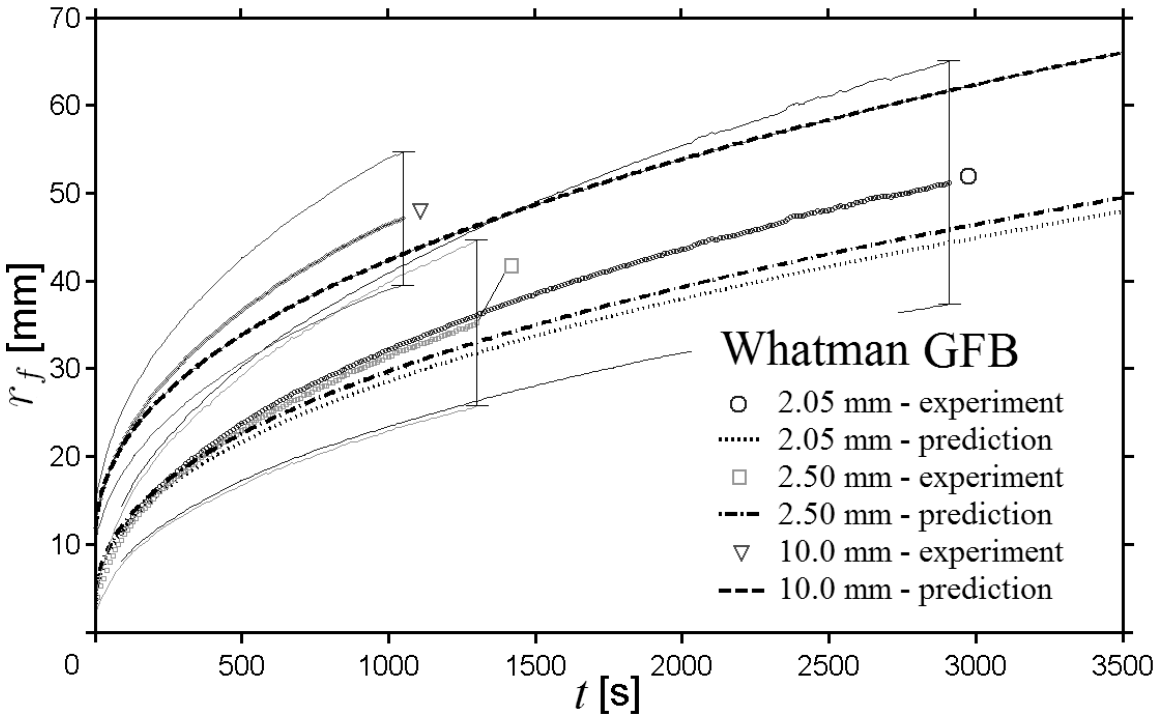


Figure 8.16: Diagram showing radius versus time for outward wicking in Whatman GFB filter paper.

Table 8.6: The wicking parameter $b$, as gained from theoretical prediction and three experiments.

| Values for $b$ [s/mm$^2$] | Sartorius 391 | Whatman 589/2 | Whatman 40 | Whatman GFB |
|---|---|---|---|---|
| paper properties | 7.508 | 1.236-3.717 | 5.394 | - |
| horizontal strip | 3.559 | 1.297 | 2.004 | 1.134 |
| vertical strip | 3.425 | 1.473 | 1.637 | 1.167 |
| radially outward | 3.555 | 1.179 | 1.887 | 0.892 |
| Mean value $\overline{b}$ | 4.512 | 1.296 | 2.731 | 1.064 |
| Error $\Delta b$ | $\pm$1.998 | $\pm$0.127 | $\pm$1.782 | $\pm$0.150 |

### 8.3.3 Overview on obtained wicking constants

Knowledge of the wicking constant $b$ allows to predict how fast a wetted spot will grow. Here, $b$ has been derived by four different ways: i) theoretically from paper properties, ii) from linear wicking experiments in horizontal strips, iii) from linear wicking experiments in vertical strips and iv) from radially outward wicking experiments in horizontal screens. Table 8.6 provides a summary of these results. It shows that especially the theoretical prediction from the manufacturer information deviates from the mean value, and it often appears to be crude and fragmentary.

### 8.3.4 Dimensionless presentation

To expand the comprehension of the problem it is depicted in dimensionless form by plotting $r_f^\star = f(t^\star)$. This is accomplished by applying Eqs. (8.4), (8.5) to the data points. The dimensionless master curve is given by Eqs. (8.14) and (8.18) for outward wicking.

Fig. 8.17 displays all 12 outward wicking experiments along with the theoretical prediction, see Eq. (8.18), in dimensionless form $r_f^\star(t^\star)$. After all, the four papers used in the experiments are just a means to study the radial wicking process that applies to porous media in general. Because the observation radius in the experiments is restricted to 75 mm, see Fig. 8.6, the four experiments with 10 mm-wick (triangle signs) are depicted in the $r_f^\star = 0...7.5$ region and are therefore barely visible. Nevertheless, one recognizes that the thin error margin lines do not separate from the other curves what means that the data points are within the expected area. The four experiments with 2.5 mm-wick (square signs) and the four experiments with 2.05 mm-wick (circle signs) are easier to distinguish. Apparently the mastercurve lies well within

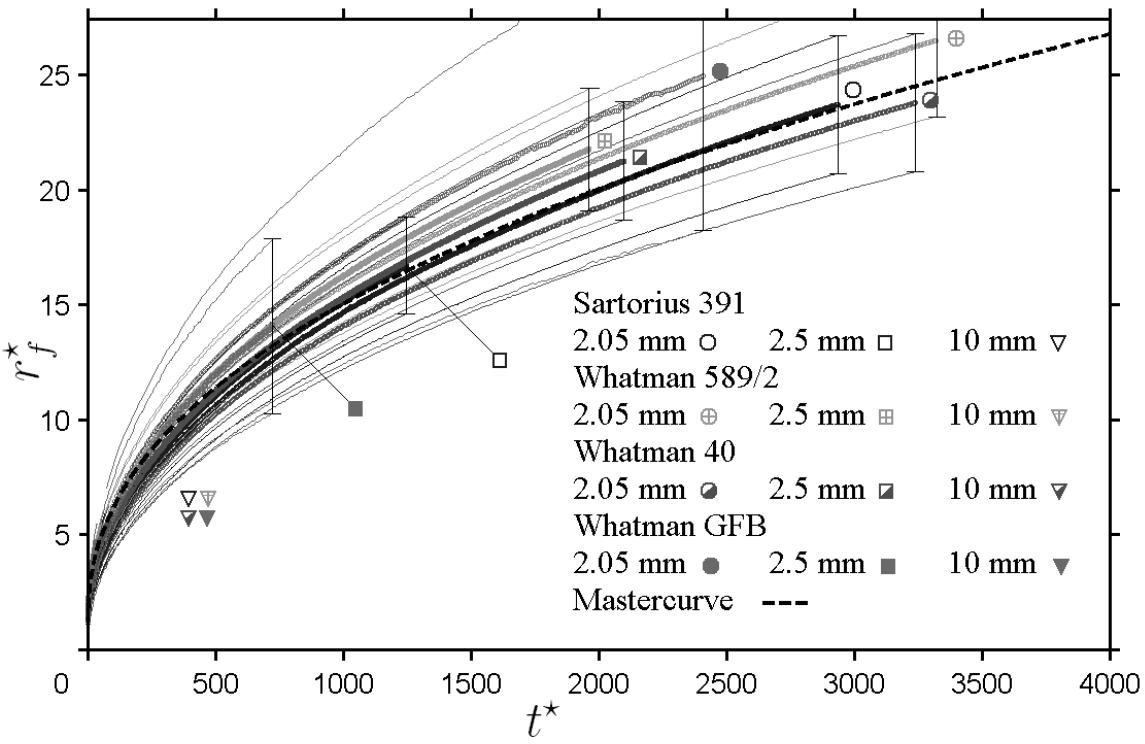


Figure 8.17: Dimensionless presentation of the outward wicking experimental data and the prediction mastercurve Eq. (8.18). Here, the data curves are complemented by its corresponding error margin curves as betoken by the vertical solid lines at the end of each data curve. The $b$ value for the dimensionless scaling is based on the linear reference experiments ($\bar{b}$-value in Table 8.4).

the experimental data. All data curves collapse with the mastercurve within the expected error margins. One can see that the spot which spread farthest reached $r_f^\star = 26.4$ and $t^\star = 3300$. Therefore, these values mark the limit of the experimental corroboration.

## 8.4 Discussion

The model developed is simplified insofar that it neglects the viscous pressure drop in the feeding wick, the hydrostatic pressure between paper and liquid reservoir as well as inertial effects. These are the same presuppositions like Marmur [64] has chosen for the radial capillary, see Fig. 8.18.

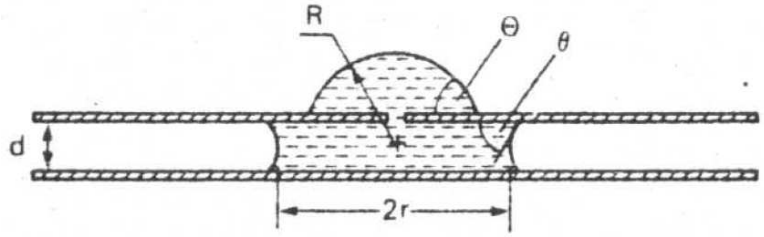


Figure 8.18: Axially symmetric geometry of the radial capillary that was studied by Marmur [64].

In fact one finds the theoretical solution to resemble that of the radial capillary:

$$\left(\frac{r_f}{r_0}\right)^2\left[\ln\left(\frac{r_f}{r_0}\right)^2+\left(\frac{r_0}{r_f}\right)^2-1\right] = \frac{2\sigma\cos(\theta)d}{3\mu r_0^2}t \quad \text{Eq. (25) in [64] rearranged} \tag{8.26}$$

$$\left(\frac{r_f}{r_0}\right)^2\left[\ln\left(\frac{r_f}{r_0}\right)^2+\left(\frac{r_0}{r_f}\right)^2-1\right] = \frac{8\sigma\cos(\theta)K}{\mu\phi R_s r_0^2}t \quad \text{Eq. (8.14) rearranged} \tag{8.27}$$

Hence, the two models are compatible. This is interesting because Marmurs derivation contains no porous medium, however deals with the same physical effects. His only geometrical parameters are plate distance $d$ and initial radius $r_0$. The presented solution instead is based on the Darcy law in porous media. Canceling out the right-hand terms of both equations gives for the corresponding distance $d$ between the parallel plates

$$d = \frac{12K}{\phi R_s}. \tag{8.28}$$

This equation clearly shows the analogy between radial flow in porous media and radial flow between parallel plates. As previously discussed (see section 2.2.2) an analogy for linear flow in a porous medium and a cylindrical capillary tube is given by Eq. (2.3), which displays a remarkable similarity to Eq. (8.28). For linear capillary transport between capillary plates the same approach and assumptions as applied for the Lucas-Washburn equation [104] can be used to obtain [87]

$$x_f^2 = \frac{\sigma\cos(\theta)\,d}{3\mu}\,t. \tag{8.29}$$

Here, a viscous pressure drop of

$$\Delta p = -\frac{12x_f\dot{x_f}\mu}{d^2}, \tag{8.30}$$

and a capillary pressure of

$$\Delta p = -\frac{2\sigma\cos(\theta)}{d} \tag{8.31}$$

is applied. Note that, contrary to cylindrical tubes, only one principal radius of curvature has to be considered.

The hydrostatic pressure neglect is contained in the error estimation. The neglect of pressure drop in the feeding wick, on the other hand, is not. But apparently, it visibly disturbs the comparison between experimental data and model prediction. According to the model, the liquid flow rate that the porous material draws from the reservoir, is infinite in the beginning. This holds for both outward and inward wicking, see Eq. (8.23) and Figs. 8.4 and 8.5. Naturally, the wick cannot support an infinite flow rate and will retard the delivery of liquid. Hence in the beginning the observed wetted spot will grow more slowly in the experiment than predicted. The neglect of the inertial effects is justified as the inertial parameter $\pi_3$, see Eqs. (8.10) and (8.8), is very high for all performed experiments, see Table 8.8.

Another issue to be clarified is the contact between feeding wick and reservoir. As the experiments show the first contact is pointwise. But once happened, complete contact is suddenly established aided by liquid bridges. The elapsed time for this liquid bridging was much smaller compared to the whole duration of the wicking process.

The characteristic times of all experiments calculated by Eq. (8.7) are listed in Table 8.7.

In dimensionless terms, the coverage of the experiments extends to $0 \leq r_f^\star \leq 27$ and $0 \leq t^\star \leq 3300$. The outward wicking process is boundless in space and time, therefore the experimental basis is limited here.

Table 8.7: Characteristic time $t_c$ [s] of the wicking process for all experiments.

| $t_c$ [s] | Sartorius 391 | Whatman 589/2 | Whatman 40 | Whatman GF/B |
|---|---|---|---|---|
| $r_0 = 2.05$ mm | 3.67 | 1.45 | 1.89 | 1.21 |
| $r_0 = 2.5$ mm | 5.45 | 2.16 | 2.82 | 1.80 |
| $r_0 = 10$ mm | 87.26 | 34.48 | 45.04 | 28.75 |

Table 8.8: Value of the inertial parameter $\pi_3$ [-] for all experiments.

| $\pi_3$ [−] | Sartorius 391 | Whatman 589/2 | Whatman 40 | Whatman GF/B |
|---|---|---|---|---|
| $r_0 = 2.05$ mm | $0.21 \cdot 10^9$ | $0.08 \cdot 10^9$ | $0.14 \cdot 10^9$ | $0.46 \cdot 10^9$ |
| $r_0 = 2.5$ mm | $0.32 \cdot 10^9$ | $0.12 \cdot 10^9$ | $0.21 \cdot 10^9$ | $0.69 \cdot 10^9$ |
| $r_0 = 10$ mm | $5.08 \cdot 10^9$ | $1.98 \cdot 10^9$ | $3.39 \cdot 10^9$ | $11.0 \cdot 10^9$ |

## 8.5 Conclusion

A theoretical study is presented on capillary transport in radial direction, supported by experiments investigating outward transport. The model is based on Darcy's law in porous media and assumes a viscous dominated flow regime. It can well predict the evolution of the wetted area and is compatible to the radial capillary model of Marmur. Experiments are performed with filter paper and three cylinder-wicks for outward flow. The recorded images are evaluated with Matlab. In addition to the radial wicking experiments linear wicking experiments in both horizontal and vertical strips are considered. These linear experiments serve as reference, which also allows to obtain the necessary constants to predict the radial wicking process. Thus, the pore structure parameters $K$, $R_s$ and $\phi$ (in lumped form of $b$) are obtained by different experimental methods which provide reasonable agreement (Table 8.6). The impact of the observations made is also discussed in section 9.7.

So overall, this study covers a spectrum of three different wicking experiments along with an appropriate theory. For the outward wicking processes the agreement between experiments and prediction is within the specified error margins.

# Chapter 9

# Summary

The aim of the presented work is to investigate capillary dominated transport processes in porous materials and small tubes. The first part of the work is devoted to a fundamental discussion of the theory of capillary rise. Here, a detailed dimensional analysis and an introduction to the different time stages and analytical approaches to this phenomenon are presented. The second part of the work shows two experimental setups. The corresponding chapters describe the experiments performed to investigate capillary dominated flows of particular interest to space propulsion systems. They provide relevant experimental data to verify the mathematical models.

## 9.1 Dimensionless scaling methods

In the chapter "Dimensionless scaling methods for capillary rise", three different scaling options using the Buckingham $\pi$ theorem are systematically derived. It is shown that three forces - identified as inertial, viscous and hydrostatic forces - can be used to obtain these three scaling sets, each consisting of two dimensionless variables and one dimensionless basic parameter. From a general point of view the scaling options are all equivalent and valid for describing the problem of capillary rise. Contrary to this for certain cases - depending on the time scale and the dominant forces - one of the options can be favorable. For example, using the appropriate scaling can help to identify the influence of a certain parameter to be investigated. Also for some special cases, for example including microgravity, the choice is limited to a single scaling method. The three different sets are discussed systematically. It is evaluated which scaling is most useful for certain cases. Furthermore, numerical as well as analytical solutions of the momentum balance are shown in dimensionless form. Their ranges of applicability when

compared to numerical solutions of the differential equation of motion are determined. Based on this data an appropriate scaling to represent experimental data of capillary rise can be chosen. This can help to systematically plan an experimental campaign in advance by defining which dimensionless basic parameter shall be varied.

## 9.2 Transition between different time regimes

It is found that the capillary rise process can be separated into different time stages where different forces dominate. In the chapter "The transition from inertial to viscous flow" the early stages of capillary rise of a liquid in a tube are investigated. In this period, both inertia and viscous flow losses balance the pressure generated by the meniscus curvature (capillary pressure). It is known that the very first stage is dominated purely by inertial forces, but subsequently the influence of viscosity increases (visco-inertial flow). From the calculations, one can conclude that the purely inertial and the purely viscous flow period are separated by a visco-inertial stage where both effects have to be considered. Finally the effect of inertia vanishes and the flow becomes purely viscous. The times and meniscus heights at which the transition between the time periods occur are derived. This provides a method to determine a priori which terms of the momentum balance are relevant for a given problem, as only these terms have to be taken into account to obtain a solution of sufficient precision. Analytical solutions known from literature [11, 61, 78, 104] are discussed and the time intervals of their validity compared. The predicted transition times and the calculated heights show good agreement with experimental results from literature [89]. The results are also discussed in dimensionless form and the limitations of the calculations are pointed out. Up to now, typically the time where the solution for the inertial and the viscous rise provide the same height has been used as a measure for the separation between the time stages. However, it is shown that it takes about eight times as long for the flow to become independent of inertial effects.

## 9.3 Analytical solutions including the gravity term

For a setup not in a microgravity environment, gravity begins to become a dominating force in the later time stages of capillary rise. The chapter "Analytical solutions including the gravity term" focuses onto this domain. An analytical solution for the capillary rise of liquids in a cylindrical tube or a porous medium is derived in terms of height $h$ as a function of time $t$. The implicit $t(h)$ solution by Washburn is the basis for these calculations and the Lambert

W function is used for its mathematical rearrangement. The original equation is derived from the 1D momentum conservation equation and features viscous and gravity terms. Thus, in contrast to the Lucas-Washburn equation, the presented $h(t)$ solution includes the gravity term and enables the calculation of the liquid rise behavior for longer time scales. Based on the new equation, it is possible to derive several parameters including the time necessary to reach a static state. Also the error made by neglecting gravity and using the Lucas-Washburn equation is determined. The results are also discussed in dimensionless form and a dimensionless plot of the Lucas-Washburn equation and the extended solution including gravity is shown. The flow velocity is obtained by differentiating the height and a dimensionless number for its description is found. In the second part of this chapter the analytical solution is extended to describe the dynamics of a broader set of initial conditions such as varying the initial height. These may involve capillary rise, capillary fall or drainage. Capillary fall refers to a meniscus starting from a position above the equilibrium height and subsequently moving down towards the equilibrium height. In the introduced model capillary, viscous, and gravity effects are considered. This is also discussed by means of dimensionless numbers, which enable to plot a characteristic diagram showing rise and fall regimes. Good agreement is observed between the experimental results taken from literature [85] and the prediction by the presented model.

## 9.4 Macroscopical numerical simulation

In the chapter "A basic macroscopic numerical simulation with FLOW-3D", a numerical method to simulate capillary rise in porous media is briefly presented. Here a macroscopical approach is used, which implies the application of an integral model to represent both the effects of the capillary pressure and the effect of viscous flow resistance. If one provides the code with the capillary pressure and an integral permeability of the porous material, the code (FLOW-3D) then applies the correct boundary condition at the fluid interface (capillary pressure) and the viscous flow resistance is modeled in each grid cell using the Darcy law. With this fairly simple approach wicking of liquids into porous materials can be simulated. Comparison to mathematical models shows excellent agreement. As a disadvantage has to be considered that the material properties such as the permeability must be known a priori to set up the simulation. This issue can only be solved by microscopic approaches or experiments. For small structures (e.g. a representative volume), a microscopic simulation will provide useful data within reasonable time. This allows to extract the pore structure parameters $K$, $R_s$ and $\phi$ from the microscopic simulation to use them in a macroscopic simulation.

## 9.5 Capillary rise and the effect of evaporation

As previously mentioned, the second part of this work focuses on experimental work. In the chapter "Linear capillary rise and the effect of evaporation" the wicking of different liquids into a dry Dutch Twilled Weave (DTW 200 × 1400) is analyzed by combining experimental and analytical approaches. Experiments using a vertically positioned weave are performed under isothermal, terrestrial conditions. The results are compared to analytical solutions showing good agreement between the Lucas-Washburn equation and the experimental data for flow regimes where gravity and evaporation effects are negligible. From the measurements, the permeability and static radius for the capillary pressure of the structure can be determined. No significant influence of the screen width onto the wicking process is found. However, the capillary rise in warp direction occurs about twice as fast as in weft direction. This results from a difference in the permeabilities by about this factor due to the thicknesses of the wires and the weave structure. The results for the slope parameter $K/R_s$ are validated by previous literature [28, 98], but there are discrepancies for the static radius which may occur due to the sensitivity of the experiment to evaporation.

To investigate the influence of evaporation on the capillary rise process, experiments with volatile liquids are conducted. Significant deviations from classical models are observed. Thus, an enhanced form of the standard wicking model from Lucas and Washburn is introduced to account for evaporation and gravity effects. By comparing the experimental results with the enhanced wicking model, good qualitative agreement is found. Using dimensionless parameters it is possible to plot all experimental data in a single diagram to compare different fluids and evaporation rates. The experimental data supports the theoretical model, although it shows that the model tends to overestimate the reached height by about 20%. It is noted that evaporation may have a major retarding impact on the wicking process.

## 9.6 Radial capillary transport

Finally, in the chapter "Radial capillary transport", radial liquid movement is studied in contrast to linear movement as investigated in the previous chapters. Application of radial transport is also under consideration for propellant management in space. A theoretical and experimental study on the more basic situation when liquid spreads radially from an infinite reservoir is presented. Based on Darcy's law in porous media and assuming a viscous dominated flow regime, the theoretical model predicts both outward and inward radial transport in a porous

screen. It can well predict the evolution of the wetted area and is compatible to the radial capillary model of Marmur [64]. For both cases (outward and inward transport) an analytical solution is obtained in terms of time versus radius as well as radius versus time aided by the Lambert W function. In the experiments four different filter papers are used combined with three cylindrical wicks for outward wicking. In addition to the radial wicking experiments linear wicking experiments in both horizontal and vertical strips are considered. These linear experiments serve as reference to obtain the necessary material parameters. Therefore a prediction of the radial wicking process is enabled. Overall, a spectrum of three different wicking experiments along with an appropriate theory is covered. The agreement between experiments and prediction is within the specified error margins for the outward wicking processes.

## 9.7 Pore structure parameters

In conclusion it can be stated that the pore structure parameters $K$, $R_s$ and $\phi$ have proven to be a very useful tool to macroscopically describe capillary transport in porous structures. The values obtained by different experimental approaches are in reasonable agreement, e.g. see Table 8.6. However, it was found that the values provided by the suppliers of porous samples may sometimes be rough estimates. Also, due to different definitions and models for special applications, e.g. the Herzberg filtration time, they may be hard to correlate to the parameters used here. In the context of PoreNet this means that the pore structure parameters for the porous samples used should be measured experimentally to compare them to the values provided by the suppliers. For validation purposes it should be considered to apply different experimental methods for each parameter. For example, the porosity $\phi$ could be determined from mercury intrusion, capillary rise mass recordings and the weight of a completely wetted specimen. For the determination of $K$ cross flow pressure drop measurements and the capillary rise rate can be applied, while for $R_s$ the bubble point method, the maximum height $h_{eq}$ or mercury intrusion are useful. The same applies for advanced methods like computer tomography which allows to obtain a microscopic three dimensional image of the pore structure. This data could be used in a microscopic numerical simulation to obtain the pore structure parameters. Linking and comparing the values obtained by different methods will allow to determine the pore structure parameters with more precision, but will also allow to understand the processes in more depth. For example, using glass filter frits the difference between $R_s$ and the radius determined by the bubble point method (see Table 7.10) may be traced back to the fact that the bubble point method determines the largest pore. However, as $R_s$ is smaller, it seems that the wicking

effective capillary pressure is not only influenced and restricted by the largest pores, but also by the smaller ones.

Capillary dominated flows still prove to be a challenging, however, interesting and relevant field for research in fluid mechanics. This work is intended to be a contribution to the fundamental understanding and classification of capillary flows, and a foundation for further work on capillary flows in PoreNet. Although no specific geometries have been discussed here, the research also aims to provide guidelines and models for engineers designing Propellant Management Devices in space applications. As an outlook it can be stated that especially for non-isothermal setups many problems remain to be addressed. While this work is restricted to isothermal cases with storable liquids some rockets use cryogenic propellants such as oxygen and hydrogen due to their higher specific impulse. The realization of Propellant Management Devices for this type of liquids involves many fields that have been addressed in this work - however with isothermal setups. As preliminary experiments show, cryogenic capillary rise can be demonstrated and measured using liquid nitrogen and porous materials like metallic screens or filter frits. The next step within the framework of PoreNet will be to experimentally investigate relevant non-isothermal setups and to extend the known analytical and numerical models of capillary dominated flows to these cases. Especially for cryogenic setups the effect of evaporation and other heat transfer issues will be of major importance.

# Appendix A

# Mathematical derivations

The first three calculations (A.1 - A.3) presented in the following are not originally calculated by the author, but recalculated from the available information provided in the original publications.

## A.1 Derivation of the Quéré solution

To solve the differential equation Eq. (4.2)

$$\frac{d\left(h\dot{h}\right)}{dt} = \frac{2\sigma\cos(\theta)}{\rho R}, \tag{A.1}$$

one may separate the variables to obtain

$$\int d\left(h\dot{h}\right) = \int \frac{2\sigma\cos(\theta)}{\rho R} dt. \tag{A.2}$$

By integrating it reads

$$h\frac{dh}{dt} = \frac{2\sigma\cos(\theta)}{\rho R} t + C, \tag{A.3}$$

and due to boundary condition $h(t=0)=0$, $C$ can be calculated to be zero. By repeating the previous steps again, one finally obtains

$$\frac{1}{2}h^2 = \frac{1}{2}\frac{2\sigma\cos(\theta)}{\rho R} t^2 + C_2, \tag{A.4}$$

and due to the initial condition one arrives at the solution of constant velocity by Quéré [78]

$$h = t\sqrt{\frac{2\sigma\cos(\theta)}{\rho R}}. \tag{A.5}$$

## A.2 Derivation of the Bosanquet solution

To solve the differential equation Eq. (4.4)

$$\frac{d}{dt}\left(h\dot{h}\right) + b_1 h\dot{h} = b_2, \tag{A.6}$$

the following approach may be used. Note that due to the historical context the coefficients

$$b_1 = \frac{8\mu}{\rho R^2} = \frac{b}{a}, \tag{A.7}$$

and

$$b_2 = \frac{2\sigma\cos\theta}{\rho R} = \frac{1}{a}. \tag{A.8}$$

used by Bosanquet [11] are applied. By substituting

$$h\dot{h} = u, \tag{A.9}$$

one obtains

$$\frac{du}{dt} + b_1 u = b_2. \tag{A.10}$$

The homogeneous solution has to be found first

$$\int \frac{1}{u} du = \int -b_1 dt \tag{A.11}$$

provides

$$\ln(u) = -b_1 t \tag{A.12}$$

and finally

$$u_h = e^{-b_1 t}\, C_1 \tag{A.13}$$

and

$$\dot{u}_h = -b_1 e^{-b_1 t}\, C_1 + e^{-b_1 t}\, \dot{C}_1. \tag{A.14}$$

The inhomogeneous case can be used to find the unknown constant

$$e^{-b_1 t}\, \dot{C}_1 - b_1 e^{-b_1 t}\, C_1 + b_1 e^{-b_1 t}\, C_1 = b_2, \tag{A.15}$$

where $C_1$ is calculated from $\dot{C}_1$ to be

$$C_1 = \frac{b_2}{b_1} e^{b_1 t}. \tag{A.16}$$

Therefore $u$ (bringing together the homogeneous and the special solution) reads

$$u = u_h + u_{sp} = e^{-b_1 t}\, \frac{b_2}{b_1}\, e^{b_1 t} + e^{-b_1 t}\, C_2. \tag{A.17}$$

Due to the initial condition u(t=0)=0 one obtains

$$C_2 = -\frac{b_2}{b_1}, \tag{A.18}$$

and

$$u = \frac{b_2}{b_1}\left(1 - e^{-b_1 t}\right) \tag{A.19}$$

Resubstitution of $h$ provides

$$\int h dh = \int \frac{b_2}{b_1}\left(1 - e^{-b_1 t}\right) dt \tag{A.20}$$

and

$$\frac{1}{2}h^2 = \frac{b_2}{b_1}t + \frac{b_2}{b_1^2}e^{-b_1 t} + C_3. \tag{A.21}$$

As h(t=0)=0

$$C_3 = -\frac{b_2}{b_1^2}. \tag{A.22}$$

One finally arrives at the solution by Bosanquet [11] reading

$$h^2 = \frac{2b_2}{b_1}\left[t - \frac{1}{b_1}(1 - e^{-b_1 t})\right]. \tag{A.23}$$

## A.3 Derivation of the implicit Washburn equation

To solve the integral of Eq. (5.9) the following approach may be used:

$$t = \int \frac{bh}{1 - ch} dh = \int \frac{(ch - 1) + 1}{\frac{c}{b}(1 - ch)} dh. \tag{A.24}$$

This may be rearranged to

$$t = \int -\frac{b}{c} dh + \int \frac{b}{c}\frac{1}{1 - ch} dh. \tag{A.25}$$

Preparing the substitution

$$y = 1 - ch \tag{A.26}$$

by

$$dy = -c\, dh \tag{A.27}$$

gives

$$t = \int -\frac{b}{c} dh - \int \frac{b}{c^2}\frac{1}{y} dy. \tag{A.28}$$

Solving and reversing the substitute gives Eq. (5.10)

$$t = -\frac{bh}{c} - \frac{b}{c^2}\ln(y) = -\frac{bh}{c} - \frac{b}{c^2}\ln(1 - ch) + C, \tag{A.29}$$

which finally provides Eq. (5.13), the implicit equation by Washburn [104].

## A.4 Mathematical verification of the extended equation

To show that the extended solution Eq. (5.23) fulfills the differential equation Eq. (5.8) one may use the derivative of the solution and insert it into the initial differential equation. By differentiating the defining Eq. (5.17) for $W(x)$ [22] one obtains

$$\frac{dx}{dW(x)} = e^{W(x)} + W(x)e^{W(x)}. \tag{A.30}$$

Rearranging gives

$$W'(x) = \frac{1}{e^{W(x)} + W(x)e^{W(x)}}, \tag{A.31}$$

further

$$W'(x) = \frac{1}{e^{W(x)}(1 + W(x))}, \tag{A.32}$$

and

$$W'(x) = \frac{W(x)}{W(x)e^{W(x)}(1 + W(x))}. \tag{A.33}$$

By definition:

$$x = W(x)e^{W(x)} \tag{A.34}$$

and finally

$$W'(x) = \frac{W(x)}{x(1 + W(x))}. \tag{A.35}$$

To ease the handling of Eq. (5.23) a coefficient z can be defined:

$$z = -e^{-1-\frac{c^2 t}{b}}, \tag{A.36}$$

the derivative is

$$\frac{dz}{dt} = z\frac{-c^2}{b}. \tag{A.37}$$

Inserting Eq. (A.35), Eq. (A.37) (the inner derivative) and Eq. (5.23) into Eq. (5.8) gives

$$\frac{1}{c}\frac{W(z)}{z(1 + W(z))}z\frac{-c^2}{b} = \frac{c}{b(1 + W(z))} - \frac{c}{b}. \tag{A.38}$$

After some rearrangement one obtains

$$-W(z) = -W(z) \tag{A.39}$$

which proves that Eq. (5.23) is a solution to Eq. (5.8).

## A.5 Derivation for a general initial condition

In following the derivation of the analytical solution for the general initial condition $h(t_0) = h_0$ shall be explained in more detail. Starting from Eq. (5.10)

$$t = -\frac{bh}{c} - \frac{b}{c^2}\ln(1 - ch) + C \tag{A.40}$$

one can use the initial condition to obtain

$$t = -\frac{bh}{c} - \frac{b}{c^2}\ln(1 - ch) + t_0 + \frac{bh_0}{c} + \frac{b}{c^2}\ln(1 - ch_0). \tag{A.41}$$

Rearranging gives

$$\frac{c^2 t_0}{b} + ch_0 - \frac{c^2 t}{b} - ch = \ln[(1 - ch)(ch_0 - 1)], \tag{A.42}$$

and

$$\frac{c^2 t_0}{b} + ch_0 - \frac{c^2 t}{b} - ch = \ln[(ch - 1)(1 - ch_0)], \tag{A.43}$$

which gives

$$\ln(-1 + ch_0) - 1 + c\left(\frac{c}{b}t_0 + h_0 - \frac{c}{b}t\right) = \ln(ch - 1) + ch - 1. \tag{A.44}$$

After some further rearrangement

$$(-1 + ch_0)e^{-1+c\left(\frac{c}{b}t_0 + h_0 - \frac{c}{b}t\right)} = (ch - 1)e^{(ch-1)} \tag{A.45}$$

and applying the inverse properties of the Lambert W function as shown before one finally obtains

$$h(t) = \frac{1}{c}\left\{1 + W\left[(-1 + ch_0)e^{-1+c(-\frac{c}{b}(t-t_0)+h_0)}\right]\right\}. \tag{A.46}$$

This is Eq. (5.53).

# Bibliography

[1] B.N. Antar and V.S. Nuotio-Antar. *Fundamentals of Low Gravity Fluid Dynamics and Heat Transfer*, chapter 9, pages 265–287. CRC Press, Boca Raton, Florida, 1993.

[2] J.C. Armour and J.N. Cannon. Fluid flow through woven screens. *AIChE Journal*, 14(3):415–420, 1968.

[3] J. Bachmann, S.K. Woche, M.O. Goebel, M.B. Kirkham, and R. Horton. Extended methodology for determining wetting properties of porous media. *Water Resour. Res.*, 39(12), 2003.

[4] D.A. Barry, J.-Y. Parlange, D.A. Lockington, and L. Wissmeier. Comment on "The effect of evaporation on the wicking of liquids into a metallic weave" by N. Fries, K. Odic, M. Conrath and M. Dreyer. *J. Colloid Interf. Sci.*, 336:374–375, 2009.

[5] D.A. Barry, J.-Y. Parlange, G.C. Sander, and M. Sivaplan. A class of exact solutions for Richards' equation. *Journal of Hydrology*, 142:29–46, 1993.

[6] W. Batel. Vorausberechnung der Restfeuchtigkeit bei der mechanischen Flüssigkeitsabtrennung. *Chemie-Ing.-Techn.*, 8/9:497–501, 1955.

[7] P. Behruzi, C. Dodd, and G. Netter. Future propellant management device concepts for restartable cryogenic upper stages. In *43rd AIAA/ASME/SAE/ASEE Joint Propulsion Conference and Exhibit, Cincinnati, Ohio, AIAA 2007-5498*, 2007.

[8] P. Behruzi and G. Netter. Concept analysis of PMD designs for future upper stages. *54th International Astronautical Congress of the International Astronautical Federation, Bremen*, 2003.

[9] N. Bernet, V. Michaud, P.E. Bourban, and J.A.E. Manson. An impregnation model for the consolidation of thermoplastic composites made from commingled yarns. *J. Composite Materials*, 33(8):751–772, 1999.

[10] M. Blunt, D. Zhou, and D. Fenwick. Three-Phase Flow and Gravity Drainage in Porous Media. *Transport in Porous Media*, 20:77–103, 1995.

[11] C.H. Bosanquet. On the flow of liquids into capillary tubes. *Philos. Mag. Ser. 6*, 45:525–531, 1923.

[12] M. Bracke, F. De Voeght, and P. Joos. The kinetics of wetting: the dynamic contact angle. *Progress in Colloid & Polymer Science*, 79:142–149, 1989.

[13] I.N. Bronstein and K.A. Semendjajew. *Taschenbuch der Mathematik*. Teubner, 1985.

[14] I.N. Bronstein and K.A. Semendjajew. *Handbook of Mathematics. 20th edition*. Van Nostrand Reinhold, 1991.

[15] R.H Brooks and A.J. Corey. Hydraulic properties of porous media. *Hydrol. paper 3 Colo. State Univ., Fort Collins, Colorado, USA*, 1964.

[16] W. Brutsaert. The adaptability of an exact solution to horizontal infiltration. *Water Resour. Res.*, 4(4):785–789, 1968.

[17] E. Buckingham. On physically similar systems; illustrations of the use of dimensional equations. *Phys. Rev.*, 4(4):345–376, 1914.

[18] T.-Y. Chan, C.-S. Hsu, and S.-T. Lin. Factors affecting the significance of gravity on the infiltration of a liquid into a porous solid. *J. Porous Mat.*, 11(4):273–277, 2004.

[19] R. Chebbi. Dynamics of liquid penetration into capillary tubes. *J. Colloid Interface Sci.*, 315:255–260, 2007.

[20] E. Chibowski and R. Perea-Carpio. Problems of contact angle and solid surface free energy determination. *Advances in colloid and interface science*, 98:245–264, 2002.

[21] M. Conrath, N. Fries, M. Zhang, and M.E. Dreyer. Radial capillary transport from an infinite reservoir. *accepted for publication in Transport in Porous Media*, 2009.

[22] R.M. Corless, G.H. Gonnet, D.E.G. Hare, D.J. Jeffrey, and D.E. Knuth. On the Lambert W Function. *Advances in Computational Mathematics*, 5:329–359, 1996.

[23] D. Danino and A. Marmur. Radial capillary penetration into paper: Limited and unlimited liquid reservoirs. *J. Colloid Interf. Sci.*, 166(1):245–250, 1994.

[24] H. Darcy. *Les Fontaines Publiques de la Ville de Dijon.* Dalmont, Paris, 1856.

[25] P.S. de Laplace. *Supplément au livre X du Traitée de méchanique céleste.* Couvreier, Paris, 1806.

[26] T. Delker, D.B. Pengra, and P. Wong. Interface pinning and the dynamics of capillary rise in porous media. *Physical Review Letters*, 76(16):2902–2905, 1996.

[27] F.T. Dodge. *Low-Gravity Fluid Dynamics and Transport Phenomena, editor J.N. Koster and R.L. Sani*, volume 130, chapter 1, pages 3–14. Aeronautics and Astronautics, Washington, DC, 1990.

[28] F.T. Dodge. *The New Dynamic Behavior of Liquids in Moving Containers.* Southwest Research Institute, San Antonio, Texas, 2000.

[29] F.T. Dodge and E.B. Bowles. Vapor flow into a capillary propellant-acquisition device. *19th Joint Propulsion Conference, Seattle, Washington, AIAA-83-1380*, 1983.

[30] M.E. Dreyer. *Free Surface Flows under Compensated Gravity Conditions*, volume 221 of *Springer Tracts in Modern Physics.* Springer-Verlag, 2007.

[31] M.E. Dreyer, A. Delgado, and H.J. Rath. Capillary rise of liquid between parallel plates under microgravity. *J. Colloid Interf. Sci.*, 163(1):158–168, 1994.

[32] F.A.L. Dullien. *Porous Media, Fluid Transport and Pore Structure, second edition.* Academic Press, New York, 1992.

[33] Jr. E. Nenniger and J.A. Storrow. Drainage of Packed Beds in Gravitational and Centrifugal-force Fields. *A.I.Ch.E. Journal*, 4(3):305–316, 1958.

[34] D.H. Fenwick and M.J. Blunt. Three-dimensional modeling of three phase imbibition and drainage. *Advances in Water Resources*, 21:121–143, 1998.

[35] N. Fries and M. Dreyer. An analytic solution of capillary rise restrained by gravity. *J. Colloid Interf. Sci.*, 320(1):259–263, 2008.

[36] N. Fries and M. Dreyer. The transition from inertial to viscous flow in capillary rise. *J. Colloid Interf. Sci.*, 327(1):125–128, 2008.

[37] N. Fries and M. Dreyer. Dimensionless scaling methods for capillary rise. *J. Colloid Interf. Sci.*, 338(2):514–518, 2009.

[38] N. Fries, K. Odic, M. Conrath, and M. Dreyer. The effect of evaporation on the wicking of liquids into a metallic weave. *J. Colloid Interf. Sci.*, 321(1):118–129, 2008.

[39] N. Fries, K. Odic, and M. Dreyer. Wicking of perfectly wetting liquids into a metallic mesh. *Proceedings of the 2nd International Conference on Porous Media and its Applications in Science and Engineering; Kauai, USA*, 2007.

[40] W.H. Green and G.A. Ampt. Studies on soil physics. *J. Agri. Sci.*, 4:1–24, 1911.

[41] A. Hamraoui and T. Nylander. Analytical approach for the Lucas-Washburn equation. *J. Colloid Interf. Sci.*, 250:415–421, 2002.

[42] F. Hauksbee. An experiment touching the ascent of water between two glass planes in an hyperbolick figure (author's note: original source writes hyperbolick with ck). *Philosophical Transaction of the Royal Society of London*, 27:539–540, 1712.

[43] B. Hayes. Why W. *American Scientist, the magazine of Sigma Xi, The Scientific Research Society*, 93:104–109, 2005.

[44] M. Hemmat and A. Borhan. Creeping flow through sinusoidally constricted capillaries. *Phys. Fluids*, 7(9):2111–2121, 1995.

[45] R.L. Hoffman. A study of the advancing interface. I. Interface shape in liquid-gas systems. *J. Colloid Interface Sci.*, 50:228–241, 1975.

[46] N. Hsu and N. Ashgriz. Nonlinear penetration of liquid drops into radial capillaries. *J. Colloid Interf. Sci.*, 270(1):146–162, 2004.

[47] N. Ichikawa and Y. Satoda. Interface dynamics of capillary flow in a tube under negligible gravity condition. *J. Colloid Interf. Sci.*, 162:350–355, 1994.

[48] T.-S. Jiang, S.-G. Oh, and J.C. Slattery. Correlation for dynamic contact angle. *J. Colloid Interf. Sci.*, 69:74–77, 1979.

[49] J. Jurin. An account of some experiments shown before the royal society; with an enquiry into the cause of the ascent and suspension of water in capillary tubes. *Philos. T. R. Soc.*, 30:739–747, 1717-1719.

[50] M. Kaviany. *Principles of Heat Transfer in Porous Media*. Springer, New York, 1995.

[51] T. Kawase, S. Sekoguchi, T. Fuj, and M. Minagawa. Spreading of liquids in textile assemblies. *Text. Res. J.*, 56(7):409–414, 1986.

[52] A. Kaya. Untersuchung des Eindringverhaltens von Flüssigkeiten in poröse Medien. *Thesis (Diplomarbeit), University of Bremen*, 2007.

[53] E. Kissa. Capillary sorption in fibrous assemblies. *J. Colloid Interf. Sci.*, 83(1):265–272, 1981.

[54] M. Lago and M. Araujo. Capillary rise in porous media. *Physica A*, 289:1–17, 2001.

[55] B. Lavi, A. Marmur, and J. Bachmann. Porous media characterization by the two-liquid method: Effect of dynamic contact angle and inertia. *Langmuir*, 24(5):1918–1923, 2008.

[56] S.-L. Lee and H.-D. Lee. Evolution of liquid meniscus shape in a capillary tube. *J. Fluids Engineering*, 129(8):957–965, 2007.

[57] S. Levine, J. Lowndes, E.J. Watson, and G. Neale. A theory of capillary rise of a liquid in a vertical cylindrical tube and in a parallel-plate channel. *J. Colloid Interf. Sci.*, 73(1):136–151, 1980.

[58] S. Levine, P. Reed, E.J. Watson, and G. Neale. A theory of the rate of rise of a liquid in a capillary. In M. Kerker, editor, *Colloid and Interface Science*, volume 3, pages 403–419. Academic Press, New York, 1976.

[59] D.A. Lockington and J.-Y. Parlange. A new equation for macroscopic description of capillary rise in porous media. *J. Colloid Interf. Sci.*, 278:404–409, 2004.

[60] É. Lorenceau, D. Quéré, J.-Y. Ollitrault, and C. Clanet. Gravitational oscillations of a liquid column in a pipe. *Physics of Fluids*, 14(6):1985–1992, 2002.

[61] R. Lucas. Ueber das Zeitgesetz des kapillaren Aufstiegs von Flüssigkeiten. *Kolloid-Zeitschrift*, 23:15–22, 1918.

[62] D. Lukas and V. Soukupova. Recent studies of fibrous materials wetting dynamics. *In INDEX 99 Congress, Geneva, Switzerland*, 1999.

[63] K.J. Maloy, L. Furuberg, J. Feder, and T. Jossang. Dynamics of Slow Drainage in Porous Media. *Phys. Rev. Letters*, 68:2161–2164, 1992.

[64] A. Marmur. The radial capillary. *J. Colloid Interf. Sci.*, 124(1):301–308, 1988.

[65] A. Marmur. Penetration and displacement in capillary systems of limited size. *Adv. Colloid Interfac.*, 39:13–33, 1992.

[66] A. Marmur. Kinetics of Penetration into Uniform Porous Media: Testing the Equivalent-Capillary Concept. *Langmuir*, 19:5956–5959, 2003.

[67] A. Marmur and R.D. Cohen. Characterization of porous media by the kinetics of liquid penetration: The vertical capillaries model. *J. Colloid Interf. Sci.*, 189:299–304, 1997.

[68] G. Mason, H. Fischer, N.R. Morrow, and D.W. Ruth. Spontaneous counter-current imbibition into core samples with all faces open. *Transport Porous Med.*, 78:199–216, 2009.

[69] G. Mason and D.W. Mellor. Simulation of Drainage and Imbibition in a Random Packing of Equal Spheres. *J. Colloid Interface Sci.*, 176:214–225, 1995.

[70] R. Masoodi, K.M. Pillai, and P.P. Varanasi. Darcy's law-based models for liquid absorption in polymer wicks. *AICHE J.*, 53(11):2769–2782, 2007.

[71] G.H. McKinley. Dimensionless groups for understanding free surface flows of complex fluids. *Society of Rheology, Rheology Bulletin*, 74(2):6–9, 2005.

[72] M. Meistering. Bubble Point, Drop Point und Permeabilität, Dokumentation der Experimente an porösen Strukturen mit dem Topas PSM 165. *Work in progress, Thesis (Bachelorarbeit), University of Bremen*, 2010.

[73] R. Nasarek, S. Wereley, and P. Stephan. Flow field measurements near a moving meniscus of a capillary flow with micro particle image velocimetry (upiv). *Proceedings of the Sixth International ASME Conference on Nanochannels, Microchannels and Minichannels, ICNMM2008-62327, Darmstadt 2008*, pages 1–9, 2008.

[74] V. Neacsu, A. Abu Obaid, and S.G. Advani. Spontaneous radial capillary impregnation across a bank of aligned micro-cylinders - part i: Theory and model development. *Int. J. Multiphas. Flow*, 32(6):661–676, 2006.

[75] V. Neacsu, A. Abu Obaid, and S.G. Advani. Spontaneous radial capillary impregnation across a bank of aligned micro-cylinders. part ii: Experimental investigations. *Int. J. Multiphas. Flow*, 32(6):677–691, 2006.

[76] W. Ostwald. Ueber das Zeitgesetz des kapillaren Aufstiegs von Flüssigkeiten und über die Beziehungen desselben zur chemischen Konstitution der letzteren. *Koll.-Zeitschrift, Vol 2, Suppl.-Heft II*, 1908.

[77] D. Patro, S. Bhattacharyya, and V. Jayaram. Flow kinetics in porous ceramics: Understanding with non-uniform capillary models. *J. Am. Ceram. Soc.*, 90(10):3040–3046, 2007.

[78] D. Quéré. Inertial capillarity. *Europhys. Lett.*, 39(5):533–538, 1997.

[79] D. Quéré, É. Raphaël, and J.-Y. Ollitrault. Rebounds in a capillary tube. *Langmuir*, 15(10):3679–3682, 1999.

[80] G. Ramon and A. Oron. Capillary rise of a meniscus with phase change. *J. Colloid Interf. Sci.*, 327(1):145–151, 2008.

[81] E.K. Rideal. On the flow of liquids under capillary pressure. *Philos. Mag. Ser. 6*, 44:1152–1159, 1922.

[82] J.R. Rollins, R.K. Grove, and D.E. Jaekle. Twenty-three years of surface tension propellant management system design, development, manufacture, test, and operation. In *21st Joint Propulsion Conference*, pages 1–9. AIAA-85-1199, 1985.

[83] J. Rouquerol, D. Avnir, C.W. Fairbridge, D.H. Everett, J.H. Haynes, N. Pernicone, J.D.F. Ramsay, K.S.W. Sing, and K.K. Unger. Recommendations for the characterization of porous solids. *Pure Appl. Chem.*, 66(8):1739–1758, 1994.

[84] C.E. Schaefer, D.A. DiCarlo, and M.J. Blunt. Determination of Water-Oil Interfacial Area during 3-Phase Gravity Drainage in Porous Media. *J. Colloid Interface Sci.*, 221:308–312, 2000.

[85] E. Schäffer and P. Wong. Dynamics of Contact Line Pinning in Capillary Rise and Fall. *Physical Review Letters*, 80(14):3069–3072, 1998.

[86] E. Schäffer and P. Wong. Contact line dynamics near the pinning threshold: A capillary rise and fall experiment. *Physical Review E*, 61(5):5257–5277, 2000.

[87] M.K. Schwiebert and W.H. Leong. Underfill flow as viscous flow between parallel plates driven by capillary action. *IEEE Transac. on Components, Packaging and Manufacturing Tech.*, 19(2):133–137, 1996.

[88] J.I. Siddique, D.M. Anderson, and A. Bondarev. Capillary rise of a liquid into a deformable porous material. *Phys. Fluids*, 21(013106):1–15, 2009.

[89] A. Siebold, M. Nardin, J. Schultz, A. Walliser, and M. Oppliger. Effect of dynamic contact angle on capillary rise phenomena. *Colloids and Surfaces A*, 161(1):81–87, 2000.

[90] C.E. Siegert, D.A. Petrash, and E.W. Otto. Time response of liquid-vapor interface after entering weightlessness. Technical Report NASA TN D-2458, Lewis Research Center, Cleveland, Ohio, 1964.

[91] D.E. Smiles. Water flow in filter paper and capillary suction time. *Chem. Eng. Sci.*, 53(12):2211–2218, 1998.

[92] E. M. Sparrow, S. H. Lin, and T. S. Lundgren. Flow development in the hydrodynamic entrance region of tubes and ducts. *Phys. Fluids*, 7(3):338–347, 1964.

[93] J.H. Spurk. *Strömungslehre (5. Auflage)*. Springer-Verlag, 2004.

[94] D.C. Standnes. Spontaneous imbibition of water into cylindrical cores with high aspect ratio: Numerical and experimental results. *J. Petrol. Sci. Eng.*, 50(2):151–160, 2006.

[95] M. Stange. *Dynamik von Kapillarströmungen in zylindrischen Rohren*. Cuvillier, Göttingen, 2004.

[96] M. Stange, M. E. Dreyer, and H. J. Rath. Capillary driven flow in circular cylindrical tubes. *Phys. Fluids*, 15(9):2587–2601, 2003.

[97] T.L. Staples and D.G. Shaffer. Wicking flow in irregular capillaries. *Colloid. Surface. A*, 204(1-3):239–250, 2002.

[98] E.P. Symons. Wicking of liquids in screens. *NASA TN D-7657*, 1974.

[99] J. Szekely, A.W. Neumann, and Y.K. Chuang. The rate of capillary penetration and the applicability of the washburn equation. *J. Colloid Interf. Sci.*, 35(2):273–278, 1971.

[100] B. Taylor. Concerning the ascent of water between two glas planes. *Philosophical Transaction of the Royal Society of London*, 27:538, 1712.

[101] S.R. Valluri, D.J. Jeffrey, and R.M. Corless. Some Applications of the Lambert W Functions to Physics. *Canadian Journal of Physics*, 78:823–831, 2000.

[102] C. van Oss, R. Giese, Z. Li, K. Murphy, J. Norris, M. Chaudhury, and R. Good. Determination of contact angles and pores sizes of porous media by column and thin layer wicking. *J. Adhesion Sci. Technol.*, 6(4):413–428, 1992.

[103] VDI-Gesellschaft. *VDI-Wärmeatlas (10. Auflage), chapter Ml.* Springer-Verlag, Heidelberg, 2006.

[104] E.W. Washburn. The dynamics of capillary flow. *Physical Review*, 17(3):273–283, 1921.

[105] E.W. Washburn. Note on a method of determining the distribution of pore sizes in a porous material. *P. Natl. Acad. Sci. USA*, 7(4):115–116, 1921.

[106] F.M. White. *Fluid Mechanics, 4th. edition.* McGraw Hill, New York, 1998.

[107] F.M. White. *Fluid Mechanics, 5th. edition.* McGraw Hill, New York, 2003.

[108] Wikipedia / Wikimedia. Gnu public license. *Online Image Repository*, 2009.

[109] P. Wong and E. Schäffer. *Experimental Study of Contact Line Dynamics by Capillary Rise and Fall in Contact Angle, Wettability and Adhesion, K.L. Mittal (ed.)*, volume 3, pages 25–37. VSP, 2003.

[110] H.T. Xue, Z.N. Fang, Y. Yang, J.P. Huang, and L.W. Zhou. Contact angle determined by spontaneous dynamic capillary rises with hydrostatic effects: Experiment and theory. *Chemical Physics Letters*, 432:326–330, 2006.

[111] T. Young. An assay on the cohesion of fluids. *Philos. T. R. Soc.*, 95:65–87, 1805.

[112] B.V. Zhmud, F. Tiberg, and K. Hallstensson. Dynamics of capillary rise. *J. Colloid Interface Sci.*, 228(2):263–269, 2000.

# List of Figures

# List of Tables